Towards quantum metrology for nanoscatterers

By

Nora Tischler

A thesis accepted by Macquarie University
for the degree of Doctor of Philosophy
Department of Physics & Astronomy
August 2016

This thesis was written under a cotutelle agreement between the University of Vienna and Macquarie University, for submission to both universities. Except where acknowledged in the customary manner, the material presented in this thesis is, to the best of my knowledge, original and has not been submitted in whole or part for a degree in any university outside of the stated cotutelle agreement.

Nora Tischler

Acknowledgements

The work presented in this thesis was made possible through the financial support of an Australian government funded APA and a cotutelle MQRES of Macquarie University, the Australian Research Council's Centre for Engineered Quantum Systems (EQuS), and the SFB:FoQus program of the Austrian Science Fund (FWF).

In my experience, the quality of a work environment is mainly determined by the people one is surrounded by. I had the pleasure to spend my PhD in two very nice groups around the world, in Sydney and Vienna.

I thank Mathieu Juan and Xavier Vidal for much needed lab advice. Having started my PhD as a complete newbie in the lab, they were the ones who introduced me to the world of experiments, generously sharing their experience with me and teaching me many handy tricks.

Also, thanks to Ivan Fernandez-Corbaton and Xavier Zambrana-Puyalto for their friendship and being role-model PhD students to me. I continued to be amazed both by the quality of their work and their ability to hold on to idealistic views of how science should work.

My advisor Gabriel Molina-Terriza has inspired me by demonstrating how great physicists first and foremost care about the physics, and what effect this caring has. It leads to a deep understanding of the concepts, and the ability to ignore usually perceived boundaries: For one, the division between theorists and experimentalists, and also the boundaries between different topics.

My other advisor Anton Zeilinger then offered me the wonderful opportunity to go and join his group in Vienna. Everyone there quickly made me feel like part of the team. I would like to thank especially Robert Fickler, Radek Lapkiewicz, Mehul Malik, Mario Krenn, and Manuel Erhard for their friendship, support, and for the countless interesting discussions at all times of the day and night. I also feel privileged to have experienced Anton's ambitious and passionate approach to physics, and his ability to home in on the essential and interesting things.

Of course it is not only the work environment that determined my last few years. Last but not least, I would like to thank my partner Jack Gillespie for his unconditional love and

support. He has always been there to celebrate the good times and help me put things in perspective and get through the difficult ones.

List of Publications

- K. Vernon, D. Gomez, T. Davis, and N. Tischler. *Simulations of the effect of waveguide cross-section on quantum dot - plasmon coupling.* J. Appl. Phys. **110**, 074315 (2011).
- I. Fernandez-Corbaton, N. Tischler, and G. Molina-Terriza. *Scattering in multilayered structures: Diffraction from a nanohole.* Phys. Rev. A **84**, 053821 (2011).
- K. Vernon, N. Tischler, and M. Kurth. *Coupling of energy from quantum emitters to the plasmonic mode of V groove waveguides: A numerical study.* J. Appl. Phys. **111**, 064323 (2012).
- N. Tischler, X. Zambrana-Puyalto, and G. Molina-Terriza. *The role of angular momentum in the construction of electromagnetic multipolar fields.* Eur. J. Phys. **33**, 1099 (2012).
- I. Fernandez-Corbaton, X. Vidal, N. Tischler, and G. Molina-Terriza. *Necessary symmetry conditions for the rotation of light.* J. Chem. Phys. **138**, 214311 (2013).
- I. Fernandez-Corbaton, X. Zambrana-Puyalto, N. Tischler, X. Vidal, M. L. Juan, and G. Molina-Terriza. *Electromagnetic duality symmetry and helicity conservation for the macroscopic Maxwell's equations.* Phys. Rev. Lett. **111**, 060401 (2013).
- N. Tischler, I. Fernandez-Corbaton, X. Zambrana-Puyalto, A. Minovich, X. Vidal, M. L. Juan, and G. Molina-Terriza. *Experimental control of optical helicity in nanophotonics.* Light Sci Appl **3**, e183 (2014).
- A. Büse, N. Tischler, M. L. Juan, and G. Molina-Terriza. *Where are photons created in parametric down-conversion? On the control of the spatio-temporal properties of biphoton states.* J. Opt. **17**, 065201 (2015).
- N. Tischler, A. Büse, L. G. Helt, M. L. Juan, N. Piro, J. Ghosh, M. J. Steel, and G. Molina-Terriza. *Measurement and shaping of biphoton spectral wave functions.* Phys. Rev. Lett. **115**, 193602 (2015).

- N. Tischler, M. L. Juan, S. Singh, X. Zambrana-Puyalto, X. Vidal, G. Brennen, and G. Molina-Terriza. *Topological metrology and its application to optical position sensing.* arXiv: 1505.00547 (2015).

- M. Krenn, N. Tischler, and A. Zeilinger. *On small beams with large topological charge.* New J. Phys. **18**, 033012 (2016).

Curriculum Vitae

Personal Information

Name:	Nora Tischler
Date of birth:	29. April, 1987
Place of birth:	Budapest, Hungary

Education

Higher Degree Research

2012 - 2016:	PhD candidature at Macquarie University, Australia (since 2012) and the University of Vienna, Austria (cotutelle since 2014)

Tertiary Education

2011:	Bachelor of Applied Science (First Class Honours), majoring in physics, at Queensland University of Technology (QUT), Australia
2010:	Bachelor of Applied Science (majoring in physics) / Bachelor of Mathematics double degree at QUT, Australia

School

2006:	High school "Abitur" certificate from Grimmelshausen Gymnasium Gelnhausen, Germany

Teaching experience

May - Aug 2014:	Tutor for the Macquarie University Campus Wellbeing, Australia
Feb - Nov 2011:	Laboratory Demonstrator for the Discipline of Physics, QUT, Australia
Feb 2009 - Nov 2010:	Tutor for the School of Mathematical Sciences, QUT, Australia
Aug 2008 - Nov 2011:	Peer Advisor, QUT, Australia

Awards and Prizes

2011:	QUT University Medal (awarded for exceptional academic performance in the Bachelor or Applied Science (Honours) (Physics) - First Class Honours).
2011:	QUT University Medal (awarded for exceptional academic performance in the Bachelor or Applied Science (Physics) - with Distinction / Bachelor of Mathematics - with Distinction).
2011:	Dean's Award for Academic Excellence, Bachelor of Applied Science / Bachelor of Mathematics (QUT): Awarded to the student who completed in 2010, with highest overall GPA.
2011:	Trevor Lewis Memorial Bursary 2010 (QUT): Awarded to a student entering the Honours course in Physics or the Masters of Applied Science course in Medical Physics, with the highest academic merit.
2011:	Mathematical Sciences Staff Prize in Mathematics Double Degree (QUT): Awarded to the student enrolled in the Bachelor of Mathematics or Bachelor of Applied Science (Mathematics) within a double degree program, who is the most academically outstanding graduate of the year.
2008 - 2010:	Mathematical Sciences Staff Prizes (first year, second year, third year), QUT: Awarded to the student enrolled in the Bachelor of Mathematics or Bachelor of Applied Science (Mathematics) or double degree program in Mathematics who obtains the best results in the Mathematics component of the respective year of the course.

Research Experience in Addition to Degrees

Jan - Feb 2011:	A 6 week research project at QISS, Department of Physics and Astronomy, Macquarie University, Australia. Supervisor: Dr. Gabriel Molina-Terriza.
Dec 2009 - Feb 2010:	An 8 week research project with the Quantum Atom Optics Group, School of Mathematics and Physics, University of Queensland, Australia. Supervisor: Dr. Joel Corney.

Abstract

Measurements play a pivotal role in the advance of science and technology. To name just two examples, the global positioning system (GPS) technology relies on atomic clocks, and the detection of gravitational waves has been achieved via extremely precise interferometric measurements.

The aim of my thesis is to contribute towards the goal of doing quantum metrology with nanophotonic structures. With this motivation, some problems across the fields of nanophotonics and quantum optics are tackled.

First, the role of helicity within nanophotonics is explored. In the context of symmetries and conserved quantities, helicity, the projection of the total angular momentum on the linear momentum direction, is a useful addition to the more commonly considered quantities such as angular momentum. A simple but versatile experimental treatment of helicity is introduced and demonstrated on the scattering of focused light by circular nanoholes in a gold film. The helicity transformation that takes place in this light-matter interaction is studied.

Another section is devoted to the topic of quantum light sources. It is shown how to influence and measure the spectrotemporal wavefunction of photon pairs by exploiting properties of the spontaneous parametric down-conversion (SPDC) process. The proposed technique also allows to determine the distribution of time delays between the two photons in a pair, which is typically a challenging experimental task.

Finally, a quantum metrology experiment on the interaction of light with chiral molecules is presented. In this proof-of-concept experiment entangled photon pairs are used for the measurement of natural optical activity and its wavelength dependence, the optical rotatory dispersion.

Messungen spielen eine Schlüsselrolle im Fortschritt von Wissenschaft und Technik. So beruht zum Beispiel die Technologie des Global Positioning Systems (GPS) auf Atomuhren, und auch die Detektion von Gravitationswellen wurde durch extrem präzise interferometrische Messungen erreicht.

Meine Dissertation verfolgt das Ziel, einen Beitrag zur Ermöglichung von Quantenmetrologie mit nanophotonischen Strukturen zu leisten. Aus dieser Motivation heraus werden einige Fragestellungen in den Gebieten der Nanophotonik und Quantenoptik behandelt.

Zuerst wird die Rolle der Helizität in der Nanophotonik untersucht. Im Kontext von Symmetrien und Erhaltungsgrößen stellt Helizität, die Projektion des gesamten Drehimpulses auf die Richtung des linearen Impulses, eine nützliche Erweiterung zu den geläufigeren Größen, wie dem Drehimpuls, dar. Eine einfache, jedoch vielseitige experimentelle Behandlung der Helizität wird eingeführt und anhand der Streuung von fokussiertem Licht durch runde Nanolöcher in einem Goldfilm demonstriert. Die in dieser Interaktion zwischen Licht und Materie stattfindende Transformation von Helizität wird anschließend erforscht.

Ein weiterer Teil der Dissertation behandelt das Thema von Quanten-Lichtquellen. Es wird gezeigt, wie die spektro-temporale Wellenfunktion beeinflusst und gemessen werden kann, indem Eigenschaften des Spontaneous Parametric Down-Conversion (SPDC) Vorgangs ausgenutzt werden. Die vorgeschlagene Methode erlaubt auch die Bestimmung der Verteilung von Zeitverzögerungen zwischen den zwei Photonen eines Paares, was üblicherweise eine experimentell schwierige Aufgabe ist.

Zum Schluss wird ein Quantenmetrologie-Experiment zur Interaktion zwischen Licht und chiralen Molekülen vorgestellt. In diesem Grundlagenexperiment werden verschränkte Photonenpaare benutzt, um natürliche optische Aktivität und deren Wellenlängenabhängigkeit zu messen.

Contents

Abbreviations

APD ..... avalanche photodiode.

arb. ..... arbitrary.

BS ..... beam splitter.

CCD ..... charge coupled device.

cw ..... continuous wave.

DOF ..... degree of freedom.

FI ..... Fisher information.

FIB ..... focused ion beam.

Fig. ..... Figure.

FROG ..... frequency-resolved optical gating.

FWHM ..... full width at half maximum.

GPS ..... global positioning system.

H ..... horizontal.

HB ..... Holland-Burnett.

HOM ..... Hong-Ou-Mandel.

HWP ..... half waveplate.

KTP ..... potassium titanyl phosphate.

LC ..... left circular.

MZI ..... Mach-Zehnder interferometer.

NA ..... numerical aperture.

ORD..... optical rotatory dispersion.

PBS ..... polarising beam splitter.

PEC..... perfect electric conductor.

POVM..... positive operator valued measure.

ppKTP ..... periodically poled potassium titanyl phosphate.

QFI..... quantum Fisher information.

QPD..... quadrant photodiode.

QWP ..... quarter waveplate.

RC ..... right circular.

Ref..... Reference.

Sec..... Section.

SEM..... scanning electron microscope.

SERS..... surface-enhanced Raman spectroscopy.

SFG ..... sum-frequency generation.

SLM..... spatial light modulator.

SMF..... single-mode fibre.

SPDC..... spontaneous parametric down-conversion.

V ..... vertical.

Statement of contributions

Chapter 1, Section 1.2.3
This section is partly based on Ref. [1], for which I performed the simulations.

Chapter 2
The nanostructure samples used for the experiments of this chapter were fabricated by Dr. Alexander Minovich. Both sections contain simulation results by Dr. Ivan Fernandez-Corbaton. The projects were supervised by Assoc. Prof. Molina-Terriza.

Section 2.3
The experiment and data analysis were carried out by me and Dr. Mathieu Juan. The ideas behind the experiment stem from Dr. Mathieu Juan, Dr. Ivan Fernandez-Corbaton, Dr. Xavier Zambrana-Puyalto, Dr. Xavier Vidal, and Assoc. Prof. Molina-Terriza.

Section 2.4
The experiment and data analysis shown in this section were done by me, with assistance from Dr. Mathieu Juan. The idea for the technique was conceived by the group of Assoc. Prof. Molina-Terriza, including Dr. Mathieu Juan, Dr. Ivan Fernandez-Corbaton, Dr. Xavier Zambrana-Puyalto, and Dr. Xavier Vidal.

Chapter 3
Both sections of Chapter 3 contain simulations. The code for these simulations was developed by me, incorporating parts of previous scripts by Assoc. Prof. Molina-Terriza, and with his advice. The simulations were performed by me.

Section 3.2
I developed the idea for the mechanism underlying the effect that is the subject of Section 3.2 and did the analytic and numerical work. The observation of the effect arose from a joint project with my colleague Alexander Büse: We had built a spontaneous parametric down-conversion source and Hong-Ou-Mandel (HOM) experimental set-up together, and had

observed an impediment to the HOM dip visibility, which is caused by, and led us to study, the time delay effect. We divided the remainder of the project such that I would be responsible for the theory and Alexander Büse for the experiment, with regular joint discussions to exchange ideas. The measurements of the effect, which are shown for comparison and are explained in Ref. [2], were devised and performed by him. The project was supervised by Assoc. Prof. Molina-Terriza.

Section 3.3

I developed the method, the simulations, and the data analysis presented in Section 3.3 with the help of contributions as detailed below:

The project was initiated by the idea of Assoc. Prof. Molina-Terriza, that a change in crystal temperature might provide useful information about the biphoton wavefunction. Dr. Luke Helt oversaw my analytic work. He also supported the progress of the project through regular conversations and came up with the idea that a shift in the pump frequency could be an alternative to changing the crystal temperature. Assoc. Prof. Michael Steel contributed to the planning and assessment of the project through discussions. Alexander Büse contributed through discussions and consultation about the experimental feasibility of the method. He also performed experiments implementing the method, which can be found in [3] and are shown in this thesis for comparison. Assoc. Prof. Molina-Terriza had the idea that the method is also applicable to biphoton states created by four-wave mixing processes, and supervised the entire project.

Chapter 4

I devised and conducted the experiment of this chapter as well as the data analysis. The work was supported through the following contributions: Dr. Robert Fickler built up the photon pair source in the polarisation-based Sagnac interferometer used for the experiment. Dr. Xavier Vidal gave me advice about experimental techniques for measuring optical activity, and took classical optical activity measurements that were used to test the predictions of the Drude model. The project was also aided by useful discussions with Mario Krenn, Assoc. Prof. Gabriel Molina-Terriza, and Dr. William Plick. It was supervised by Prof. Anton Zeilinger.

Appendix A

The nanofabrication described in this appendix was done by me. Michael Larkins inducted and assisted me in this process, in particular in the use of the focused ion beam machine and the ellipsometer. The fabrication was supervised by Dr. Kristy Vernon.

Chapter 1

Introduction

1.1 General introduction

As one of our primary senses, vision provides information about our surroundings through the detection of light that has interacted with them. In our everyday lives, we typically encounter situations in which classical light interacts with bulk objects. As a result, this is the regime that we develop intuition for. However, in accordance with the advice of John Archibald Wheeler to "find the strangest thing and then explore it" [quoted in 4], it is possible to move out of this familiar regime. On the one hand, we can reduce the features of the matter to tiny scales, which the field of nanophotonics deals with. On the other hand, we can also choose exotic states of light, covered by the field of quantum optics. The work presented in this thesis contributes to the goal of probing nanoscatterers with nonclassical light. It therefore addresses problems in, and combines the two fields. Here, I will provide a brief introduction to the fields.

1.1.1 Nanophotonics

Nanophotonics deals with optical phenomena on the subwavelength level, such as the interaction of classical light with matter at these scales [5]. This means that the matter can be of subwavelength dimensions, an example of which is a nanoparticle. Alternatively, it may consist of an overall larger object containing structure on the subwavelength scale. The two possibilities are illustrated in Fig. 1.1. An interesting example are the man-made metamaterials, typically composite objects that contain several materials arranged in a periodic pattern, designed in a way such that they produce a particular effect on electromagnetic radiation [6, Sec. 1.1]. So what is special about light-matter interaction in this regime? I will now describe some key features of nanophotonics that will also play a role in this thesis:

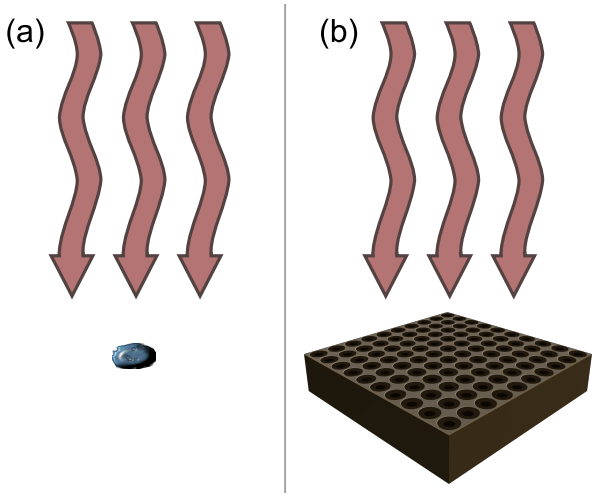

FIGURE 1.1: For a typical interaction of light with matter treated by nanophotonics, the matter can have overall subwavelength size (a) or contain features of subwavelength size (b).

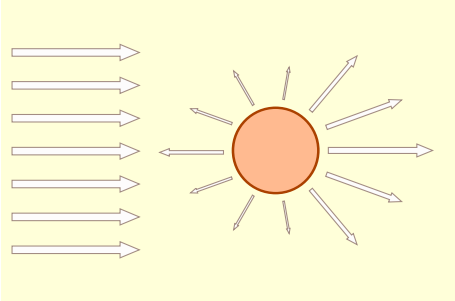

FIGURE 1.2: Schematic of the system solved by Mie theory: Scattering of a plane wave by a sphere in a uniform background.

1. A strong dependence on the scatterer size and the wavelength of the light, 2. evanescent fields, and 3. effective media.

A lot can be learned from one of the simplest problems in nanophotonics, illustrated in Fig. 1.2. It consists of a sphere that is contained in a uniform medium and is probed by light of a single wavelength, which is incident as a plane wave. The analytic solution to this problem is known as Mie theory (the interested reader is referred to Chapter 4 of [7] for a nice coverage of Mie theory). Since the scatterer and its surrounding medium are spherically symmetric, the most convenient coordinate system for the description of the scattered field is the spherical one. Indeed, the multipolar fields that one obtains when using the spherical coordinate system to construct a set of basis functions of solutions to Maxwell's equations [8, Sec. 13.1], are the natural modes of the scatterer. Mie theory describes how, depending on the ratio of wavelength and scatterer size, different multipolar moments can be excited,

and this determines the scattered field. The analytically understood example problem of the spherical scatterer thus very nicely demonstrates one of the characteristic features of nanophotonic scattering problems, namely a strong dependence on the size of the scatterers and the wavelength. A pronounced wavelength dependence can also arise from resonances of the nanostructure [5, Chapter 12]. Another central feature of nanophotonics problems already present in Mie theory are evanescent fields, which are illustrated in Fig. 1.3. These are fields that decay exponentially with increasing distance from an object, for example the scatterer surface [5, Sec. 2.11]. Unlike free-space radiation, the energy of evanescent fields is bound to the surface and does not propagate away from it. Within the small regions where the fields exist, they can be extremely large. In some applications, such as surface-enhanced Raman spectroscopy (SERS), this can be used to boost an otherwise weak signal [9, Chapter 9].

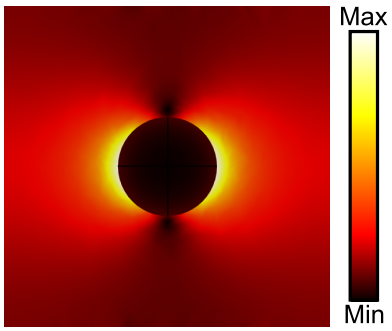

Figure 1.3: Evanescent fields. Plotted is the electric field norm around a subwavelength sized metallic nanosphere, which is illuminated with a plane wave.

In problems where the scatterer is not an isolated object but a more complex multi-component structure, a further important concept in nanophotonics can prove very useful. It is the concept of effective media, meaning that it is sometimes possible to account for small scale scatterer features by modelling the object as a uniform bulk material with modified properties ([10], and [6, Sec. 1.2]). This is similar to the transition from microscopic Maxwell equations to the macroscopic ones. There, a more complex description of the system at the level of atoms that make up matter, and involving the electrons that interact with the electromagnetic fields, is replaced by a simpler model, in which the light-matter interaction is incorporated as a homogeneous property of matter at a larger scale. The concept of effective media helps to understand how metamaterials can be tailored to exhibit exotic properties such as negative refractive indices as a whole, even though the constituent components are made of conventional materials [11, 12].

1.1.2 Quantum optics

The other field relevant to this thesis is quantum optics. As the name suggests, light is quantised, as a result of which the possible values of energy that could be obtained when measuring an electromagnetic excitation of a fixed frequency are not continuous, but discrete. The quantisation was proposed by Einstein in the 1905 paper [13], where based on thermodynamic properties, he established an analogy between heat radiation and ideal gases, which consist of spatially localised, independent particles. The quantisation of light allowed the explanation of two puzzling physical phenomena: Black-body radiation (Max Planck, 1901, [14]) and the photoelectric effect (Albert Einstein, 1905, [13]). The reason such a fundamental fact about electromagnetic radiation was discovered fairly late is that in everyday situations, we tend to be in a regime where the number of photons is so large that the discretisation in energy is not noticeable, and where the response depends on the mean number of photons. In the classical regime and for mean photon numbers, the predictions of quantum optics agree with classical optics. However, light generally has a distribution over different photon numbers, so its state is not fully characterised by the mean photon number, the first moment of the distribution. Quantum optics is able to describe problems where these distributions become noticeable.

A nice example is the Hong-Ou-Mandel (HOM) experiment, which is concerned with the photon number distribution at the output of a beam splitter when two photons are incident, one in each input arm [15]. Each photon incident individually would have equal probabilities of being transmitted and reflected. On the other hand, as illustrated in Fig. 1.4, when both photons are incident and they are indistinguishable, the probability amplitudes for both photons being transmitted and both being reflected cancel out. It results in the suppression of the probability to obtain a single photon in each output arm, so that the two photons must exit in the same arm. This type of interference occurs in quantum mechanics because coherent sums over different possibilities, superpositions, are possible. In the HOM experiment, coincidences of photons exiting in different directions are monitored while sweeping the relative delay of the two photons arriving at the beam splitter. The quantum interference shows itself as a dip in the coincidences at zero relative time delay.

Many fascinating features of quantum mechanics manifest themselves in optics. One of these is entanglement. Superpositions and the fact that two or more objects, which may be spatially separated, can share a state, give rise to the possibility of remarkable correlations between the objects. Given two correlated particles, we might have no information at all about the properties of the particles individually, but once we establish the properties of one, we also know those of the other [16, Sec. 8.1]. Correlations are also possible classically,

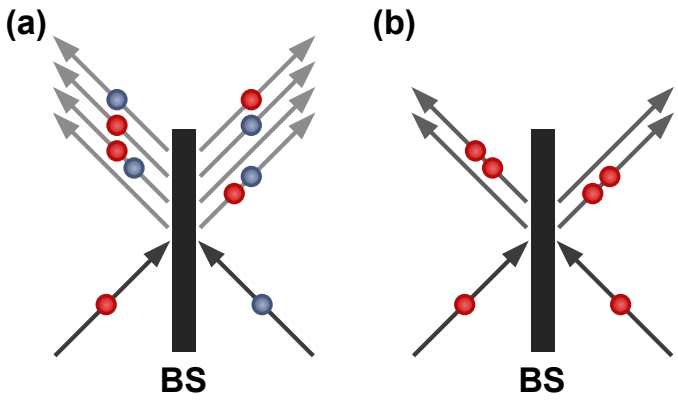

Figure 1.4: Quantum interference: A beam splitter (BS) with one photon incident at each input. Different possible output events are shown as outgoing arrows at different heights. When the photons are completely distinguishable (a), there is equal probability of the photons exiting in opposite directions and in equal directions. When the photons are completely indistinguishable (b), the two photons leave in the same direction due to quantum interference.

but entanglement is a special type of correlation that goes beyond what is permitted in classical models. Multi-photon states can exhibit this property. Entangled photon pairs can be created in nonlinear optical processes, for example in spontaneous parametric down-conversion (SPDC). SPDC is a process occurring in nonlinear materials, where a high energy photon, typically from an intense laser beam, has a small probability to be converted into a pair of photons with lower energy. We will investigate this process in more detail in Chapter 3.

Another central feature of quantum physics that can be observed in quantum optics experiments is the fact that some pairs of quantities are incompatible, such that they cannot simultaneously be known with arbitrary precision [17, Sec. 5.2.4]. The feature is described through so-called uncertainty relations. For light, an uncertainty relation exists for its amplitude and phase relative to a reference [18], [19, Sec. 15.4]. This property of light in quantum optics is in stark contrast to what is expected from classical optics, where the phase and amplitude can simultaneously be well defined.

Both uncertainty relations and entanglement play an important role in optical quantum metrology [20, Chapter 13], [21]. Quantum metrology is a branch of physics devoted to the study of the measurement process in the framework of quantum physics. It has shown that the use of nonclassical states for the measurement process can offer advantages over classical states. In the case of optical quantum metrology, light is used as the measurement probe, and the measurement precision for a fixed mean number of photons can be improved by using nonclassical states of light. The most well known such states are:

1. squeezed states, where one variable has reduced uncertainty at the expense of an increased uncertainty in the conjugate variable [22], and
2. NOON states, where the light is in a superposition of having all photons in one mode (e.g. path) and all in another one [23].
An optical quantum metrology experiment is presented in Chapter 4.

1.1.3 Scope of the project

This PhD project works towards the goal of probing nanoscatterers with quantum light. Certain tools are required to pave the way for this new topic, involving both nanophotonics and quantum optics: First of all, even for a nonclassical state of light, the modes obey Maxwell's equations. Thus, for the comprehension and modelling of such a problem, it is a prerequisite that we understand the corresponding classical light-matter interaction. Secondly, we require a well controlled quantum light source that we can use as a probe. During my project, I have worked on both of these aspects separately, and also performed a quantum metrology experiment on the interaction of light with very small scatterers, namely chiral molecules.

1.2 Background

This subsection lays out some physics concepts and a mathematical framework that will be important in the main body of the thesis. Depending on the familiarity level of the reader with the topics, it may serve either as an introduction, as a refresher, or may alternatively be skipped altogether.

1.2.1 Classical versus quantum light

It is not uncommon for classical and quantum optics to be treated as if they were barely related. The separation is achieved in classical optics by focusing on problems in which quantum effects are negligible.

Things are somewhat different on the side of quantum optics, because the electromagnetic modes that are quantised still have to fulfil Maxwell's equations, which therefore constitute an integral part of the problem [17, Sec. 2.1.1], [24]. For example, the classical vector potential, from which the electric and magnetic fields can be obtained, has the following

Hermitian operator as its quantum optical counterpart [17, Sec. 2.2.1]:

$$\hat{\mathbf{A}}(\mathbf{r},t) = \sum_i \left(\mathbf{A}_i(\mathbf{r},t)\,\hat{a}_i + \mathbf{A}_i^*(\mathbf{r},t)\,\hat{a}_i^\dagger \right). \tag{1.1}$$

The mode functions $\mathbf{A}_i$ form an orthonormal basis set for solutions to the electromagnetic wave equation in accordance with Maxwell's equations [25, Sec. 6.1], $\mathbf{r}$ and t stand for spatial and temporal coordinates, and the $\hat{a}_i$, $\hat{a}_i^\dagger$ are annihilation and creation operators. Eq. (1.1) shows that the modes themselves are like classical modes, but their occupation is modelled as that of quantum mechanical harmonic oscillators.

Yet, quantum optics problems are frequently restricted to particularly simple physical systems, in which the classical electromagnetic modes are well known and no longer explicitly written down. In problems involving only few modes, one often labels the modes in question and thinks of the light-matter interaction from a simple operational viewpoint, although the actual modes are the solutions of Maxwell's equations [24]. For instance, this is common practice in systems with optical fibres, waveguides, and beam splitters.

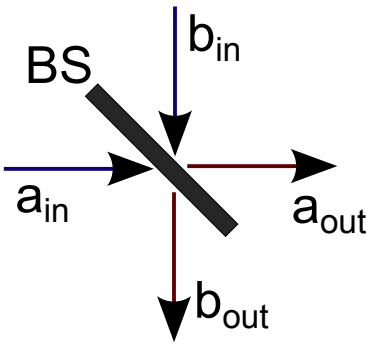

Figure 1.5: A beam splitter (BS) as a simplified device that transforms two input modes into two output modes.

As an example, Fig. 1.5 illustrates how one would think of a beam splitter as a device with only two input modes and two output modes. The underlying assumption might be that they are all Gaussian beams of a particular beam waist, wavelength, and with a particular polarisation, propagating at an angle of 45° with respect to the beam splitter surface. Then a multitude of other possible modes, for instance with different polarisation or spatial structure (such as higher order Laguerre or Hermite Gaussian modes), have implicitly been excluded from the description.

And indeed, many fascinating phenomena, such as two-photon quantum interference in the HOM experiment, already emerge in this type of setting. Moreover, such a treatment

can help to identify the mathematical equivalence of physically distinct systems or degrees of freedom (DOF), which enables the application of already established knowledge to new problems. The restriction to a small number of modes can be based 1. on a physical limitation of the allowed modes, such as imposed by a single-mode fibre (SMF), or 2. on assumptions, for instance when a free-space beam splitter is labelled as having two spatial inputs and outputs as in Fig. 1.5, implicitly assuming fixed, symmetric and equal transverse spatial modes and polarisations. Remembering to distinguish between these two cases can be fruitful, since in the latter case the system can obviously be extended by lifting the assumptions. For example, richer features of two-photon quantum interference were demonstrated by introducing more complex modes to the HOM experiment [26]. When trying to extend quantum optics to any new physical setting, we need to keep in mind that an understanding of the classical Maxwell modes of the system is a prerequisite.

1.2.2 Symmetries and conserved quantities

Some considerations based on the concept of symmetry are so general that they find frequent use in both classical and quantum optics [27]. Symmetries allow short-cuts that provide a powerful way of analysing physical systems: They enable us to draw conclusions about the behaviour of a system, even if our knowledge about it is incomplete.

Let us consider an object of interest and the physical system it is contained in. The object of interest might be an electron wavefunction, or an electromagnetic field. The physical system is determined by the environment the object interacts with, and the equations governing its time evolution or input-output relations. For the electron wavefunction, the environment could be a distribution of charges, and the equation of motion the Schroedinger equation. For the example of the electromagnetic field, we might have a known field incident on a scatterer, and we are interested in the scattered field. The light-matter interaction can mathematically be expressed as a scattering matrix, which relates the incident field with the scattered field, and is determined by Maxwell's equations and the properties of the system. The first example is a quantum system, while the second is a classical optics problem. I will work with the quantum formalism, because it allows to reach the results in a more accessible manner. The next part mainly follows Chapter 17 of [28].

A symmetry is an invariance with respect to some unitary transformation, examples of which are translations, rotations, and inversions in space. We will denote the symmetry transformation by $\hat{U}$. All unitary transformations have the property $\hat{U}^\dagger\hat{U} = \hat{U}\hat{U}^\dagger = \mathbb{1}$, where † means taking the Hermitian conjugate and $\mathbb{1}$ is the identity. Important properties of unitary transformations are that they are reversible and preserve the normalisation, i.e.

the total probability of finding the object in one of the possible states is unchanged by the action of the unitary operator. Mathematically, a symmetry of an object with respect to a unitary transformation means that the state of the object remains the same under the transformation, except for a possible global phase. A symmetry of a system with respect to a unitary transformation is equivalent to the Hamiltonian or the scattering matrix commuting with the transformation. What are the implications of this?

Firstly, symmetries enable the convenient creation of new solutions. Assume we know that the system possesses a symmetry, but the object itself is not symmetric. Starting with a first solution, we can then apply the unitary transformation to create another, distinct solution. This means that if we have the solution for one initial condition, we also know the solution associated with another initial state. The two solutions are simply related by the symmetry operation. Letting $|\Psi\rangle$ be the state of the object with the subscripts i and f denoting initial and final, which are related by the transformation $\hat{T}$, and subscripts 1 and 2 distinguishing two states related by the symmetry transformation $\hat{U}$, this can be seen in the following way: $|\Psi_{f2}\rangle = \hat{T}|\Psi_{i2}\rangle = \hat{T}\hat{U}|\Psi_{i1}\rangle = \hat{U}\hat{T}|\Psi_{i1}\rangle = \hat{U}|\Psi_{f1}\rangle$.

Secondly, and very importantly, an intimate link exists between symmetries and conservation laws. To get an understanding of this, let us consider a situation in which both the system and the initial state of the object have a symmetry. As a consequence of $\hat{U}$ being unitary and the initial state being symmetric, we can write $\hat{U}|\Psi_i\rangle = \exp(im)|\Psi_i\rangle$, with $m \in \mathbb{R}$ to give an eigenvalue of modulus one, which is simply a global phase. To answer the question how the operator $\hat{U}$ acts on the final state, we can once more make use of the fact that $\hat{U}$ and $\hat{T}$ commute: $\hat{U}|\Psi_f\rangle = \hat{U}\hat{T}|\Psi_i\rangle = \hat{T}\hat{U}|\Psi_i\rangle = \hat{T}\exp(im)|\Psi_i\rangle = \exp(im)\hat{T}|\Psi_i\rangle = \exp(im)|\Psi_f\rangle$. This shows that the final state is also an eigenstate of the operator $\hat{U}$, with the same eigenvalue as the initial state, hence the eigenvalue is conserved.

Of great importance in physics are one-dimensional continuous symmetry groups connected to the identity, for which it is possible to write the unitary transformation in the form $\hat{U}(\phi) = \exp\left(-i\hat{O}\phi\right)$. Here $\hat{O}$ is a Hermitian operator that is called the generator of the group, and ϕ is a real, continuous parameter. Then the symmetric states can be labelled by their eigenvalue $\hat{U}(\phi)|\Psi_o\rangle = \exp(-i\phi o)|\Psi_o\rangle$, where o is the state's eigenvalue with respect to the generator of the transformation. The quantity associated with the generator is also a conserved quantity. For classical systems, it was formally shown by Noether in 1918 that for every continuous symmetry of the system, there exists a conservation law [29]. Some familiar examples of transformations and their generators are translations generated by linear momentum, and rotations generated by angular momentum. And indeed, a translationally symmetric system conserves linear momentum, while a cylindrically symmetric system conserves the component of the angular momentum along the axis of symmetry [28,

Chapter 17]. As a simple example, consider an electromagnetic field incident on a planar interface. The physical system is translationally invariant in the directions parallel to the interface, as are Maxwell's equations. So if a plane wave is chosen as the incident field, it has a definite transverse momentum, and this momentum is conserved. It is $\hbar k_0 n \sin(\theta)$, $\hbar$ being the reduced Planck's constant, k_0 the wavenumber in vacuum, n the refractive index of the subdomain, and θ the angle of incidence. A division by the constant $\hbar k_0$ and application across different subdomains directly leads to Snell's law.

The above overview has shown that the presence of symmetries provides concrete, quantitative predictions about the object in question. In particular, if we enter with an eigenstate of the generator of a symmetry transformation and the evolution possesses the same symmetry, then we know that the eigenvalue has to be preserved. Things get more complicated when the symmetry is absent. Based on ideas from quantum information theory, Marvian and Spekkens proposed measures of asymmetry for states, leading to restrictions on how non-symmetrical states can evolve under symmetric dynamics [27]. In contrast, for the case where the input state is symmetric but the dynamics lack the symmetry, we only have the qualitative information that the eigenvalue is in general not preserved. We will return to the intriguing question what effect the absence of a symmetry from the evolution has on several occasions.

1.2.3 Helicity

Although the examples of symmetry groups mentioned above are of a geometrical character, more abstract transformations can also be considered. Here we focus on another observable and the corresponding non-geometrical symmetry transformation, namely helicity and the duality transformation. They will form the subject of the first experiment presented in this thesis. This current section is primarily based on Refs. [1, 30, 31].

Compared to the total angular momentum, helicity, the projection of the total angular momentum onto the linear momentum direction [32, Sec. 8.4.1], is a less studied observable in the context of symmetries and conserved quantities within optics. Its definition is perhaps most easily understood in the plane wave decomposition, or in other words angular spectrum, of an electromagnetic field, where it is associated with the handedness of circular polarisation of each plane wave with respect to its momentum vector. For an electromagnetic field to be in an eigenstate of helicity it must fulfil that each of the plane waves composing the total field has the same handedness of circular polarisation. From this description it is easy to realise that in real space, where all the different plane waves are integrated, the helicity of a general electromagnetic field does not bear a simple relationship with the polarisation

components of the electric field. As will be shown below, the important case of collimated beams is an exception to this rule: Collimated beams that are eigenstates of helicity can, to a good approximation, be described as circularly polarised beams with their handedness given by the eigenvalue of helicity; a helicity of ± 1 corresponds to left/right circular (LC/RC) polarisation.

As experiments in optics often involve cylindrically symmetric beams, whether collimated or not, it is convenient to use the cylindrically symmetric Bessel beams as a basis set for electromagnetic fields in a theoretical description. We will use Bessel beams for the analysis related to helicity and angular momentum states, which will allow us to understand the experiment of Section 2.3. Bessel modes can be written as two types of vector wave functions ($\mathbf{C}_{\mathrm{mp_z}}$ and $\mathbf{D}_{\mathrm{mp_z}}$) which are simultaneously eigenstates of the energy given by the magnitude of the wavevector k, the z component of the linear momentum (i.e. $P_z\mathbf{C}_{\mathrm{mp_z}} = \mathrm{p_z}\mathbf{C}_{\mathrm{mp_z}}$, $P_z\mathbf{D}_{\mathrm{mp_z}} = \mathrm{p_z}\mathbf{D}_{\mathrm{mp_z}}$) and angular momentum (i.e. $J_z\mathbf{C}_{\mathrm{mp_z}} = \mathrm{m}\mathbf{C}_{\mathrm{mp_z}}$, $J_z\mathbf{D}_{\mathrm{mp_z}} = \mathrm{m}\mathbf{D}_{\mathrm{mp_z}}$), and also the helicity ($\Lambda\mathbf{C}_{\mathrm{mp_z}} = -\mathbf{C}_{\mathrm{mp_z}}$ and $\Lambda\mathbf{D}_{\mathrm{mp_z}} = +\mathbf{D}_{\mathrm{mp_z}}$, respectively) [30, 31]. The expressions for these fields in real space are given below. Cylindrical coordinates $[\rho, \theta, z]$ are used for the spatial variables and the helical basis $[\hat{\mathbf{r}}, \hat{\mathbf{l}}, \hat{\mathbf{z}}]$ for the vectorial character of the fields, where $\hat{\mathbf{l}} = (\hat{\mathbf{x}} + i\hat{\mathbf{y}})/\sqrt{2}$, $\hat{\mathbf{r}} = (\hat{\mathbf{x}} - i\hat{\mathbf{y}})/\sqrt{2}$. A harmonic time dependence of $\exp(-i\omega t)$ is implicitly assumed.

$$\begin{aligned}
\mathbf{C}_{\mathrm{mp_z}}(\rho,\theta,\mathrm{z}) &= A(z)\exp(i\mathrm{m}\theta)[B_+ J_{\mathrm{m}+1}(p_\rho\rho)\exp(i\theta)\hat{\mathbf{r}} + B_- J_{\mathrm{m}-1}(p_\rho\rho)\exp(-i\theta)\hat{\mathbf{l}} + i\sqrt{2}p_\rho J_{\mathrm{m}}(p_\rho\rho)\hat{\mathbf{z}}],\\
\mathbf{D}_{\mathrm{mp_z}}(\rho,\theta,\mathrm{z}) &= A(z)\exp(i\mathrm{m}\theta)[B_- J_{\mathrm{m}+1}(p_\rho\rho)\exp(i\theta)\hat{\mathbf{r}} + B_+ J_{\mathrm{m}-1}(p_\rho\rho)\exp(-i\theta)\hat{\mathbf{l}} - i\sqrt{2}p_\rho J_{\mathrm{m}}(p_\rho\rho)\hat{\mathbf{z}}],
\end{aligned} \tag{1.2}$$

where $p_\rho^2 = k^2 - \mathrm{p_z}^2 = p_x^2 + p_y^2$, p_j being the j-component of the linear momentum with $j \in \{x, y, z\}$. Furthermore, $J_m(\,\cdot\,)$ are the Bessel functions of the first kind, the amplitude $A(z) = \frac{1}{k}\sqrt{\frac{p_\rho}{2\pi}} i^{\mathrm{m}} \exp(i\mathrm{p_z}z)\frac{i}{\sqrt{2}}$, and $B_\pm = (k \pm \mathrm{p_z})$. The above modes form a complete orthonormal basis of transverse Maxwell fields.

In the collimated limit, when $\frac{p_\rho}{k} \to 0$ ($\mathrm{p_z} \approx k$ so that $B_+ \to 2$ and $B_- \to 0$), two of the polarisation components for each of $\mathbf{C}_{\mathrm{mp_z}}$ and $\mathbf{D}_{\mathrm{mp_z}}$ are very small, so that the helicity eigenstates can be approximated as the following circularly polarised beams:

$$\mathbf{C}_{\mathrm{mp_z}}(\rho,\theta,\mathrm{z}) \approx \sqrt{\frac{p_\rho}{\pi}} i^{\mathrm{m}+1} \exp(i(\mathrm{p_z}z)) J_{\mathrm{m}+1}(p_\rho\rho)\exp(i\theta(\mathrm{m}+1))\hat{\mathbf{r}}, \tag{1.3}$$

$$\mathbf{D}_{\mathrm{mp_z}}(\rho,\theta,\mathrm{z}) \approx \sqrt{\frac{p_\rho}{\pi}} i^{\mathrm{m}+1} \exp(i(\mathrm{p_z}z)) J_{\mathrm{m}-1}(p_\rho\rho)\exp(i\theta(\mathrm{m}-1))\hat{\mathbf{l}}. \tag{1.4}$$

The error in the intensity that is made with this approximation is of the order $(p_\rho/k)^2$.

This asymptotic property allows the preparation and analysis of light beams with well defined helicity using simple optical elements. The term "well defined" is used to refer to eigenstates of a linear operator. Experimentally, when the light can be described as a mode which is an eigenstate of that linear operator, except for possible negligible deviations caused by experimental imperfections, I will call the value of the operator "well defined".

The helicity operator can generally be written as $\Lambda = \frac{\mathbf{J}\cdot\mathbf{P}}{|\mathbf{P}|}$, where $\mathbf{J}$ is the total angular momentum and $\mathbf{P}$ is the linear momentum. Within electromagnetism, it can be rewritten in the instructive form of $\Lambda = \frac{\nabla\times}{k}$ for the case of monochromatic fields (with a convenient choice of units such that the vacuum permittivity and permeability are $\varepsilon_0 = \mu_0 = 1$). Using this form together with the fact that Maxwell's equations relate the electric and magnetic fields by curl operations, the transformation generated by helicity in free space can be shown to mix the roles of electric and magnetic fields in the following way:

$$\mathbf{E} \rightarrow \mathbf{E}\cos(\phi) - \mathbf{H}\sin(\phi) \tag{1.5}$$

$$\mathbf{H} \rightarrow \mathbf{E}\sin(\phi) + \mathbf{H}\cos(\phi), \tag{1.6}$$

where $\mathbf{E}$ and $\mathbf{H}$ are the electric and magnetic field, respectively, and $\phi \in \mathbb{R}$ is the continuous parameter that labels the group elements [1, 33, 34]. The above transformation is called duality transformation, and some settings of ϕ, such as $-\frac{\pi}{2}$, result in a full exchange between electric and magnetic fields. For a system to possess electromagnetic duality symmetry means that applying the duality transformation to an electromagnetic field that satisfies Maxwell's equations for the system, one again obtains a valid Maxwell field. In vacuum, this is always true. In contrast, material systems do not generally have this property, but only under certain conditions. Remarkably, unlike the symmetries corresponding to linear and angular momentum, a system is strictly dual, that is, it has duality symmetry, depending only on its material properties rather than its geometry: In piecewise homogeneous and isotropic media, symmetry under duality is achieved if and only if the ratio of the electric permittivity and magnetic permeability, and hence the geometry-independent intrinsic impedance, is constant for all subdomains [1, 30]. While the considerations about the duality transformation may at first appear like a purely mathematical exercise, the significant physical outcome is that within a dual system, the helicity of the electromagnetic field must necessarily be conserved. In general this does not imply zero scattering, but simply that no component with changed helicity is present in the scattered field. The preservation of helicity based on duality symmetry even holds in the near field, where the relationship between helicity and polarisation is non-trivial, and is illustrated in Fig. 1.6 for the example of subwavelength nanoscatterers.

The connection between the observable helicity and its symmetry duality can be exploited in light-matter interactions. On the one hand, the study of the electromagnetic helicity in interactions with matter provides us with a new source of information: The electric and magnetic properties of the material system. On the other hand, consideration of the duality symmetry enables a deeper understanding and control of the polarisation DOF.

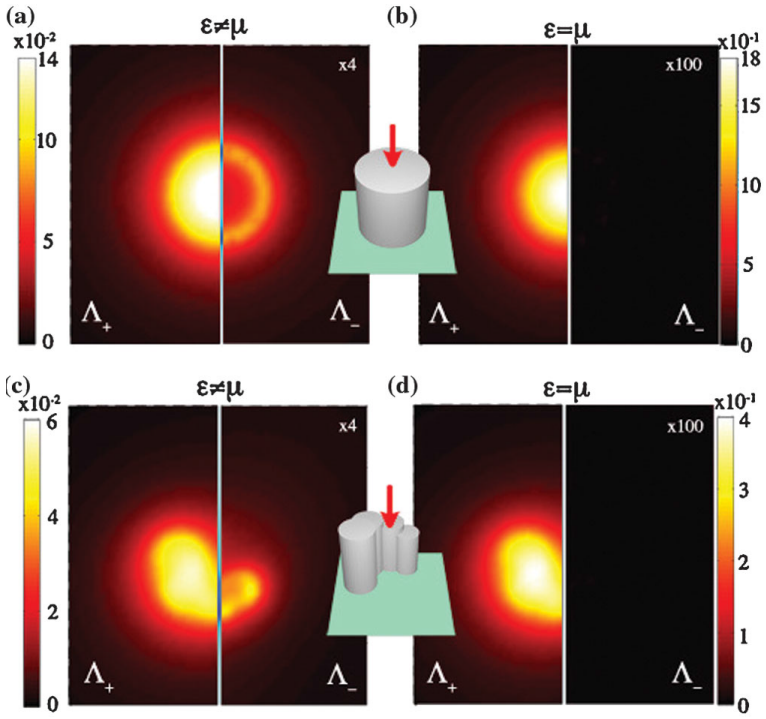

Figure 1.6: Numerical demonstration of the link between the geometry-independent duality symmetry and helicity. The simulations are of light scattered by four different objects, which can be grouped according to the presence/absence of cylindrical symmetry by rows, and of duality symmetry by columns. The incident light is a plane wave in a helicity eigenstate and for each case, the left half of the image shows the unchanged helicity component of the scattered field, while the right half shows the changed component. The results demonstrate that the preservation of the helicity of light depends only on the duality of the scatterer, and is independent of cylindrical symmetry. This figure appears in Ref. [1] and in Dr. Ivan Fernandez-Corbaton's PhD thesis [35]. Details about the simulations, which were performed by me, can be found in those references.

It would be interesting to manipulate a light beam while maintaining the helicity of the field. Yet, at optical frequencies it is very difficult to find a material with an intrinsic impedance matching that of air or vacuum. Although perfect duality symmetry is impossible to achieve without impedance matched materials, some systems can be designed in such a way that helicity is preserved to a very good approximation [36, 37]. One approach is to engineer the system such that it supports equal excitations of electric and magnetic multipolar moments. In this respect, metamaterials also show promise for providing a tailorable electric

and magnetic response [38, 39]. Very importantly from an experimentalist's point of view, microscope objectives designed to fulfil the aplanatic lens model do not change the helicity of light, either [30, 40]: An effectively dual response is restored by special anti-reflection coatings.

Naturally, to really add helicity to our toolkit, we require experimental methods of preparing, manipulating, and measuring helicity states of light. The following key points make the experimental handling of helicity simple: 1. Helicity can be manipulated and measured for collimated light beams through the polarisation of the field, and 2. using microscope objectives, it is possible to transform between paraxial and non-paraxial regimes without changing the helicity content.

With this knowledge, let us now consider a family of scattering problems depicted in Fig. 1.7, where a cylindrically symmetric but non-dual scatterer is probed by a light beam with well defined total angular momentum and helicity. It will allow us to better understand the experiment of the next section, which is an example of this type of scattering problem. The z-axis of the coordinate system is taken to be the axis of cylindrical symmetry. To prepare the beam, one can first create a collimated beam with a set azimuthal phase dependence and circular polarisation. This will correspond to a superposition over p_z of one of Eq. (1.3) or Eq. (1.4), where the choice of either $\mathbf{C}$ or $\mathbf{D}$ indicates the helicity and is determined by the polarisation, and the value of m indicates the fixed total angular momentum and is determined by the azimuthal phase dependence together with the helicity. Subsequently, the beam may be focused with a microscope objective, ensuring that the axis of symmetry coincides with that of the scatterer. This will change the transverse momentum distribution, i.e. the superposition over p_z values, but neither the well defined helicity nor the total angular momentum. The interaction of the light with the target will generally preserve the angular momentum of the light but not its helicity, because the scatterer is cylindrically symmetric but not dual. After the interaction, the light can be projected onto the two helicity eigenstates with a second microscope objective to collimate the beam, followed by a quarter waveplate (QWP) and linear polariser, where the polariser setting determines which helicity is selected.

What we can expect to happen in such an experiment based on symmetry considerations is that for one input mode, two output modes are obtained that differ in the helicity. The azimuthal phase dependence of the output modes is different: The unchanged helicity mode has the same phase dependence as the input mode, whereas that of the changed helicity mode differs by $\exp(i2\theta)$ or $\exp(-i2\theta)$, which is evident from a comparison of the modes $\mathbf{C}_{\mathrm{mp_z}}$ and $\mathbf{D}_{\mathrm{mp_z}}$ in Eqs. (1.3), (1.4).

It is not uncommon for people to divide the total angular momentum into a spin and

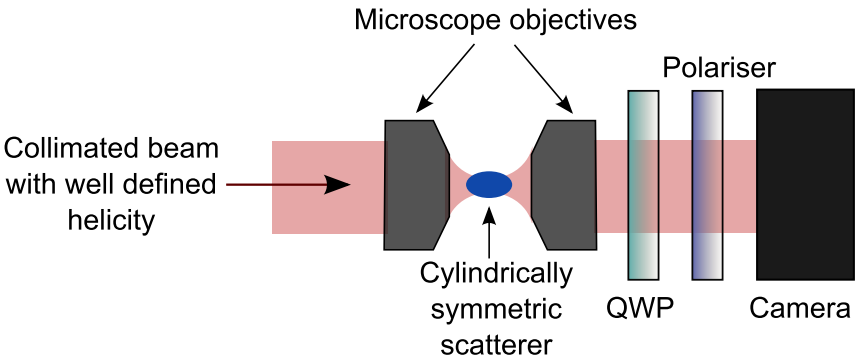

Figure 1.7: Sketch of an experiment in which a cylindrically symmetric but non-dual scatterer is probed by a light beam with well defined total angular momentum and helicity. Depending on the setting of the polariser behind the quarter waveplate (QWP), the unchanged or changed helicity component of the scattered field can be imaged.

orbital part, the spin being associated with the polarisation, and the orbital angular momentum with the azimuthal phase dependence of the beam [41], [42, Sec. 2]. A helicity change, which in the paraxial regime is associated with a changed polarisation and azimuthal phase, is therefore sometimes labelled as spin-orbit coupling [43]. However, when analysed in terms of the observables total angular momentum and helicity, linked with the corresponding symmetries rotational invariance and duality, it is easier to understand what happens [1, 30]. Furthermore, it is possible to predict that the phenomenon would not occur for the case of a dual scatterer. Such predictive power is lacking from a treatment in terms of spin and orbital angular momenta.

Now we have an understanding of what helicity is, and what role the corresponding duality transformation plays for electromagnetic fields in material systems. In the next chapter, we will encounter a concrete example of helicity change in a nanophotonics experiment.

Chapter 2

Interaction of classical light with nanoapertures

As mentioned previously, an understanding of the classical light-matter interaction problems is a prerequisite before venturing into the use of nonclassical light. As an example, in this chapter I study the classical light-matter interaction for a geometrically simple, yet already highly nontrivial system through two experiments. The first is presented in Section 2.3 and explores the role of helicity in nanophotonics experiments. The second is shown in Section 2.4, which addresses the question of how to position the sample with high precision. Section 2.3 is based on Ref. [31], and [1, 44] are also relevant for both Sections 2.3 and 2.4.

2.1 Nanoaperture sample

Nanoscatterers can come in many forms. As explained in Chapter 1, an analytic solution is known for spherical scatterers. However, this is no longer true for the case of cylinders with a finite length. The scatterer used for both experiments of this chapter is such a cylinder, but contrary to the common notion that a scatterer is a solid object, the cylinder is in fact a hole in an opaque film. An advantage of this geometry is that there is no need to separate the scattered field from a background when observing the transmitted light.

Two very similar samples were used, one for each experiment of this chapter. Each sample consists of a gold film on a glass substrate, with cylindrical nanoapertures in the gold, as illustrated in Fig. 2.1. The glass substrate is a 1 mm thick microscope slide made of fused silica. For the fabrication of the samples, first the gold was deposited on the glass by sputter coating. The sample used in the experiment of Section 2.3 has a gold thickness of 200 nm, while the one for the experiment of Section 2.4 has a thickness of 150 nm. Then a

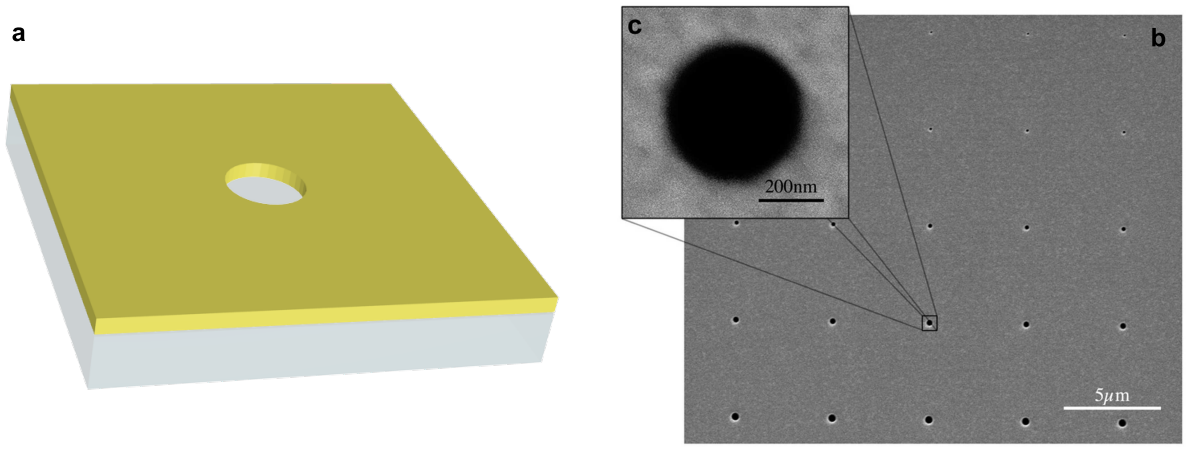

FIGURE 2.1: Nanoaperture sample. (a) Schematic, illustrating an isolated circular nanoaperture, which is the nanostructure effectively probed in the experiments of Sections 2.3 and 2.4. (b) Scanning electron microscope (SEM) image of an array of apertures, with the inset (c) showing a close-up of an example hole.

set of cylindrical holes was milled in the gold using a focused ion beam (FIB) machine, with hole diameters ranging between 150 and 630 nm, and distances of at least 5 μm between neighbouring holes. More details on the fabrication of nanoaperture samples can be found in Appendix A. When illuminated with light as in the experiments of Sections 2.3 and 2.4, the spot size of the probe beam is significantly smaller than this distance. Propagating surface plasmons can be excited, but they largely decay during their propagation along the gold surfaces before reaching other holes of the grid. For this reason, interaction between holes is negligible when one of the holes is illuminated, and we can consider the scatterer as an isolated nanoaperture in the gold-glass structure.

For the experiment detailed in Section 2.3, the diameters of all the apertures were measured using a scanning electron microscope (SEM), and 212 apertures with diameters between 150 and 580 nm and with ellipticities between 0 and 0.1 were selected.

2.2 Literature review

The motivation driving research on nanoapertures is twofold: First of all, from a general physics point of view the interaction of light with the structure is an interesting scattering problem in its own right. Perhaps it is the geometrical simplicity of the scatterer, given the cylindrical symmetry and the mirror symmetry about any plane containing the cylindrical symmetry axis, that has attracted people to the seemingly simple, yet surprisingly nontrivial

problem. Secondly, nanoholes enable the manipulation of electromagnetic and plasmonic excitations, so that this problem has a bearing on a number of nano-optical applications, including nanometric generation of surface plasmon polaritons [45], optical trapping [46], and reshaping of optical fields [47].

The general aim of the research is to build up knowledge of the scattered light when experimentally feasible and relevant input states are incident on the nanoapertures. Specifically, the properties of the transmitted light that one might typically be interested in are the transmitted power, the spatial distribution and polarisation properties of the transmitted light, and the excitation of plasmonic modes. Most investigations pay special attention to the dependence of the scattered field on the wavelength and hole size, although the details of the scattering also depend on the material and thickness of the film, as well as the polarisation and spatial mode of the incident light.

An understanding of the problem has been built up through three approaches: 1. development of analytic models, 2. numerical solution of Maxwell's equations, and 3. experiments. Each approach entails advantages and disadvantages: The full, general problem of the nanohole has not been solved analytically, so analytic models are based on approximations and assumptions. At the same time, they provide insight and predictive power. Approximations can be relaxed in numerical studies and of course, experiments are free of them. However, a generalisation of the observed behaviour can be difficult, while repeating the calculations or experiments for many different cases is time consuming.

Here, I will outline some key steps that took place in the research on nanoholes, mainly based on [48], to provide a rough overview of the body of work. A more comprehensive review, which is outside the scope of this thesis, can be found there.

In the seminal work of 1944, Bethe developed a model in which the system is replaced by a pair of electric and magnetic dipoles, assuming an infinitesimally thin perfect electric conductor (PEC) as the film [49]. The validity of the model is restricted to very small holes, meaning $kr \ll 1$, where k is the wavenumber of the incident light, and r is the hole radius. The transmission, normalised to the area of the hole, is predicted to scale as $\left(\frac{r}{\lambda}\right)^4$, λ being the wavelength of the light. Keeping the same assumptions, Bouwkamp refined the model by extending the transmittance as a series in kr to include higher order terms [50]. The finite thickness of the film was taken into account in a rigorous model by Roberts [51]. A new feature emerges, namely waveguide modes associated with the cylindrical hole. Similarly to optical fibres, a cut-off wavelength, above which the system does not support any modes, exists for this waveguide. Another significant step was the inclusion of the properties of real metals, which was accomplished in a numerical study by Wannemacher [52]. A notable difference between real metals and PECs is that real metals have an associated skin depth,

meaning that the electromagnetic field penetrates the metal to a small, but non-zero depth. Consequences are a redshift of the cut-off wavelength of the waveguide mode, such that a finite frequency mode exists for arbitrarily small holes (Catrysse *et al.* [53], Webb and Li [54]), and the fact that real metals support plasmonic modes. Although plasmonic modes are evanescent, they show up as resonances in the transmission spectra, and resonances were indeed observed by Degiron *et al.* [55] and Prikulis and colleagues [56], in experiments using silver and gold films, respectively.

Polarisation properties of the light-matter interaction as a function of the hole size have also been explored. In Ref. [57], Kindler and co-workers probed nanoapertures in silver with radially and azimuthally polarised vector beams in order to couple with the matching higher order waveguide modes. They observed significant differences in the transmission of the two input modes, which can be attributed to the unequal cut-off conditions of the respective waveguide modes. More recently, a study of light transmitted through nanoholes when probed with linear polarisation was presented by Yi *et al.* [58]. Focusing on the dependence on the hole size, particularly within the transition between deeply subwavelength holes and the limit of large holes, they show experimental results and provide analytic expressions of the polarisation-dependent far field angular spectrum of the transmitted light.

2.3 Helicity conversion of classical light when scattered from nanoholes

Somewhat similarly to the work of Yi *et al.* [58], the following experiment studies the spatial modes of the transmitted light, with attention on the polarisation DOF. Yi and co-workers used linearly polarised incident light and based on the mirror symmetries of the nanohole, they were able to measure the contributions from the different polarisations at the output by scanning along two planes. However, aside from mirror symmetries, the nanoaperture also possesses cylindrical symmetry. The cylindrical symmetry of the hole was matched in Ref. [57] by the use of azimuthally and radially polarised modes of light. The input beams of that experiment have well defined total angular momentum $J_z = 0$, and consist of equal-weight superpositions of the two helicities.

In the experiment of this section, the cylindrical symmetry of the system is similarly exploited, but instead of using azimuthally and radially polarised fields, we will use helicity eigenstates. I would like to remind the reader of the family of scattering problems discussed in part 1.2.3 of the introduction: A cylindrically symmetric, but non-dual, system is probed using light with well defined total angular momentum and helicity. The scattering process is

expected to preserve the total angular momentum, but not the helicity. This experiment is now shown for the example of the nanohole. Unlike in [57, 58], the incident light is circularly polarised, and then it is strongly focused (which is similar to [57] but not [58]). For the two output helicities, the spatial distributions are studied, as well as their relative power and their scalings with the hole size. Theory results were obtained with a semi-analytic method based on the Green's function [44].

2.3.1 Experimental design

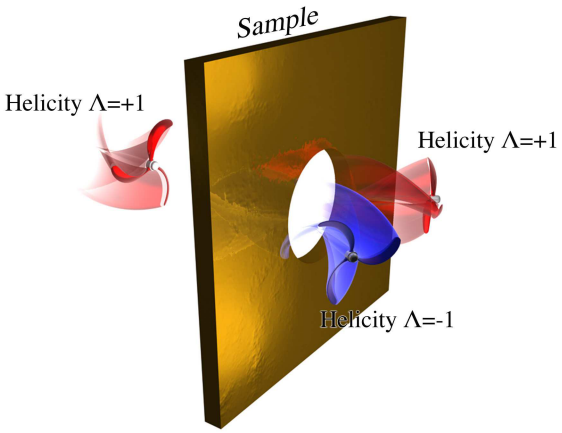

Figure 2.2: Sketch of the concept behind the experiment. Light with a well defined helicity, represented by a red propeller, impinges on a cylindrically symmetric aperture in a thin metallic film. The output light is analysed in terms of its helicity content, represented as red propellers when it is the same as the incident helicity, or blue ones with opposite handedness when the helicity is the opposite to the incident one.

The idea behind the experiment is illustrated by Fig. 2.2. Like the scatterers discussed in Section 1.2.3, the nanohole sample is cylindrically symmetric, but does not possess duality symmetry. In the experiment detailed below, we are interested in the helicity change induced by the scattering of light from the target. For this reason, an incident beam with well defined helicity $\Lambda = 1$ is chosen, and to simplify the resulting field, it is also ensured that the incident field has well defined z-component of the total angular momentum, $J_z = 1$. The wavelength of the light is also fixed and unchanged during the experiment, at 633 nm. This means that the analysis of Section 1.2.3 is applicable here. As discussed there, the beam is focused, and the z component of the linear momentum does not have a sharp value. In terms of Bessel beams from Eq. (1.2), the field incident on the nanoaperture can be written as a superposition of $\mathbf{D}_{1\mathrm{p}_z}$ functions, which all have $\Lambda = 1$ and $J_z = 1$, with different values of

the z-component of linear momentum, p_z. The transformation of a light beam interacting with the target can be represented by a transfer matrix between Bessel modes $(\mathbf{C}_{\mathrm{mp_z}}, \mathbf{D}_{\mathrm{mp_z}})$. Since for this nanophotonics experiment the transformation leaves the angular momentum invariant, the transfer between Bessel modes is only allowed between modes with the same index m. We therefore expect that the transmitted light will consist of $\mathbf{D}_{1\mathrm{p_z}}$ (which have $\Lambda = 1$, $J_z = 1$) and $\mathbf{C}_{1\mathrm{p_z}}$ (which have $\Lambda = -1$, $J_z = 1$), and we are particularly interested in the mode consisting of $\mathbf{C}_{1\mathrm{p_z}}$ functions, which is selected by means of a QWP and polariser after collimating the scattered field. The helicity change is attributed to the interaction of the light beam with the target. The presence of a vortex of charge two, which corresponds to the $\exp(2i\theta)$ term in the mode $\mathbf{C}_{1\mathrm{p_z}}$ of Eq. (1.3), is a signature of angular momentum preserving and helicity changing scattering [30].

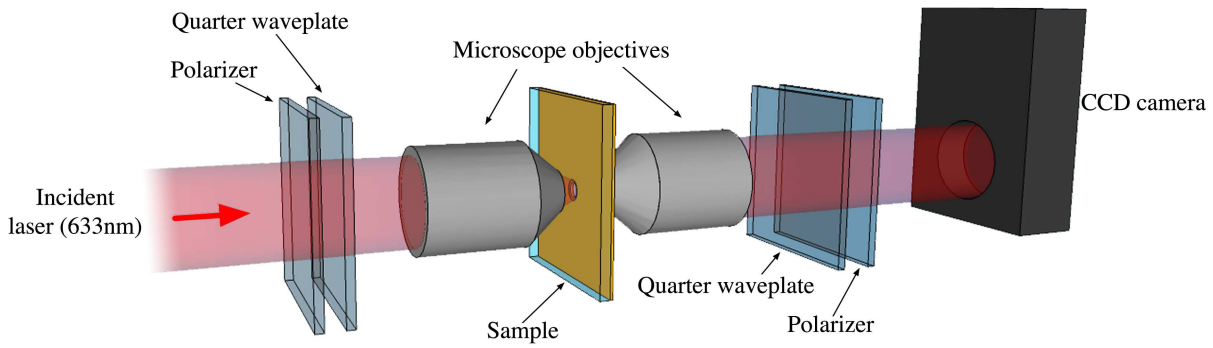

FIGURE 2.3: Experimental set-up. An incoming collimated beam is circularly polarised and focused to address the isolated nanohole, which is centred with respect to the beam with a nanopositioner. The transmitted light is then collected and analysed with a quarter waveplate, polariser, and a charge coupled device (CCD) camera.

Therefore, we know a priori that alongside an unchanged helicity mode, we can also expect a changed helicity mode, and we know what the modes qualitatively look like. As is often the case, however, the symmetry considerations only teach us about the existence of the modes, and not their relative weights. In this experiment the relative weights of the two helicity modes are investigated as a function of hole size.

2.3.2 Experimental method

The experimental set-up is illustrated in Fig. 2.3. The nanoapertures were probed with a continuous wave (cw) laser ($\lambda = 633$ nm). The preparation of the probing beam was achieved as follows: First, the laser beam was collimated and then a set of linear polarisers (extinction

ratio of 5×10^{-5}) and waveplates was used to obtain a LC polarisation. As detailed previously, when this collimated field is decomposed in modes that are eigenstates of J_z and Λ, the components with $J_z = 1$, $\Lambda = 1$ are dominant. This collimated beam was subsequently focused with a microscope objective with a numerical aperture (NA) of 0.5. Since the transformation of an aplanatic lens preserves helicity, a focused electromagnetic field with a well defined helicity could be prepared in this way. The focused field was then allowed to interact with one of the isolated nanoapertures. The nanoaperture was carefully positioned on the symmetry axis of the optical system by means of a set of piezo-stages. Subsequently, the scattered light was collected and collimated with another microscope objective of NA=0.9. Once again, this lens did not affect the helicity of the beam, so that after collimation it was possible to analyse the helicity with another set of waveplates and polarisers. In this way, two very different spatial profiles were obtained for scattered fields with $J_z = 1$, $\Lambda = 1$ and $J_z = 1$, $\Lambda = -1$. The light was detected with a charge coupled device (CCD) camera.

2.3.3 Results and discussion

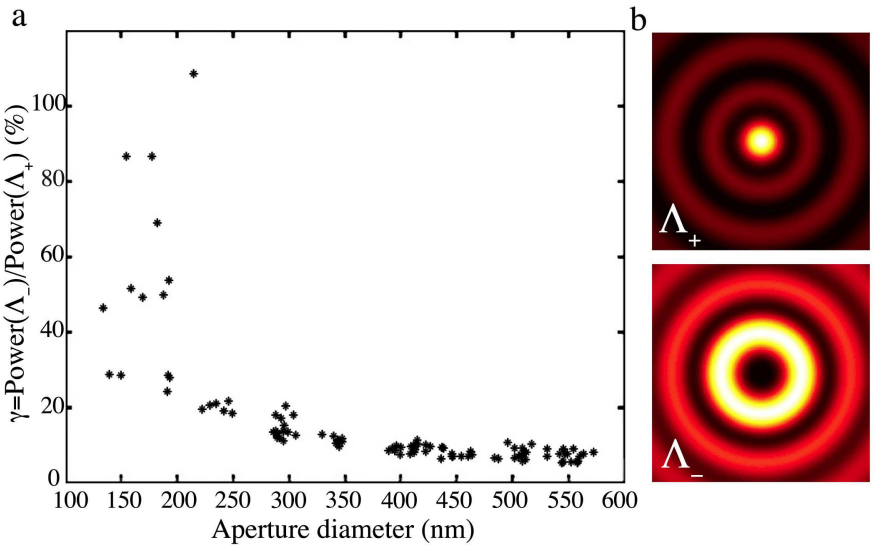

Figure 2.4: Helicity transformations through nanoapertures. (a) dependence of the ratio of the transmitted powers (changed helicity divided by unchanged helicity) on the aperture size. Uncertainties inferred from the power measurements for each hole are not shown, since they are much smaller than the variation between different holes, which stems from the geometrical characteristics of the individual holes. This variation appears as the spread in γ values for holes of similar size. (b) numerically calculated spatial intensity pattern for the unchanged and transformed helicity fields transmitted through a cylindrical aperture of 300 nm. Simulations were performed by Dr. Ivan Fernandez-Corbaton.

For all the measured holes, the transmitted light contained a component with changed helicity. This can be seen in Fig. 2.4 (a), which shows the power ratio between the two transmitted helicities, γ, as a function of the aperture diameters, d. The smallest conversion measured was for the largest holes, $\gamma_{580} = 0.08 \pm 0.02$. This can be compared with the limiting value of $\gamma_{\text{glass}} \approx 10^{-3}$, for the helicity transformation measured in the same sample through the glass alone, corresponding to an infinite aperture. Removing even the glass substrate, the helicity transformation by the focusing and collimating lenses alone was even smaller, of the order of $\gamma_{\text{lens}} \approx 10^{-4}$, which is consistent with the fact that perfect aplanatic lenses should preserve helicity. Fig. 2.4 (b) displays the typical spatial patterns for the two output helicities of the light scattered from a perfect cylindrical aperture, as calculated with a semi-analytical method by Dr. Ivan Fernandez-Corbaton [44]. He numerically checked that this output conserves angular momentum but, as can be seen, breaks helicity conservation (duality symmetry).

In order to test that the experimental results are consistent with the expected transformation of helicity and simultaneous conservation of angular momentum, the CCD images were analysed. Fig. 2.5 shows typical experimental results and their comparison with numerical calculations for two different aperture sizes. In the left column (Fig. 2.5 (a) and (d)) the components of the output field with the same helicity as the input, Λ_+, are shown. The observed field pattern is a typical Airy pattern arising from the subwavelength dimensions of the nanoaperture and the finite NA of the collection microscope objective, as expected from Fig. 2.4 (b). The central column (Fig. 2.5 (b) and (e)) shows the corresponding fields with opposite helicity, Λ_-. We can observe an absence of central intensity minima that correspond to phase singularities in Fig. 2.5 (a) and (d), and the presence of two such minima in Fig. 2.5 (b) and (e).

Let us see how the patterns arise. First of all, electromagnetic modes that are eigenstates of J_z have to be cylindrically symmetric. From Eqs. (1.3) and (1.4), it can be seen that for collimated beams with eigenvalue of $J_z = 1$ there are two cases, which differ in the helicity. In the dominant polarisation, the directly transmitted helicity mode has no phase singularity, and the helicity transformed mode has a second order singularity. Such a vortex of charge two is characteristic for an angular momentum preserving and helicity changing scattering, as explained in more detail elsewhere [30]. The two modes are consistent with the theoretical considerations presented in the Section 1.2.3 and with the simulations of Fig. 2.4 (b). The differences between the experimental results of Fig. 2.5 and the ideal case of Fig. 2.4 (b) for the helicity transformed transmission are due to the finite extinction ratios of the polarisers: In practice, a small leakage from the unchanged helicity to the transformed helicity could not be avoided, when imaging the transformed helicity. As a result of such a superposition,

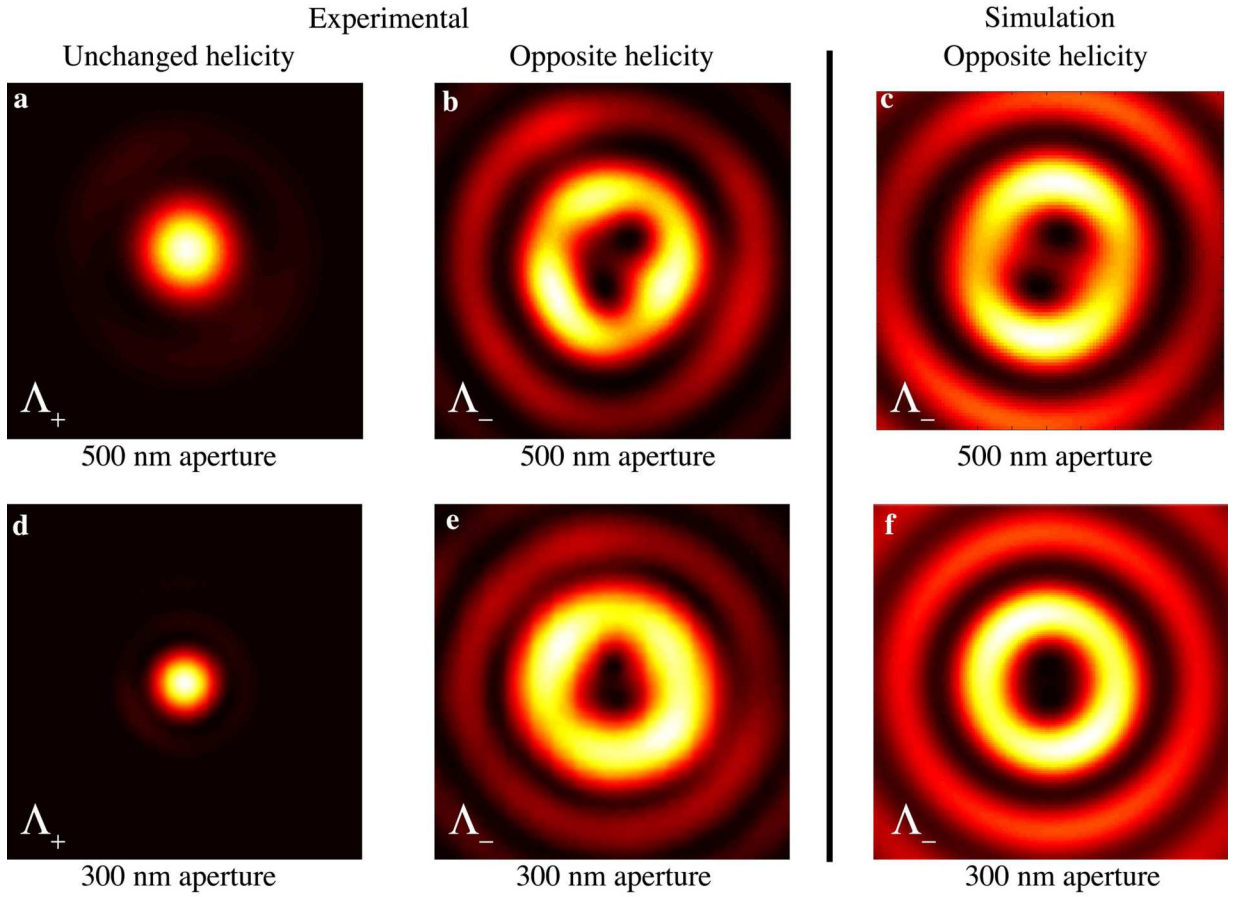

Figure 2.5: Projective measurement of helicity. Upper (lower) row shows the results for an aperture of 500 nm (300 nm). (a) and (d), Experimental results showing the transmitted light with helicity identical to the incident light. (b) and (e), Experimental results of transmitted light with opposite helicity. The cylindrical asymmetries are due to the finite extinction ratio of the polarisers. This is supported by the patterns numerically simulated by Dr. Ivan Fernandez-Corbaton, (c) and (f), where the asymmetry appears only after including the experimental parameters of the optical components used.

the second order singularity splits into two singularities of order one. Thus, the intensity pattern is no longer cylindrically symmetric. In order to demonstrate this point, Fig. 2.5 (c) and (f) show the coherent superposition of numerically calculated images of unmixed modes (as those of Fig. 2.4 (b)), with relative amplitudes given by the extinction ratios of the set of polarisers, 5×10^{-5}. In conclusion, the measurements are consistent with the fact that in the scattering process, the angular momentum is conserved, but the helicity is not.

According to the ideas presented in Section 1.2.3, the observed helicity change implies that electromagnetic duality is broken in the sample. This is to be expected because the intrinsic impedances in each subdomain are not equal, i.e. it is not true that $\frac{\varepsilon_i}{\mu_i}$ is the

same for every subdomain i with relative permittivity ε_i and permeability μ_i. Light-matter interactions in which duality is broken, whether the scatterer is a metal or dielectric, would generally lead to non-conservation of helicity. While the conservation of helicity only depends on the optical properties of the materials, when the duality symmetry is broken, the amount of helicity transformation may also depend on all the other characteristics of the scatterer. This is evident from the results displayed in Fig. 2.4 (a), where the helicity transfer is seen to depend on the aperture size, with the material properties unchanged. In order to identify the mechanism of duality breaking in this experiment, it is instructive to first consider the multilayer system air-glass-gold-air without the nanoaperture. Duality is obviously broken by just the multilayer alone, but the helicity transfer in the absence of the nanoaperture is very small. The numerical calculations predict helicity transfers around 4×10^{-4} for this case, assuming perfectly helicity preserving lenses. The experimental observation of much higher transformation ratios must hence be tied to the nanoapertures.

Let us see how this can be the case. The transmission and reflection in a planar multilayer system is best studied using plane waves. For a single plane wave with momentum $\mathbf{k}$, the two helicity states are the two states of circular polarisation, and can be obtained by linear combination of its $\mathbf{s}$ (transverse electric) and $\mathbf{p}$ (transverse magnetic) components: $\mathbf{s} \pm \mathbf{p}$. See [30, Appendix A] for a general derivation of this relationship, which also applies to multipolar fields and Bessel beams. Different scattering coefficients for $\mathbf{s}$ and $\mathbf{p}$ will hence mix the two helicity modes. A similar idea has also been applied to the analysis of resonances in spheres [59], where the fields are most suited to a multipolar decomposition. Returning to the planar multilayer, if the system presents a resonance for either $\mathbf{s}$ or $\mathbf{p}$, the helicity transfer will be enhanced in its vicinity. A pure $\mathbf{s}$ or pure $\mathbf{p}$ mode is mirror symmetric and consists of an equal weight combination of the two helicities. Hence, it strongly breaks helicity conservation (duality symmetry) when it is excited by a field with well defined helicity. The system indeed presents several resonances for non-propagating modes [44]. In the case of the multilayer structure, surface modes present such resonances that can be excited through the scattering of the incident field by the nanoaperture. Since they have equal contributions from the two helicities, this produces an asymmetric response of the surface modes with regard to the transmitted $\mathbf{s}$ and $\mathbf{p}$-polarised components. This electromagnetic asymmetry dramatically enhances the helicity transfer, even in the propagating modes, and makes it experimentally detectable. According to this explanation, the helicity transfer should increase for modes in the proximity of the resonance, i.e. for large transversal momenta. This explains the trend in Fig. 2.4 that smaller holes present a larger γ value: Smaller holes have a higher coupling to large transversal momenta, and in particular to the surface modes. One can then conclude that the nanoaperture plays a crucial role for the helicity transfer because it allows

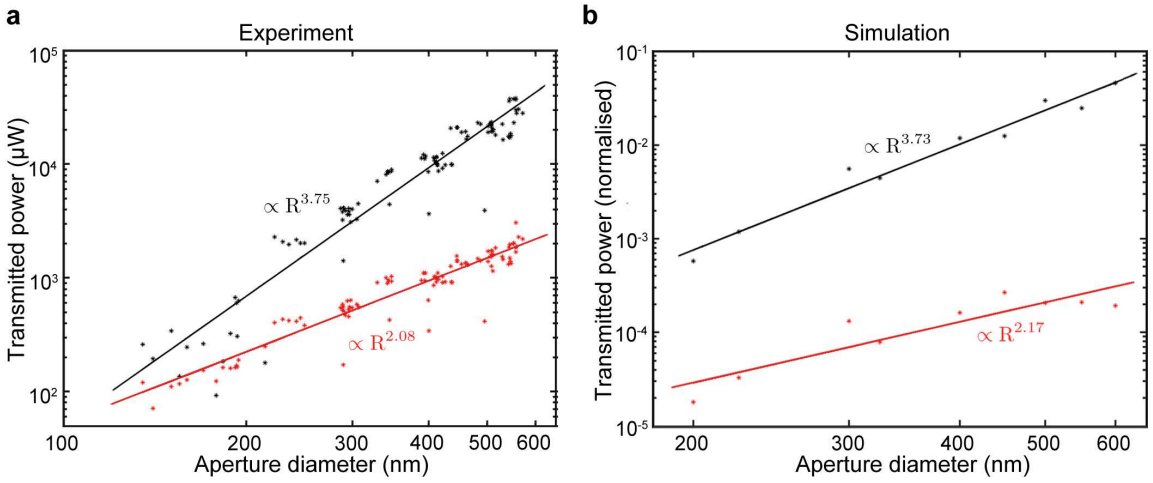

Figure 2.6: Scaling of the different components of the transmitted beam. Panel (a) contains experimental results, while (b) shows simulation results by Dr. Ivan Fernandez-Corbaton, which were obtained for a perfectly flat 200 nm thick gold layer. The unchanged helicity component ($\Lambda = 1$, in black) has a faster scaling with the aperture diameter, d with $d^{3.75}$ and $d^{3.73}$ for the experimental and simulation values, respectively. The transformed helicity component ($\Lambda = -1$, in red) conversely shows a slower scaling with $d^{2.08}$ and $d^{2.17}$ for the experimental and simulation values. Similarly to Fig. 2.4, error bars for the experimental results are omitted, because the visible variation between holes of similar size is dominant compared to the uncertainties inferred from the power measurements for each hole.

the coupling of the incident field to resonances of the multilayer structure.

A further interesting question is how the transmitted power scales with the aperture size. Since the helicity modes of the transmitted field were measured separately in this experiment, it allowed to study the scaling of the different components of the transmitted field, $\mathbf{D}_{1p_z}$ and $\mathbf{C}_{1p_z}$, with aperture size. As shown in Fig. 2.6, a considerably different scaling law was observed for the unchanged and changed helicity components. The reasons for this difference between unchanged and changed helicity components are not obvious, but one of the potential reasons may be the dominant multipolar moments that are at play for each component. The difference is especially interesting considering the behaviour expected for the limit of very small hole diameters: As discussed in Section 2.2, the scaling with aperture size of the power transmitted in the limit of very small holes, albeit for the case of an infinitely thin PEC, was one of the main results of the paper by Bethe [49]. Bethe found that in such a situation, it is possible to describe the hole solely with an electric dipole moment perpendicular to the plane of the hole and a magnetic dipole moment lying in the plane of the hole, both of them scaling as d^6 (not normalised by the area of the hole). Due to its symmetry, the incoming field with $J_z = 1$ is unable to induce an electric dipole moment

with such orientation, leaving only the magnetic dipole moment. Since a field emitted by a magnetic dipole is an equal weight superposition of the two helicities, this model would predict a value of $\gamma = 1$. The scaling of the total transmitted power, as well as of each of the helicity modes, would be d^6. Very small holes of the order of $\lambda/10$ or below were not probed within this experiment, but the trend of the smallest holes having large γ values is already evident in Fig. 2.4. No analytic model is known that predicts the γ value for arbitrary hole sizes. The observed difference between the scaling of the two helicity components for larger holes might be due to the higher multipolar moments that start to play a role with increasing hole size.

2.4 Nanopositioning

In this section I will describe a second experiment that makes use of the interaction of classical light with nanoholes. In fact, the experimental set-up is kept the same as in Section 2.3. The helicity conversion measurements of the previous experiment were taken with the nanoholes positioned on-axis relative to the incident beam. Now we will look at a method with which this transverse position of the sample can be identified. A precision of approximately 10 nm is demonstrated in the implementation below.

2.4.1 Problem description

In nanophotonics experiments such as the one described above, the position of the scatterer relative to the probe beam strongly affects the scattered fields. These experiments therefore rely on the ability to position the samples in a reproducible manner. Due to the remarkable progress in the field of nanotechnology, some fabrication processes and super-resolution microscopy techniques also require nanometre-scale accuracy in the positioning of samples [60–62]. Nanopositioning is always possible if one can locate a reference position and execute controlled translations. Then a position of interest can be reached by starting from the reference and translating the sample in a particular way [63, Chapter 8]. The technique proposed in this section addresses the problem of identifying a reference position. In contrast, the ability to execute a controlled nanoscale movement of the sample is assumed as a given, since solutions for this are commercially available. In the experiment below, translations are realised by the translational piezo-electric stage on which the sample is mounted.

Although it might appear like a simple task at first, the identification of a reference position is nontrivial down at the nanometre scale. As an example, let us consider the task of identifying the position at which a cylindrical nanoaperture is centred with respect to the

probe beam. A common approach would be to maximise the transmitted power. However, given that the diffraction limit imposes a lower bound on the spot size of the probe light, the relative change in power is typically quite small for a 10 nm displacement of the sample. More sophisticated versions of the same idea are also possible, such as performing a scan where the power is measured at many different transverse positions, and determining the centre of the distribution through a statistical fit. Nanopositioning methods based on the transmitted power are indeed possible. Yet, the information from the power at any single position is limited: Even if the sample happened to be exactly at the reference position, one would not generally recognise this without prior calibration or comparison with other locations. The analysis based on a linear scan in one direction would still entail similar difficulties, because of the uncertainty whether the reference position is at the maximum of that line or actually on a parallel line. A scan of an area is required. This is essentially because power measurements lack directional information and the identification of the reference is calibration-dependent.

Directional information can be gained by measuring the intensity of the scattered light as a function of transverse position in the detection plane. This is done in the case of a quadrant photodiode (QPD), which is a versatile position sensing tool applicable to a variety of systems. The sensitivity of a differential signal obtained from different transverse regions in the measured field depends on how directional the scattering is as a function of the sample displacement. Several recent works on position sensing have focused on optimising the directional scattering through the interference of different contributions to the measured field, e.g. from electric and magnetic dipole modes, or from scattering off a particle and reflection from the substrate [64, 65]. The signal can be enhanced by careful choice of the spatial mode, polarisation, and wavelength of the incident light, as well as the properties of the scattering system.

2.4.2 Symmetry-based determination of a reference position

Here I take a slightly different approach. Instead of focusing on the optimisation of the specific system at hand, the scattering by a nanohole, the aim is to construct a versatile technique. As the idea rests on simple symmetry considerations, it can also be generalised to other structures besides the nanohole. As a matter of fact, let us start by considering a very general optical system defined by an incident electromagnetic field and a scatterer in a fixed reference frame. The key behind the positioning technique is that when the system has certain symmetries, translations of the scatterer can be related to rotations of both scatterer and light. For a general incident field and a scatterer that is translated relative to the field,

there is no straightforward relation of the scattered field before and after the transformation (see the left case of Fig. 2.7). However, the problem is simplified significantly when both the incident field and the scatterer individually exhibit cylindrical symmetry. This symmetry of incident field and scatterer is the requirement we will place on the system. In that case any translation which leaves the distance between the axes of symmetry of scatterer and incident field unchanged is equivalent to a rotation of the complete physical system (shown on the right side of Fig. 2.7). From this argument, it is evident that the scattered fields before and after the translation of the scatterer are also related by that same rotation. The idea of the technique is quite generally to use the overall symmetric position, at which the two axes of symmetry coincide, as the reference, and to assign a measure of asymmetry and an angle based on the scattered light distribution. The measure of asymmetry provides information about the distance to the reference position and the angle about its direction. The reference position corresponds to an angle singularity: The angle is undefined at the reference, and all angles can be found in its neighbourhood.

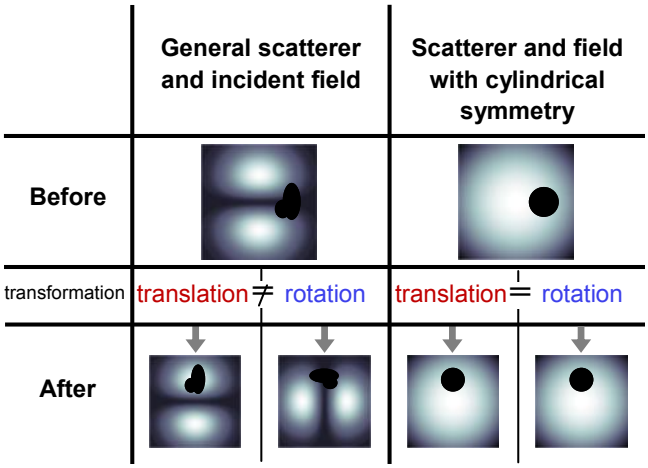

FIGURE 2.7: Relationship between two optical systems where the scatterer has been translated. Left column: General scatterer and incident field. The translation of the scatterer cannot be replaced by a rotation of the system. Right column: Cylindrically symmetric scatterer and incident field. If the translation occurs between two positions of equal distance from the center of the incident beam, the translation is equivalent to a rotation of the whole system.

For the practical implementation of this idea, two points in the scattered field are located based on some rules that could take many different forms and will be discussed later on. The two points will define a line (connecting them) and thus an angle (α) with respect to a fixed axis of the image frame. For transverse scatterer positions (x, y) along any circle with non-zero distance from the central axis of the incident field, it is clear that the full range of angles, 2π, is traversed. The angle as a function of transverse position of the scatterer takes on the form $\alpha = \arctan(\frac{y-y_0}{x-x_0}) - \alpha_0(r)$, where (x_0, y_0) is the central reference position, α_0 is

the angle at which the transition from 0 to 2π occurs and this can generally be a function of the distance from the centre, $r = \sqrt{(x - x_0)^2 + (y - y_0)^2}$.

2.4.3 Implementation

I now show a proof-of-principle experiment demonstrating how the nanoaperture can be positioned at the reference position without any calibration by identifying the angle singularity obtained from the image analysis. The experimental set-up is the same as in Section 2.3, and is shown in Fig. 2.3. The position of the sample relative to the incident beam is controlled using a translational piezo-electric stage, and images of the changed helicity component of the transmitted light are taken with a CCD camera. Evidently, the circular nanoaperture fulfils the cylindrical symmetry requirement on the scatterer, and the Gaussian incident beam in a helicity eigenstate also conforms to the cylindrical symmetry requirement. Hence, for such a system translations of the sample can be related to rotations of the system and as explained above, a reference position can be defined by identifying the angle singularity.

In this particular implementation, the recorded intensity patterns typically contain two local minima corresponding to the charge two vortex that has split in two, which is already familiar from Fig. 2.5. At off-centre positions of the nanohole, the patterns can be more skewed, an example of which is shown in Fig. 2.8. The following two points, not to be confused with the two intensity minima (labelled $\mathbf{q}_{\mathrm{min}1,2}$), are retrieved from each image to determine the position of the sample: the midpoint $\mathbf{p}_1$ between the two minima of intensity and the position of the centroid $\mathbf{p}_2$, weighted with respect to the intensity value:

$$\mathbf{p}_1 = \frac{1}{2}(\mathbf{q}_{\mathrm{min}1} + \mathbf{q}_{\mathrm{min}2}) \tag{2.1}$$

$$\mathbf{p}_2 = \frac{\sum_{\mathrm{A}} \mathbf{r}\, I(\mathbf{r})}{\sum_{\mathrm{A}} I(\mathbf{r})}, \tag{2.2}$$

where A is the region of interest of the image, $\mathbf{r}$ is a position in the image, and $I(\mathbf{r})$ is the intensity value at position $\mathbf{r}$. Using these two points ($\mathbf{p}_{1,2}$), their distance ($d = |\mathbf{p}_1 - \mathbf{p}_2|$) and the angle ($\alpha$) between the edge connecting the two points and the horizontal (parallel to the x-axis) are calculated. In principle, two different identifiable points could also be used as $\mathbf{p}_{1,2}$ in the data analysis to yield a distance d and angle α. The use of the intensity-weighted centroid and midpoint between the intensity minima is merely one example, and alternative rules that identify two points could have been chosen. In fact, the use of the changed helicity component is not necessary for the technique to work, either. It is simply one particular implementation that was found to work well.

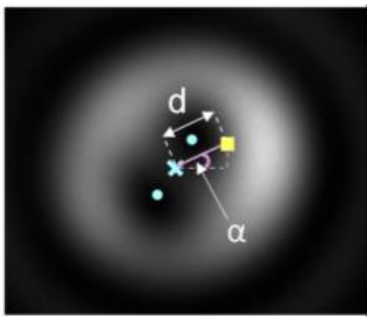

FIGURE 2.8: Image analysis. The quantities extracted from the image of the changed helicity mode are demonstrated on an example pattern. The midpoint $\mathbf{p}_1$ (blue cross) between the minima of intensity $\mathbf{q}_{\text{min}1,2}$ (blue dots) is determined, along with the intensity-weighted centroid of the image, $\mathbf{p}_2$ (yellow square). The distance (d) between the midpoint and intensity-weighted centroid, and the angle (α) between the edge connecting these two points and the horizontal are then calculated.

The two points $\mathbf{p}_{1,2}$ coincide when the nanoaperture and the incident field are perfectly aligned. This results in a zero distance d and undefined angle α. Conversely, when the sample is displaced in the transverse plane, the cylindrical symmetry of the overall physical system is broken and $\mathbf{p}_{1,2}$ do not coincide any more [40]. The field pattern of Fig. 2.8 is an experimentally obtained example image corresponding to this scenario and the non-zero distance and defined angle are clearly results of asymmetry.

Imperfections of the optical components can prevent the incident beam within a real experiment from being a pure J_z eigenstate, and therefore from being cylindrically symmetric. In Appendix B it is shown that the typical mixing of input modes does not affect the reference position. In addition, slight breaking of the cylindrical symmetry of both the incident beam and the nanoapertures also occurs due to other experimental limitations. In the following, experimental results are presented which show that the imperfections do not impede the successful realisation of the method. Using the translational piezo-stage with a nominal repeatability of 5 nm, scans were carried out over a square grid extending over 200×200 nm of x- and y- positions of the sample with stepsize 10 nm for both coordinates, taking an image of the changed helicity field pattern at each position. While the stepsize is limited by the repeatability of the positioner, the 200 nm range of the measurements is for presentation purposes only. The spot size of the input beam is the fundamental limitation to the measurement's range of the technique.

Experimental results for hole diameters of 500 nm and 630 nm are shown in Fig. 2.9. The distance d and angle α obtained from the image analysis are presented as a function of the x- and y- positions. As expected, there exist positions at which the distance decreases to zero and the angle exhibits a singularity. These are the reference positions, and their

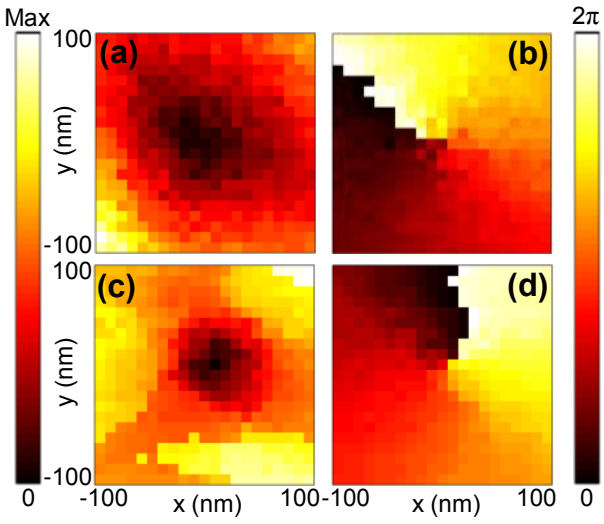

FIGURE 2.9: Experimental results of scans over transverse positions of the sample. The scans extend over an area of 200×200 nm, with each element of the colourmetric surface plots corresponding to the stepsize of 10 nm. The top and bottom rows correspond to results for nanoapertures with diameters of 500 nm and 630 nm, respectively. (a) and (c): Distance d between midpoint of intensity minima and the intensity-weighted centroid (arb. units). (b) and (d): Angle α between the horizontal and the edge connecting the midpoint and the intensity-weighted centroid.

resolution of approximately 10 nm is a reflection of the precision achievable with the set-up. The experimental results can also be compared with Fig. 2.10, where theoretical results from a scan similar to the experimental case are shown. In the simulations, which were performed by Dr. Ivan Fernandez-Corbaton, a nanoaperture diameter of 630 nm is used, and polarisation imperfections of the incident feld and projective measurement comparable to the experimental conditions are incorporated. The simulations are in close agreement with the experimental results. The resolution of the angle singularity in Fig. 2.10 is also 10 nm, but this is simply because the stepsize was chosen to match the experimental one; it can be improved by decreasing the stepsize.

Let us take a closer look at the precision. The experimentally obtained precision could be limited by a number of potential factors, depending on the exact implementation. One can separate these factors in three categories: Mechanical instabilities, imperfections of the set-up, and image related factors. Clearly, the mechanical instability of the set-up does not limit the precision of the technique, but only our ability to assess the precision. On the other hand, imperfections of the set-up, such as elliptical samples or faulty waveplates, and the signal-to-noise ratio of the imaging system are the ultimate factors limiting the precision of a particular set-up.

To measure the overall stability of the system, a series of images was recorded using the

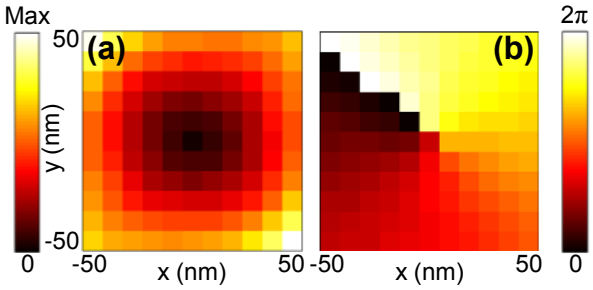

FIGURE 2.10: Numerical results of scan over transverse positions of the sample. Probing a 630 nm diameter nanoaperture, the scan extends over an area of 100 × 100 nm, with each element of the colourmetric surface plot corresponding to the stepsize of 10 nm. (a): Distance d between midpoint of intensity minima and the intensity-weighted centroid (arb. units). (b): Angle α between the horizontal and the edge connecting the midpoint and the intensity-weighted centroid. The simulations were performed by Dr. Ivan Fernandez-Corbaton

630 nm aperture, moving the piezo-stage repeatedly between a central position and ± 20 nm in x and y from that position. This resulted in five groups of images, one for each of the different nominal stage positions. After extracting α and d from each image, the position of the sample in the x-y plane (x_Δ, y_Δ) relative to the central mean position was inferred. The data were mapped to orthogonal axes using $\frac{d}{c}\cos(\alpha + \alpha_0)$ for the horizontal axis x_Δ and $\frac{d}{c}\sin(\alpha + \alpha_0)$ for the vertical axis y_Δ, where α_0 is the angle at which the transition from 0 to 2π occurs. The mapping assumes the underlying functions $\alpha = \arctan(\frac{y-y_0}{x-x_0}) - \alpha_0$ and $d = c\sqrt{(x-x_0)^2 + (y-y_0)^2}$, where (x_0, y_0) is the central reference position and c is a calibration constant. It is assumed that the phase α_0 is independent of the distance, an approximation that is valid sufficiently close to the singularity, as can be seen from Fig. 2.9. For the distance function it is assumed that within this range of 40 × 40 nm, d can be approximated as a linear function of the distance from the central position, the validity of which was confirmed using least squares fitting of the data presented in Fig. 2.9 (c). Then the axes were calibrated based on the average values of the groups of data points: The origin was set at the mean position of the central group. The calibration constant c was obtained from the mean values of the groups from having moved the stage ±20 nm in the x and y direction. The data from the stability analysis are shown in Fig. 2.11, where the five groups of data points are represented by different symbols. The standard deviations in x_Δ and y_Δ are 4.5 nm and 5.4 nm, respectively. It should be noted that the data sets shown in both Fig. 2.9 and Fig. 2.11 are based on measurements involving a movement of the stage between acquisitions. Repeated acquisitions without stage movements would provide a smaller spread in position.

From the stability measurements, the experimental precision of 10 nm was therefore

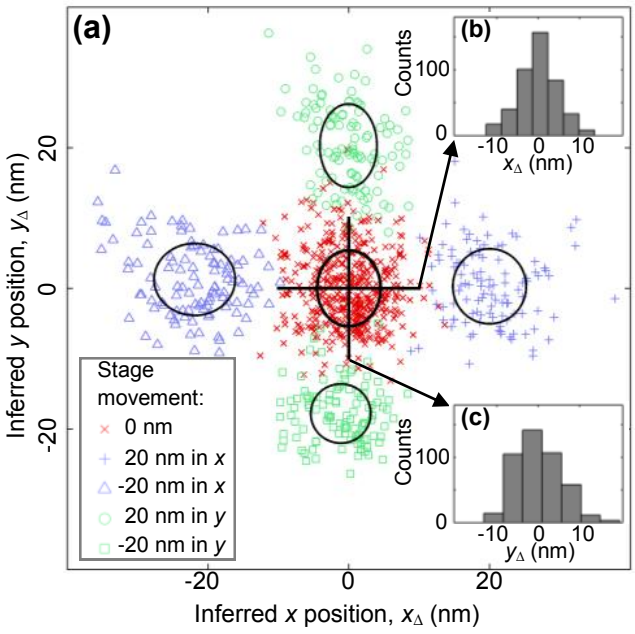

FIGURE 2.11: Stability measurements. (a): Five groups of data sets, which were obtained for the translational piezo-electric stage at five nominal positions. d and α values were extracted through image analysis, and the data points were subsequently mapped on orthogonal axes using $\frac{d}{c}\cos(\alpha+\alpha_0)$ for the horizontal axis x_Δ and $\frac{d}{c}\sin(\alpha+\alpha_0)$ for the vertical axis y_Δ, with the calibration constant c determined through the mean values of the groups. α_0 is the angle at which the transition from 0 to 2π occurs for α as a function of transverse sample position, examples of which are shown in Fig. 2.9. The mapping yielded inferred x-y positions relative to the central position. The ellipses represent the standard deviation for x_Δ and y_Δ values. The insets (b) and (c) are histograms of the x_Δ and y_Δ values from the group of points belonging to the central stage position.

found to be of the same order as the repeatability of the nanopositioning stage. This means that intrinsic limitations to the precision of the method from other set-up or image related factors are not identifiable in this current implementation.

Revisiting the motivation behind the metrology scheme on the one hand (Section 2.4.1), and the results of Fig. 2.9 on the other hand, something might strike the reader as strange. Fig. 2.9 shows scans over different transverse scatterer positions, and such scans would be needed for nanopositioning based on power measurements, too. While a whole scan is shown for the proof-of-principle experiment, directionality information, which is missing from power measurements, resides in the angle α. As a consequence, after calibration, a single measurement reveals information about the direction of the angle singularity. Aside from that, the angle singularity is recognizable even without any calibration. An advantage of the proposed technique compared to position sensing using a QPD, where the reference position of the sample depends on the position of the detection apparatus, is the independence of the

reference from the camera position.

2.5 Conclusion

The interaction of classical light with nanoapertures has received attention over the last seven decades, with progress reflecting the advances in computational power, as well as fabrication and near-field imaging capabilities throughout the years [48, 66].

The results presented in Section 2.3 of this chapter add to the body of work by showing the dependence of the helicity transformation on the aperture size. Apart from the information the experiment provides about the specific system of the nanoaperture, it also showcases several more general things. In contrast to the more common approach of employing symmetry arguments to conveniently reduce the amount of computation or measurements required, here the complete experimental design and analysis are centred on the concept of symmetries and conserved quantities. This allows the systematic study of a phenomenon that would typically be labelled as spin-orbit conversion: The observables total angular momentum and helicity are used instead of spin and orbital angular momentum, allowing an analysis in terms of rotational and duality symmetries. In order to do so, one needs to control the helicity of light in the nonparaxial regime, where its relationship to polarisation is more subtle than in the paraxial regime. It is demonstrated how this can be achieved with conventional optical elements.

Continuing with the theme of symmetries and with the same physical system, a simple, low-cost technique for nanopositioning of nanohole samples was introduced in Section 2.4. An intuitive explanation was presented for the underlying mechanism, along with experimental results that demonstrate the successful implementation of the method achieving a deeply subwavelength precision of 10 nm. The technique has straightforward applications in nanophotonics experiments for testing the alignment and navigating on the sample. Based on the same symmetry considerations, the technique can be adapted to other types of nanostructures with cylindrical symmetry.

Chapter 3

Manipulation and measurement of the spectral biphoton wavefunction

3.1 Introduction

Optical quantum metrology can draw its enhanced performance over what is achievable classically from the use of nonclassical light as the probe [21]. While a number of different quantum states are known to be suitable for this purpose [67], I will focus on photon pairs as a resource. This decision is based on the fact that the process of SPDC constitutes a readily available source of photon pairs, which we have a good understanding and control of [68, Sec. 12.2] [1]. It is interesting to note that due to the lack of distinction at such low number of photons, a photon pair can simultaneously represent different families of quantum states. For instance, the state $\frac{1}{\sqrt{2}}(|2,0\rangle + |0,2\rangle)$, where $|m,n\rangle$ stands for a pure two-mode state with m photons in the first mode and n photons in the second mode, can be considered a NOON state, but also a Holland-Burnett (HB) state. A HB state is the state that is obtained at the output of a beam splitter when a twin Fock state with equal photon numbers is incident on the two input ports [69, 70]. So although the use of photon pairs, which is at best only capable of providing a modest improvement of the precision [2], is not expected to be competitive in the long run, it makes for an instructive example and good starting point.

In order to successfully use light for probing an unknown object, a precise control and knowledge of its state is of benefit. The spectrotemporal properties of the photon pairs are especially important in applications that rely on specific energies and/or timings (e.g. ones

[1] In fact, the state created by SPDC is a superposition of vacuum, the desired photon pairs, and multiple pairs. However, the output is post-selected for the presence of photons, and multiple pair emission is negligible for the pump powers of interest here.

[2] see Section 4.2

that involve particular energy transitions or up-conversion), or indistinguishabiliy (e.g. those based on quantum interference) [71–75].

A set of tools and techniques, including spectrometers, monochromators, spectral filters, and pulse shapers, are available to enable extensive experimental control of the frequency content of light. Based on this multitude of options, one may at first be led to believe that experimentally characterising the spectrotemporal state ought to be easy. However, the measurement tools operate in the frequency domain, which is only half the story. A full characterisation requires determining complex amplitudes in either the frequency or time domain, or simultaneous knowledge of the probability distributions in the frequency and time domains, from which the phase can be retrieved with the Gerchberg-Saxton algorithm [76]. In the time domain, a gap exists between our typical experimental timing resolutions, which are limited by electronic jitter and are on the order of tens of picoseconds or more, and the time frames of interest, which can commonly be on the order of or below picoseconds [77, Sec. 34.3.2.1], [78, 79].

In Section 3.2 of this chapter, which is based on [2], I will show a way to influence the temporal properties of the SPDC biphoton wavefunction by spatial manipulations. The mechanism relies on correlations between the spatial and spectral DOF, so-called spatio-temporal correlations. Then in Section 3.3, which follows [3], I will present a new method to measure the complex spectral wavefunction.

3.2 Manipulation of the time delay between SPDC photons based on spatio-temporal correlations

This subsection presents the model and mechanism behind an effect that manifests itself as a surprising change in the temporal delay between two photons in an SPDC pair. The effect takes place for the case of type-II SPDC with noncritical phase matching, using a cw pump and focused detection mode, when longitudinally displacing the crystal or collection lens. A possible implementation is illustrated in Fig. 3.1. The displacement of the crystal or collection lens results in a change of the time delay distribution, including its mean value. Owing to the orthogonal polarisations of the two photons in type-II SPDC, the photons have different group velocities within the birefringent down-conversion crystal. As a result of this difference, they acquire a relative time delay during the propagation through the crystal. The reason a change in time delay is surprising is the fact that assuming an undepleted pump, SPDC is a coherent process in which photons are created with equal probability all along the crystal. This means that even for a focused pump, the probability of pair creation

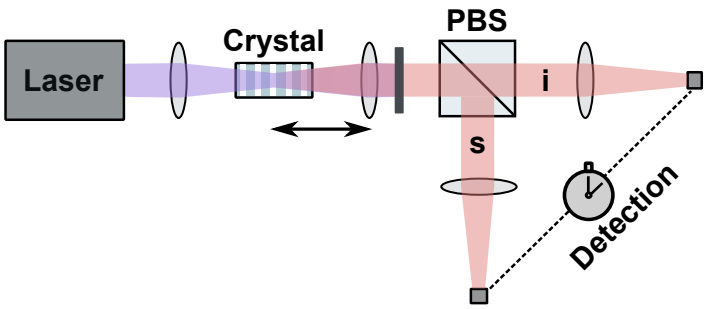

Figure 3.1: An experimental scheme that shows the time delay effect which is the subject of this section. A cw pump laser is focused into a crystal designed for type-II noncritically phase-matched SPDC. The down-converted light is collected with a second lens, and after spectral filtering the photons from a pair are split according to their polarisation with a polarising beam splitter (PBS). Finally, they are focused to detection apparatus, which may consist of SMFs followed by avalanche photodiodes (APDs), or of free-space APDs. The relative arrival time between signal and idler photons is measured as a function of the distance between the nonlinear crystal and the collection lens.

is equal in every slice of the crystal. Therefore, a first guess that a change in time delays when moving the crystal might be due to the pump focus being shifted within the crystal, turns out to be incorrect.

The phenomenon is relatively robust in the sense that it occurs for a number of different detection schemes; specifically, it was tested for single-mode fibre (SMF) detection, and for detection by free-space avalanche photodiodes (APDs) with and without the use of a narrow bandpass frequency filter. In the following pages, I will lay out the mathematical framework that allows a description of the time delay distributions for an experimentally realistic SPDC process. We will then study a simplified model which elucidates the underlying mechanism. Returning to the full model, numerical results for experimentally relevant measurements will be presented, along with corresponding experimental results that show a good agreement between the experiment and theory. The experiments were carried out by my colleague Alexander Büse, and the experimental details can be found in [2].

The aim now is to construct a complete theoretical model of the frequency and momentum correlations of the biphoton wavefunction and their effect in relevant experimental conditions. We therefore set out to calculate the number of coincidence counts as a function of time delay between signal and idler photons from type-II down-conversion, arriving at the detector for two different detection schemes: SMF collection and free space detection. Since we regard the pump focal position and distance between crystal and collection lens as free parameters, they are to appear explicitly in the calculation.

Let us begin with the biphoton wavefunction at the crystal exit facet, which already contains the dependence on the pump focal position. Throughout this work, I will model a narrowband cw pump by assuming a monochromatic pump beam, which means that signal and idler frequencies add up to a fixed pump frequency. The biphoton wavefunction is

$$|\Psi\rangle = \int \mathrm{d}\mathbf{q}_s \mathrm{d}\mathbf{q}_i \mathrm{d}\omega_s \; \Phi_{\text{full}}(\mathbf{q}_s, \mathbf{q}_i, \omega_s, \omega_i; T) \hat{a}_s^\dagger(\mathbf{q}_s, \omega_s) \hat{a}_i^\dagger(\mathbf{q}_i, \omega_i)|0\rangle, \tag{3.1}$$

where s and i label signal and idler photons, $\mathbf{q}$ is the transverse wavevector, ω the angular frequency, and T the crystal temperature. $\hat{a}_m^\dagger(\mathbf{q}, \omega)$ is the photon creation operator for a photon mode that has the polarisation as specified by m being either signal or idler, and is additionally characterised by the transverse wavenumber and frequency. The label signal is used for the photon of the down-converted pair that has the smaller group velocity inside the crystal. The integrals are implied to be over all possible values of the integration variables, unless specified otherwise. $\Phi_{\text{full}}(\mathbf{q}_s, \mathbf{q}_i, \omega_s, \omega_i; T)$ is the biphoton mode function, which takes on the form[3]

$$\begin{aligned} \Phi_{\text{full}}(\mathbf{q}_s, \mathbf{q}_i, \omega_s, \omega_i; T) \;\propto\; & \operatorname{sinc}\left(\frac{\Delta k_z(\mathbf{q}_s, \mathbf{q}_i, \omega_s, \omega_i; T) L}{2}\right) \exp\left(-\frac{w_p^2 |\mathbf{q}_s + \mathbf{q}_i|^2}{4}\right) \\ & \times \exp(i \; k_{zp}(\mathbf{q}_s + \mathbf{q}_i, \omega_s + \omega_i, T)(z_c - z_{foc}(z_c))) \\ & \times \exp(i \; (k_{zs}(\mathbf{q}_s, \omega_s, T) + k_{zi}(\mathbf{q}_i, \omega_i, T)) \; L/2). \end{aligned} \tag{3.2}$$

Here L is the crystal length, w_p the pump beam waist, k_{zm} the longitudinal component of the wavevector of photon m, Δk_z the longitudinal wave vector mismatch $k_{zp} - k_{zs} - k_{zi} - \frac{2\pi}{\Lambda}$, and Λ the poling period of the crystal (which can be set to infinity if the crystal has no periodic poling). ω_i is not an independent variable as it is given by $\omega_i = \omega_p - \omega_s$, but it is kept in the expressions for the sake of clarity. Since one of the ways to bring about the time delay effect is by longitudinally displacing the crystal, the model should allow for different crystal positions. As a part of that, we need to consider the influence the crystal position has on the pump focal position. The geometry is illustrated in Fig. 3.2. z_c denotes the position of the crystal centre and $z_{foc}(z_c)$ the focus of the pump beam, both relative to the position at which the focus coincides with the crystal centre (i.e. $z_{foc} = 0$ when $z_c = 0$). Clearly, in the commonly assumed case of the pump focal point lying at the centre of the crystal, the $\exp(i \; k_{zp}(z_c - z_{foc}(z_c)))$ term disappears. Assuming the pump beam is paraxial, its focal position in the laboratory frame is given by:

[3] A derivation of the mode function is provided in [80], which can be further simplified for a collinear configuration. The pump angular spectrum to be used takes into account the longitudinal position of the pump focus.

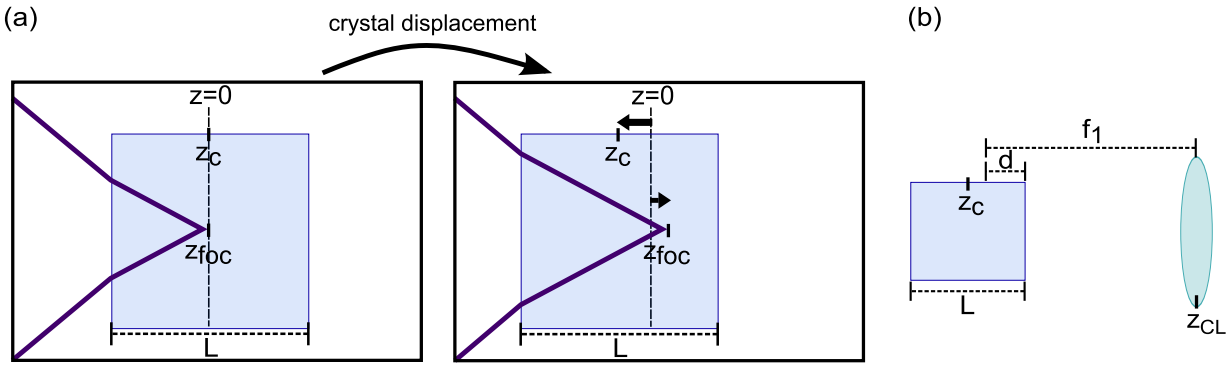

Figure 3.2: (a) Longitudinal shift of the pump focus caused by a translation of the crystal. $z = 0$ is the reference position at which the pump focus coincides with the crystal centre. z_c is the position of the crystal centre and z_{foc} the position of the pump focus. L is the length of the crystal. This configuration is similar to the one used in [81]. (b) Illustration of the geometry after the crystal. z_{CL} is the position of the collection lens which has a focal length f_1. d is the distance between a point one focal distance before the collection lens, and the crystal end.

$$z_{foc}(z_c) = \begin{cases} \frac{L}{2} - \frac{L}{2n_p} & : z_c \leq -\frac{L}{2n_p} \\ z_c - n_p z_c & : -\frac{L}{2n_p} < z_c < \frac{L}{2n_p} \\ -\frac{L}{2} + \frac{L}{2n_p} & : z_c \geq \frac{L}{2n_p}, \end{cases} \tag{3.3}$$

where n_p is the refractive index of the crystal experienced by the pump beam. The crystal positions $|z_c| = \frac{L}{2n_p}$ correspond to the pump focus lying at one of the crystal facets. Within the crystal, the pump focal position shifts in the opposite direction to the crystal movement. Once shifted out of the crystal in either direction, it no longer depends on the crystal position. From here there are two possible treatments of the spatial DOF, depending on the detection scheme used.

For SMF detection, a projection into a Gaussian detection mode is performed. This can be done at the crystal end facet where we have the expression for the biphoton wavefunction given by Eqs. (3.1), (3.2). The Gaussian detection mode is

$$G(\mathbf{q})_{z=z_c+L/2} = \frac{w_f}{\sqrt{2\pi}} \exp\left(-\frac{w_f^2|\mathbf{q}|^2}{4}\right) \exp\left(-i\frac{|\mathbf{q}|^2 d}{2k_{air}(\omega)}\right), \tag{3.4}$$

where w_f is the detection mode beam waist, and $k_{air}(\omega) = \frac{\omega}{c}$ is the wavenumber of the detected photon in air, c being the speed of light in vacuum. The Gaussian mode is effectively characterised by two parameters: the beam waist, w_f, and the distance of the crystal end from where the detection focal point would be in the absence of the crystal, $d = \left(f_1 - (z_{CL} - z_c - \frac{L}{2})\right)$. Here f_1 and z_{CL} represent the focal length and position of the

collection lens, respectively. The optimal detection beam waist depends on the pump beam waist among other things, and a body of work on this subject is available in the literature [82–84]. Usually, the detection focal point is assumed to lie at the centre of the crystal, coinciding with the pump focal point, and this imposes a particular distance from the crystal end to where the detection focal point would be without the crystal, $\left(\frac{L/2}{n}\right)$ (n is an approximation of the refractive indices of signal and idler photons, taken to be the same). The position of the collection lens for this case is $z_{CL} = \frac{L}{2} - \frac{L/2}{n} + f_1$. Additionally to the crystal position z_c, z_{CL} will also remain a parameter in these calculations to allow for longitudinal translations of the collecting lens. After projection of the photons into Gaussian detection modes with equal detection beam waists for signal and idler, the wavefunction reads:

$$\begin{aligned} |\Psi_{SMF}\rangle &= \int \mathrm{d}\omega_s \; \Phi(\omega_s, \omega_i; T)\hat{a}_s^\dagger(\omega_s)\hat{a}_i^\dagger(\omega_i)|0\rangle, \\ \Phi(\omega_s, \omega_i; T) &= \int \mathrm{d}\mathbf{q}_s \mathrm{d}\mathbf{q}_i \Phi_{\text{full}}(\mathbf{q}_s, \mathbf{q}_i, \omega_s, \omega_i; T) G^*(\mathbf{q}_s) G^*(\mathbf{q}_i). \end{aligned} \tag{3.5}$$

In order to calculate the time delay distribution between the arrival times of signal and idler photons, the following expression is evaluated:

$$R_{coinc,SMF}(\tau) \propto |\langle 0|\hat{E}_i^{(+)}(t-\tau/2)\hat{E}_s^{(+)}(t+\tau/2)|\Psi_{SMF}\rangle|^2, \tag{3.6}$$

where the operator $\hat{E}_m^{(+)}(t)$ is proportional to $\int \mathrm{d}\omega \, \exp(-i\omega t)\hat{a}_m(\omega)$. The reason t does not appear on the left-hand-side is that for a monochromatic pump beam, the quantity is independent of the mean time; it only depends on the time difference.

In contrast to the SMF case where only one spatial mode is relevant at the detector, for free-space detection, the counts as a function of time delay need to be calculated for all pairs of points on the detector surfaces, and subsequently integrated over all such available pairs:

$$\begin{aligned} R_{coinc,FS}(\tau) &= \int_{\mathrm{A_{det}}} \mathrm{d}\mathbf{r}_s \mathrm{d}\mathbf{r}_i R_{coinc,PP}(\mathbf{r}_s, \mathbf{r}_i, \tau) \\ &\propto \int_{\mathrm{A_{det}}} \mathrm{d}\mathbf{r}_s \mathrm{d}\mathbf{r}_i |\langle 0|\hat{E}_i^{(+)}(\mathbf{r}_i, t-\tau/2)\hat{E}_s^{(+)}(\mathbf{r}_s, t+\tau/2)|\Psi\rangle|^2 \end{aligned} \tag{3.7}$$

The electric field operator at the detector plane can be related to the annihilation operator at the crystal exit facet using a thin lens model from Fourier optics and the Fresnel

approximation:

$$\begin{aligned}\hat{E}^{(+)}(\mathbf{r},t)_{z=z_{det}} &= \int \mathrm{d}\omega\ \mathrm{d}\mathbf{q}\ \exp\left(-i\frac{f_1}{f_2}\mathbf{r}\cdot\mathbf{q}-i\omega t\right)\\ &\quad\times\exp\left(-ik_{air,z}d\right)\hat{a}(\mathbf{q},\omega)_{z=z_c+L/2}\\ &\approx \int \mathrm{d}\omega\ \mathrm{d}\mathbf{q}\ \exp\left(-i\frac{f_1}{f_2}\mathbf{r}\cdot\mathbf{q}-i\omega t\right)\\ &\quad\times\ \exp\left(i\left(-k_{air}(\omega)+\frac{|\mathbf{q}|^2}{2k_{air}(\omega)}\right)d\right)\hat{a}(\mathbf{q},\omega)_{z=z_c+L/2}, \end{aligned}\tag{3.8}$$

where f_1 and f_2 are the focal lengths of the collection lens and of the focusing lenses in front of the detectors, respectively. For each pair of points that contribute to the integral in Eq. (3.7) and for the expression from the Gaussian detection scheme (3.6), the coincidence counts as a function of time delay can be cast in the form of

$$\begin{aligned}R_{coinc}(\tau) \ \propto\ &\Bigg|\int \mathrm{d}\mathbf{q}_s\mathrm{d}\mathbf{q}_i\mathrm{d}\Omega\ \exp\left(i(k_{zs}(\mathbf{q}_s,-\Omega,T)+k_{zi}(\mathbf{q}_i,\Omega,T))\ L/2\right)\\ &\times\exp\left(id\left(\frac{|\mathbf{q}_s|^2}{2k_{air}(-\Omega)}+\frac{|\mathbf{q}_i|^2}{2k_{air}(\Omega)}\right)\right)\\ &\times\mathrm{sinc}\left(\Delta k_z\frac{L}{2}\right)g(\mathbf{q}_s,\mathbf{q}_i,z_c)\ \exp(i\Omega\tau)\ \Bigg|^2. \end{aligned}\tag{3.9}$$

Ω is defined as $\Omega \equiv \omega_i - \omega_p/2$, and the shorthand of Ω as an argument of wavenumbers implies an evaluation at $\frac{\omega_p}{2}+\Omega$. $g(\mathbf{q}_s,\mathbf{q}_i,z_c)$ incorporates the remaining terms and depends on the type of detection and on the crystal position through the pump focal position. The term that models a change in the distance between crystal and collection lens is $\exp\left(id\left(\frac{|\mathbf{q}_s|^2}{2k_{air}(-\Omega)}+\frac{|\mathbf{q}_i|^2}{2k_{air}(\Omega)}\right)\right)$. What impact does such a transverse momentum-dependent phase have on the time delay? A potential impact must be mediated by spatio-temporal correlations. Hence, a way to develop an understanding is by considering the form of spatio-temporal correlations imposed by the phase-matching conditions of SPDC.

To gain an intuitive picture of the system, in the following I develop a toy model by introducing approximations. I will, however, return to the full Eqs. (3.6) and (3.7) for the simulation. To learn about the spatio-temporal correlations, it is instructive to perform a multivariate Taylor approximation of k_{zs}, k_{zi} and Δk_z, about the collinear degenerate case up to leading order terms [4]. The reference, for which we take $k_{zp}-k_{zs}-k_{zi}-\frac{2\pi}{\Lambda}=0$, is therefore at $\Omega=0,\ T=T_0,\ \mathbf{q}_s=\mathbf{q}_i=\mathbf{0}$. For now, let us further simplify the analysis by considering the case of a plane wave pump beam with $\mathbf{q}_p=\mathbf{0}$ for the toy model. This

[4] Details can be found in Appendix C.3

imposes $-\mathbf{q}_s = \mathbf{q}_i \equiv \mathbf{q}$, and hence $|\mathbf{q}_s|^2 = |\mathbf{q}_i|^2 = |\mathbf{q}|^2$ which will allow us to immediately draw some interesting conclusions:

$$\Delta k_z \approx \Omega D + (T - T_0)E + \frac{|\mathbf{q}|^2}{2k_s(0)} + \frac{|\mathbf{q}|^2}{2k_i(0)}, \tag{3.10}$$

where $D = \left(\frac{\partial k_s}{\partial \Omega} - \frac{\partial k_i}{\partial \Omega}\right)$ and $E = \left(\frac{\partial k_p}{\partial T} - \frac{\partial k_s}{\partial T} - \frac{\partial k_i}{\partial T} + \frac{2\pi}{(\Lambda(T_0))^2}\frac{\partial \Lambda}{\partial T}\right)$. From now on, all derivatives are evaluated at the reference settings mentioned above. With very long crystals and a plane wave pump beam, the photons would be generated only in the perfect phase matching condition, $\Delta k_z = 0$. One can see that this case entails a linear dependence between Ω and $|\mathbf{q}|^2$, indicated by the overlaid line in Fig. 3.3 (a) and also shown in Ref. [85]. As a result, the q-dependent phase term induced by a relative displacement between the crystal and collection lens, causes a shift of the time delays which is proportional to the change in distance between the two. This mechanism can cause a crystal position-dependent time delay of the emitted photons. It is interesting to note that the absence of a linear term in momentum in Eq. (3.10) is due to the fact that in the configuration under investigation, the photons propagate along one of the optical axes; in other configurations there can be a linear dependence in the momentum [86]. In the case of type-I down-conversion [87–89] a linear relationship also appears, since the spatio-temporal correlation of the case under study relies on a difference in the group velocities of signal and idler.

Let us return to the finite crystal model where the sinc function actually results in a spread of $|\mathbf{q}|^2$ values for a given Ω value. To account for this spread and deepen our first grasp of the underlying physics, let us analyse (3.9), again using the Taylor approximation of the longitudinal wavevector mismatch (3.10).

$$\begin{aligned} R_{coinc}(\tau) \propto & \left| \int \mathrm{d}\mathbf{q}\mathrm{d}\Omega \exp\left(i\frac{L}{2}\left(k_s(0) + k_i(0) + (T - T_0)\left(\frac{\partial k_s}{\partial T} + \frac{\partial k_i}{\partial T}\right) - \Omega D\right)\right)\right. \\ & \times \exp\left(id\left(\frac{|\mathbf{q}|^2}{2k_{air}(-\Omega)} + \frac{|\mathbf{q}|^2}{2k_{air}(\Omega)}\right)\right) \\ & \left. \times \mathrm{sinc}\left(\left(\Omega D + (T - T_0)\,E + \frac{|\mathbf{q}|^2}{2k_s(0)} + \frac{|\mathbf{q}|^2}{2k_i(0)}\right)\frac{L}{2}\right) g(\mathbf{q})\, \exp(i\Omega\tau)\right|^2. \end{aligned} \tag{3.11}$$

Since a plane wave pump is assumed and therefore $\mathbf{q}_s = -\mathbf{q}_i$, the integrals over signal and idler transverse momenta were replaced by an integral over one transverse momentum. Also note that the dependence of g on the crystal position, z_c, has dropped out for a plane wave pump. It is now possible to proceed with Eq. (3.11) as follows: Since the modulus is taken, the phase that is independent of the integration variables can be removed. Next, one can evaluate the integral over Ω, which is an inverse Fourier transform of a sinc function. Then,

the functions that contain no dependence on $\mathbf{q}$ can be taken outside of the remaining integral. This leaves us with

$$\begin{aligned} R_{coinc}(\tau) \;\propto\; & \left| \frac{2\pi}{DL} \mathrm{rect}\left(\frac{1}{DL}\left(\tau - D\frac{L}{2}\right)\right) \right. \\ & \times \int \mathrm{d}\mathbf{q} \exp\left(id\left(\frac{|\mathbf{q}|^2}{2k_{air}(-\Omega)} + \frac{|\mathbf{q}|^2}{2k_{air}(\Omega)}\right)\right) \\ & \left. \times \exp\left(-i\left(\tau - D\frac{L}{2}\right)\frac{1}{D}\left(\frac{|\mathbf{q}|^2}{2k_s(0)} + \frac{|\mathbf{q}|^2}{2k_i(0)}\right)\right) g(\mathbf{q}) \right|^2 . \end{aligned} \tag{3.12}$$

At this point, making the approximation of $k_s(0) \approx k_i(0) \approx nk_{air}(\Omega) \approx nk_{air}(-\Omega) \approx nk_{air}(0)$ shows the primary effect of changing the distance between crystal and collection lens:

$$\begin{aligned} R_{coinc}(\tau) \;\propto\; & \left| \frac{2\pi}{DL} \mathrm{rect}\left(\frac{1}{DL}\left(\tau - D\frac{L}{2}\right)\right) \right. \\ & \left. \times \int \mathrm{d}\mathbf{q} \exp\left(\frac{-i|\mathbf{q}|^2}{nDk_{air}(0)}(\tau - \tau_0)\right) g(\mathbf{q}) \right|^2 , \end{aligned} \tag{3.13}$$

where $\tau_0 = DL/2 + nD(f_1 - z_{\mathrm{CL}} + z_c + L/2)$. The two key outcomes we can learn from the simplified expression (3.13) are the rectangular function and the shift in τ within the integral. The rectangular function has a width of DL and is centred such that the non-zero interval begins at 0. It physically corresponds to the time delays photons can acquire throughout the length of the crystal and ensures that the time delay distribution can only be non-zero in this specific interval. As for the specific shape of the time delay distribution, this depends on $g(\mathbf{q})$, which means that it is not predicted with this general analysis. The important thing, however, is that within the applicability of the approximations made, a change in the distance between collection lens and crystal, $z_{\mathrm{CL}} - z_c$, results in a shift of the time delay distributions, except for the fixed cut-off by the rectangular function. The shift is given by $nD\Delta z$, where Δz is the displacement of the crystal or collection lens. It is important to bear in mind that this general analysis applies to the case of fibre-coupled detection and to individual pairs of points on the detectors contributing to the free-space detection.

Now that we have gained an understanding of the underlying mechanism, let us look into the implications this has on experimentally realistic settings. The numerical results from the remainder of this subsection are based on the biphoton mode function and coincidences given by (3.6) and (3.7) as evaluated numerically without the approximations made later on, with the refractive indices modeled by temperature-dependent Sellmeier equations [5]. One

[5] Details can be found in Appendix C.1

of the detection schemes incorporates a bandpass filter, which was modelled with a Gaussian spectral transmission function applied to the biphoton wavefunction. The parameters required as inputs to the simulations are the crystal length, crystal poling period, crystal temperature, pump wavelength, pump beam waist, and the detection beam waist (for SMF detection) or the magnification of the imaging system and the detection area (for free-space detection). The parameter values used for the simulations are provided in the caption of Fig. 3.4.

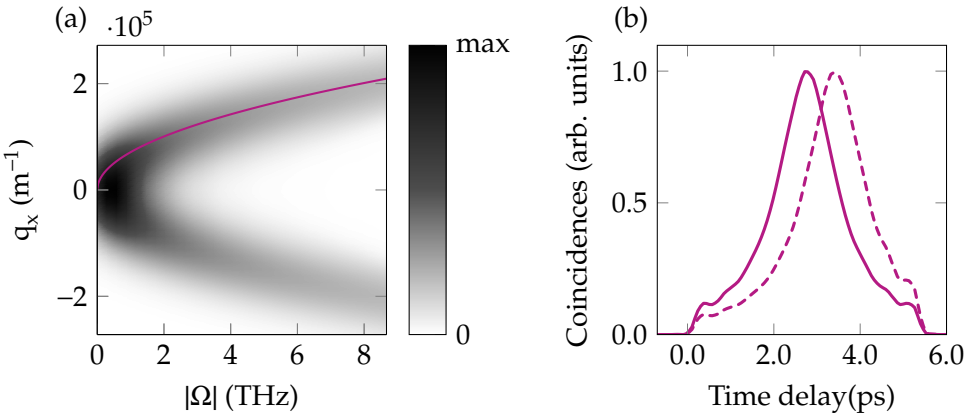

FIGURE 3.3: (a) Calculated spatio-temporal correlations of the SPDC wavefunction for experimentally relevant parameters (the parameters are as specified in the caption of Fig. 3.4 (b), but without a spectral filter). The plotted quantity is proportional to the probabilities of different q_x, Ω values for a photon with $q_y = 0$, after having traced out the other photon of the pair. The overlaid line illustrates the linear dependence between Ω and $|\mathbf{q}|^2$. (b) Simulated time delay distribution between signal and idler photons for SMF detection (corresponding to Fig. 3.4 (a)), with the crystal in the central position (solid line) and shifted by 1 mm (dashed line).

To demonstrate the applicability of the key analytic results from the toy model, which assumes a plane wave pump and is based on a Taylor approximation of the wavevector mismatch, to the experimentally more realistic case of a focused pump beam, simulation results are presented in Fig. 3.3 without the use of those approximations. Fig. 3.3 (a) shows the spatio-temporal correlations for an experimental set-up, with the linear dependence between $|\mathbf{q}|^2$ and Ω illustrated. The main outcomes from the simplified expression (3.13) can be recognised in Fig. 3.3 (b), which shows time delay distributions for two different crystal positions using the SMF detection scheme. As discussed, the time delay distribution is shifted when the crystal is displaced, except for a fixed cut-off that remains and is modelled by the rectangular function. Of course unlike for a plane wave pump, the pump focal position comes into play for a focused pump. From further simulations it was found that the focal position of the pump beam has little effect on the time delay shift, but has a significant

impact on the proportion of photons detected, particularly depending on whether the pump and detection focal positions match up.

Experimentally, a direct measurement of the actual time delay distributions such as predicted in Fig. 3.3 (b) is extremely challenging owing to the electronic jitter of the measurement apparatus, which is much larger than the time delays in question. Measuring a mean time delay is a more modest and realistic, although still nontrivial, endeavour that is detailed in [2]. Therefore, Fig. 3.4 shows mean time delays as a function of the longitudinal crystal position, for three different detection schemes: (a) With detection after incoupling into SMFs, (b) with free-space detection after a 2.5 nm wide bandpass filter, and (c) with free-space detection after a longpass filter. Across these different detection schemes, the behaviour is qualitatively the same: At the central crystal position, the mean time delay corresponds to the delay acquired between signal and idler photons based on their group velocity mismatch and a propagation through half of the crystal length. In some region around the central crystal position, the mean time delay is monotonic with the crystal position. As the crystal is displaced even further, a turning point is traversed and the mean time delays once again approach the one corresponding to propagation through half of the crystal length.

The behaviour of the mean time delays as a function of crystal position can be understood by considering what happens to the full time delay distribution. The exact shape of the

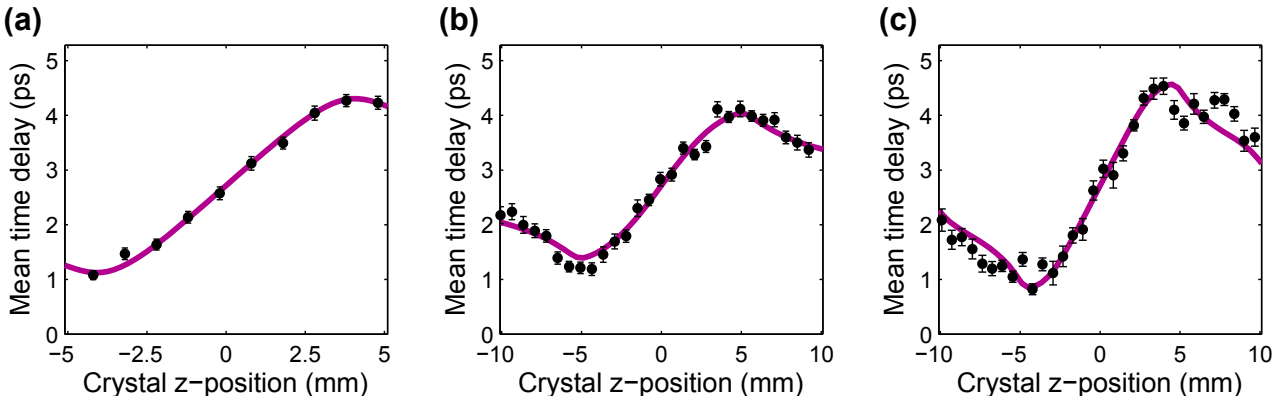

Figure 3.4: Mean time delay between signal and idler as a function of the crystal z-position for different detection schemes. (a) With detection after incoupling into SMFs, (b) with free-space detection after a 2.5 nm wide bandpass filter centred at 808 nm, and (c) with free-space detection after a longpass filter. The solid lines are simulation results, while the data points with error bars extending over one standard deviation are experimental results obtained by Alexander Büse. The parameters used in the simulation match the following experimental settings: a periodically poled potassium titanyl phosphate (ppKTP) crystal of 15 mm length with a poling period of 9.89 μm and a 404.25 nm pump beam. (a) $w_p = 12.9$ µm, $T = 59$ °C, $w_f = 18$ µm, (b) $w_p = 11.4$ µm, $T = 58$°C, $l = 40$ µm, $\frac{f_1}{f_2} = \frac{5}{3}$, (c) $w_p = 11.4$ µm, $T = 60$°C, $l = 40$ µm, $\frac{f_1}{f_2} = \frac{5}{3}$. l denotes the side length of the quadratic free-space detection area.

time distributions and mean time delay curves is jointly determined by the details of the nonlinear crystal (material, length, poling period, temperature), as well as the pump and detection modes and wavelengths. The central crystal position produces a symmetric time delay distribution, an example of which is depicted as the solid line of Fig. 3.3 (b). With a displacement of the crystal, this distribution is shifted (see dashed line). However, parts of the distribution are lost as they would be shifted outside the non-zero region, corresponding to 0 and the maximum time delays. When the bulk of the original peak is lost and only some pedestal remains, the mean time delay returns back towards the value corresponding to the central crystal position. At the same time, coincidence counts are lost, which is demonstrated for the case of free-space detection with a bandpass spectral filter in Fig. 3.5. An important but not immediately obvious fact is that even in the optimal case of central crystal position, only a portion of the down-converted photons is detected. This corresponds to the maximum in Fig. 3.5. For the case of SMF coupling, this is unsurprising since the detection is governed by the overlap between the Gaussian detection mode and the spatial mode of the SPDC photons, which are not in a purely Gaussian mode. However, losses also exist for free-space detection as simulated here, due to the SPDC beam exceeding the detector area. Although spatio-temporal correlations have been identified as the underlying mechanism, imperfect detection is in fact also required to create the overall effect of the changing time delays.

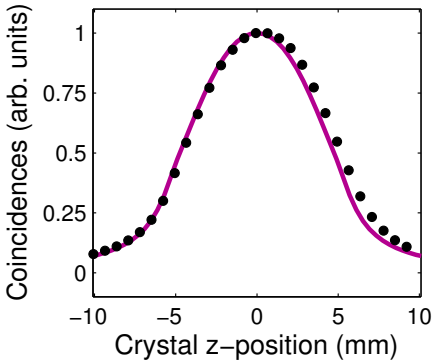

Figure 3.5: Drop of the coincidence count rate with longitudinal displacement of the crystal. The simulation (solid line) is for the free-space detection scheme with the 2.5 nm wide bandpass filter, i.e. the case belonging to Fig. 3.4 (b). The experimental values were measured by Alexander Büse.

A very similar behaviour was obtained when longitudinally displacing the collimating lens behind the nonlinear crystal instead of displacing the crystal. This can be attributed to the same mechanism, because the factor responsible for the effect in Eq. (3.9) is $d = \left(f_1 - (z_{CL} - z_c - \frac{L}{2})\right)$, which directly contains the distance between crystal and collection

lens. However, a displacement of the nonlinear crystal is experimentally more meaningful, in the sense that on the one hand, a misalignment is more likely to occur unintentionally and on the other hand, if one wanted to deliberately produce the effect, it would also be the better choice. The reason is that the drop in coincidence counts with a movement of the crystal is smaller than with a movement of the collimating lens.

This subsection has studied the effect that imparting a quadratic phase as a function of the signal and idler transverse momenta has on the time delays. As future work, this specific example of manipulating the temporal DOF through the spatial one could be extended to more general schemes. The spatio-temporal correlations offer the prospect of shaping the spectral wavefunction through more complex spatial manipulations. Arbitrary spatial phase and amplitude distributions could be imparted using components such as spatial light modulators (SLMs), holograms, and q-plates. This could result in a scheme with a similar operational principle to that of typical pulse shapers, which employ a grating to separate frequencies, an SLM or similar to imprint the desired function on the photons, and a second grating to subsequently recombine the frequencies [90]. However, since spatio-temporal correlations manifest themselves as specific frequencies corresponding to particular spatial modes, the need for the separation of frequencies via prisms could be circumvented. A step towards such a scheme is also demonstrated in the next subsection.

3.3 Measurement of spectral biphoton wavefunctions through quantum interference

Now that we have looked at ways to influence the spectrotemporal properties of biphotons, the next question arising is how these properties can be experimentally measured. Several approaches to reconstructing the full complex spectral wavefunction are possible, each associated with some experimental challenges. Interferometric methods require a high level of stability [91–93]. Other methods widely used for determining the complex spectra of bright coherent sources rely on nonlinear optical effects [94]. Yet, such effects are inherently inefficient at the low intensity levels typical of quantum light sources. Technological and material advances have recently bridged the gap and enabled the use of sum-frequency generation (SFG) for measuring time delay distributions of photon pairs [72, 73, 95]. However, they usually require large nonlinearities or high powers to be effective.

Hong, Ou, and Mandel set out to measure the time delay between two photons in a pair, back when the inefficiencies of SFG were prohibitive. This prompted them to come up with an alternative strategy to measure the coherence length and time delay between two photons,

circumventing the need for optical nonlinearities. It resulted in the 1987 experiment that now carries their name and is one of the most prominent examples of quantum interference [15]. As we will see later on, the usual HOM dip does not allow to reconstruct the full wavefunction. However, the interference phenomenon has since then proven useful in a variety of applications, including quantum teleportation [96], quantum gates [97, 98], linear optics quantum computation [99], Bell-state analysers [100], and the measurement of the group velocity of light [101], as well as of dispersion [102].

Extensions of the HOM approach also enable the full reconstruction of complex spectral wavefunctions. Chen and co-workers [103] rely on the time resolution of the detectors to directly measure time delay distributions, and therefore their method is applicable to very narrow-band biphotons. In contrast, Douce *et al.* [104] propose a scheme to measure the biphoton Wigner function using HOM interference by adding shifts of the biphoton frequencies. Yet, a direct practical implementation of such shifts is not particularly simple or efficient [105]. This subsection presents a variation of the scheme in Ref. [104], that relies on the ability to effectively shift the relative frequency of the biphoton state in the generation process. It allows the measurement of the complex spectral wavefunction for type-II SPDC with a monochromatic pump in an arbitrary paraxial spatial mode, after projection of the down-converted photons into a likewise arbitrary paraxial spatial mode. In this subsection I demonstrate the method for the particular configuration of collinear down-conversion using a periodically poled crystal, i.e. the same SPDC scheme as in the previous subsection. Experiments implementing the method, and thereby successfully reconstructing complex spectral wavefunctions, were performed by my colleague Alexander Büse and are further detailed in Ref. [3]. Other type-II SPDC configurations will also be discussed. Different systems, such as four-wave mixing in atomic species, can be similarly controlled by tuning the frequencies of the pumps [103]. The assumption of a monochromatic pump beam means that the frequencies of signal and idler photons are perfectly anticorrelated, hence reducing the problem to the determination of a complex-valued function of one variable. We will concentrate on the case of a monochromatic pump, but will also address the question of a pulsed pump later on.

The experiment is an extension of a conventional HOM type set-up by tuning either the temperature of the nonlinear crystal or the pump frequency, so that a quantum interference coincidence pattern is recorded as a function of path length difference and crystal temperature or pump frequency. An example of such a pattern for a particular set of spatial modes can be found in Ref. [106]. We will see that this type of a multivariable quantum interference pattern can in fact be used to reconstruct the complex spectral mode function $\Phi(\Omega)$, which determines the wavefunction $|\Psi\rangle = \int \mathrm{d}\Omega\ \Phi(\Omega)\hat{a}_s^\dagger\left(\frac{\omega_p}{2}+\Omega\right)\hat{a}_i^\dagger\left(\frac{\omega_p}{2}-\Omega\right)|0\rangle$. Here $\hat{a}_m^\dagger(\omega)$ is

the creation operator for a photon with frequency ω and polarisation as indicated by the subscript, and ω_p is the pump frequency.

Section 3.2 has already shown that the spectral wavefunction can be influenced through the spatial DOF. Continuing with this idea, an influence of the spatial detection modes on the wavefunction will be used to create different test cases. This leads to nontrivial complex spectra with marked differences to the standard sinc function [106], making their characterisation worthwhile. The ability to shape the spectral wavefunction is important for quantum information and communication applications, and has already been pursued for single photons and photon pairs using other approaches [95, 107]. A way of narrowing the spectrum of bright squeezed vacuum has also been introduced and demonstrated in Ref. [108].

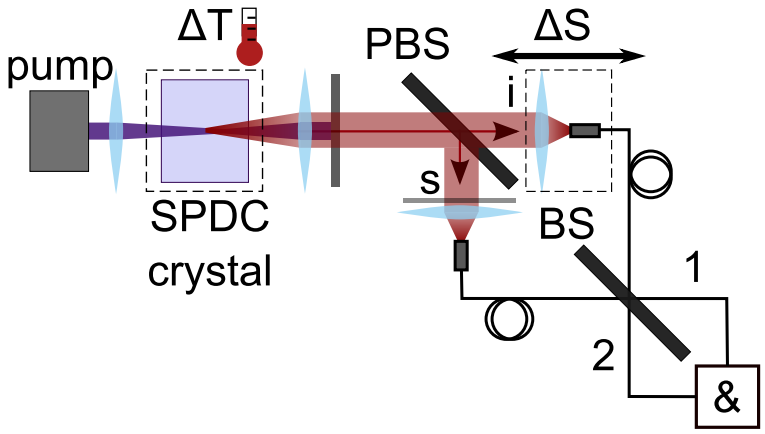

Figure 3.6: Proposed experimental set-up: A monochromatic pump beam is focused into the temperature-controlled nonlinear crystal in which the collinear type-II SPDC process takes place. The down-converted light is collimated by a lens after the crystal. The pump beam is discarded by a longpass filter. The photon pairs (s and i denoting signal and idler, respectively) are separated by a polarising beam splitter (PBS). A set of waveplates (shown as the grey line in the signal path) is used to maximise interference. The path length in air between the signal and idler arms differs by a controllable amount ΔS, before coupling into SMFs. Finally, the photons pass through a fibre beam splitter (BS), and coincidences (&) are detected across two APDs, one for each fibre beam splitter output arm. Alternatively, it is also possible to implement a free space HOM experiment, with the SMF coupling at the end. For the use of higher order Laguerre Gaussian detection modes, holograms can be inserted in the paths before SMF coupling.

The experimental set-up that is proposed here for measuring the spectral wavefunction and that is modelled in the simulations, is shown in Fig. 3.6. It consists of a HOM experiment using photons which are created in collinear, type-II down-conversion using a monochromatic Gaussian pump beam focused in the nonlinear crystal, and are separated by a polarising beam splitter. The special feature of the experiment is a tuning of the crystal temperature,

or alternatively of the pump wavelength, in addition to the usual sweep of path length differences. To create different test cases, the usual Gaussian detection mode is modified, by projecting the down-converted photons into a Laguerre-Gaussian mode, or by displacing the nonlinear crystal along the beam's propagation axis.

The data acquisition consists in measuring the coincidence count rate as a joint function of path length difference and either the crystal temperature or pump frequency. The simulation results are presented for a tuned crystal temperature, but the written expressions account for both possibilities. Tuning of the crystal temperature is known to influence the biphoton wavefunction through the temperature dependence of the crystal's dielectric tensor and if the crystal is periodically poled, additionally through thermal expansion leading to a change in its poling period.

The normalised coincidence count rates can be modelled as

$$R_{\text{coinc}}(\Delta S, T, \omega_p) = t^4 + r^4 - 2r^2t^2\text{Re}\left[f\left(\Delta S, T, \omega_p\right)\right], \tag{3.14}$$

where $\Delta S \equiv (S_s - S_i)$ is the difference between signal and idler path lengths, T is the crystal temperature, ω_p the pump frequency, and t and r are the moduli of the transmission and reflection amplitudes of the HOM beam splitter, respectively. In addition, I have defined

$$\begin{aligned} f\left(\Delta S, T, \omega_p\right) \quad \equiv \quad & \int \mathrm{d}\Omega \Phi\left(\Omega; T, \omega_p\right) \Phi^*\left(-\Omega; T, \omega_p\right) \\ & \times \exp\left(i\Delta S 2\Omega/\mathrm{c}\right), \end{aligned} \tag{3.15}$$

where c is the speed of light in vacuum. The conventional HOM dip is a slice of such a surface $R_{\text{coinc}}(\Delta S, T, \omega_p)$ along the ΔS direction, keeping the crystal temperature and pump frequency fixed. The coincidence counts thus involve our complex wavefunction of interest,

$$\begin{aligned} \Phi\left(\Omega; T, \omega_p\right) \quad \equiv \quad & \int\int \mathrm{d}\mathbf{q}_s \mathrm{d}\mathbf{q}_i \; \Phi_{\text{full}}(\mathbf{q}_s, \mathbf{q}_i, \Omega; T, \omega_p) \\ & \times G_{\mathrm{s}}^*(\mathbf{q}_s) G_{\mathrm{i}}^*(\mathbf{q}_i), \end{aligned} \tag{3.16}$$

where $\Phi_{\text{full}}(\mathbf{q}_s, \mathbf{q}_i, \Omega; T, \omega_p)$ is the wavefunction before projection into the spatial modes $G_{\mathrm{s}}(\mathbf{q}_s)$ and $G_{\mathrm{i}}(\mathbf{q}_i)$, with $\mathbf{q}$ being the transverse momenta [6]. However, due to the nature of quantum interference, the wavefunction appears in the form of

$$F(\Omega, T, \omega_p) \equiv \Phi\left(\Omega; T, \omega_p\right) \Phi^*\left(-\Omega; T, \omega_p\right), \tag{3.17}$$

[6] Details can be found in Appendix C.2

which will be referred to as the *symmetrised* wavefunction. Since $F(\Omega, T, \omega_p)$ is Hermitian with respect to Ω, $f\left(\Delta S, T, \omega_p\right)$ is real and from the coincidence rates (recall Eq. (3.14)):

$$f\left(\Delta S, T, \omega_p\right) = \left(\frac{1}{2r^2t^2}\left(t^4 + r^4 - R_{\text{coinc}}(\Delta S, T, \omega_p)\right)\right). \tag{3.18}$$

We then obtain $F(\Omega, T, \omega_p)$ by taking the Fourier transform of $f\left(\Delta S, T, \omega_p\right)$ with respect to ΔS:

$$F(\Omega, T, \omega_p) = \frac{1}{c\pi}\int \mathrm{d}\Delta S f\left(\Delta S, T, \omega_p\right) \exp(-i(2\Omega)\Delta S/c). \tag{3.19}$$

Because the symmetrisation is not isomorphic, Eq. (3.17) can in general not be inverted to retrieve the wavefunction from the usual HOM dip, so additional information is required. One possibility is to extend the measurements by shifting the relative frequencies of signal and idler. The reconstruction is also possible by performing a temperature or a pump frequency sweep. To see this, let us perform a multivariate Taylor expansion to leading orders of the wavevector z-components for each of pump, signal, and idler (indicated by subscript m), about the values at which perfect phase matching takes place: at frequencies $\omega_m = \omega_{0m}$, crystal temperature $T = T_0$, and transverse wavevector $\mathbf{q}_m = \mathbf{0}$. From the Taylor series approximation, symmetrised wavefunctions at different temperatures can be related by shifting the frequencies, while keeping the temperature fixed [7]:

$$\begin{aligned}
\Phi \quad & \left(\Omega; T_0 + \Delta T, \omega_{0p} + \Delta\omega_p\right) \Phi^*\left(-\Omega; T_0 + \Delta T, \omega_{0p} + \Delta\omega_p\right) \\
\approx \quad & \Phi\left(\Omega + \Delta T c_t + \Delta\omega_p c_{\omega p}; T_0, \omega_{0p}\right) \\
& \times\Phi^*\left(-\Omega + \Delta T c_t + \Delta\omega_p c_{\omega p}; T_0, \omega_{0p}\right),
\end{aligned} \tag{3.20}$$

where the following definitions have been used:

$$c_t \equiv -\frac{X_T}{\left(\frac{\partial k_s}{\partial\omega} - \frac{\partial k_i}{\partial\omega}\right)}, \tag{3.21}$$

$$X_T \equiv \left(\frac{\partial k_p}{\partial T} - \frac{\partial k_s}{\partial T} - \frac{\partial k_i}{\partial T} + \frac{2\pi}{\left(\Lambda\left(T_0\right)\right)^2}\frac{\partial\Lambda}{\partial T}\right), \tag{3.22}$$

$$c_{\omega p} \equiv -\frac{X_\omega}{\left(\frac{\partial k_s}{\partial\omega} - \frac{\partial k_i}{\partial\omega}\right)}, \tag{3.23}$$

$$X_\omega \equiv \left(\frac{\partial k_p}{\partial\omega} - \frac{\partial k_s}{2\partial\omega} - \frac{\partial k_i}{2\partial\omega}\right). \tag{3.24}$$

Here, k_m are the wavenumbers in the crystal (pump, signal, and idler indicated by subscripts),

[7] Details can be found in Appendices C.3 and C.4

ω_m the frequencies, and Λ the poling period of the crystal. The $\frac{\partial k_m}{\partial \omega}$ are inverse group velocities. All derivatives are evaluated at the reference temperature T_0 and frequencies $\omega_m = \omega_{0m}$, $m \in \{p, s, i\}$. c_t and $c_{\omega p}$ can be identified as proportionality constants between a shift in T or ω_p, and Ω. They represent the measurable sensitivity of the biphoton spectrum to the crystal temperature and pump wavelength. The complex mode function can be obtained as a slice through $F(\Omega, \Delta T, \Delta\omega_p)$:

$$\Phi(2c_t\Delta T + 2c_{\omega p}\Delta\omega_p; T_0, \omega_{0p}) = \frac{F^*(-c_t\Delta T - c_{\omega p}\Delta\omega_p, T_0 + \Delta T, \omega_{0p} + \Delta\omega_p)}{\sqrt{|F(0, T_0, \omega_{0p})|}}. \tag{3.25}$$

As previously mentioned, either crystal temperature or pump frequency may be swept in the experiment. However, it is sufficient to scan one, while keeping the other variable fixed. The whole data analysis is illustrated in the schematic of Fig. 3.7.

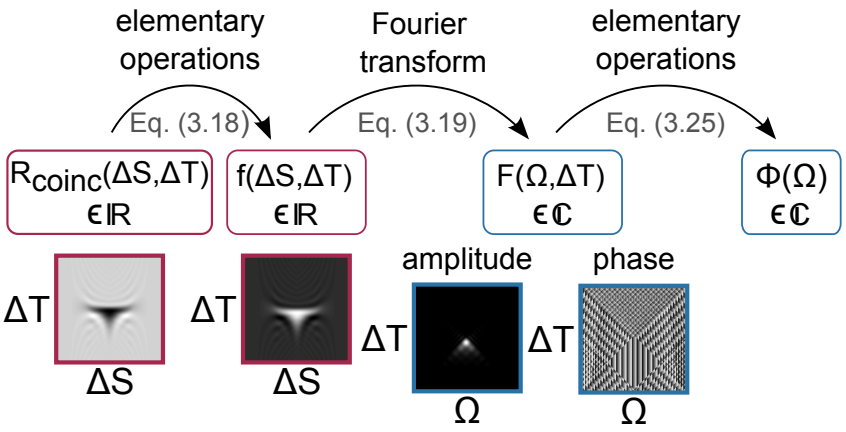

FIGURE 3.7: Steps to determine $\Phi(\Omega)$ from $R_{\text{coinc}}(\Delta S, \Delta T)$. Starting with R_{coinc}, the real coincidence counts, elementary operations are performed to arrive at another real function f (Eq. (3.18)). Taking a Fourier transform of f with respect to ΔS leads to the complex function F (by Eq. (3.19)). The desired wavefunction is obtained by taking an appropriate slice of F (by Eq. (3.25)). The essence of the method is the fact that for the symmetrised mode function, which occurs in the quantum interference coincidence counts, a change in temperature is approximately equivalent to a shift in frequency.

The use of the reconstruction method is demonstrated on three test cases, shown in Fig. 3.8. The test cases all use a Gaussian pump beam with a beam waist of 4.3 μm, but differ in the detection modes. These are, each with a beam waist of 9.6 μm, (a) Gaussians with the crystal centred, (b) Gaussians with the crystal displaced by 3 mm along the propagation direction, and (c) the Laguerre Gaussian modes (azimuthal index, radial index) = (1,0), (-1,0) with the crystal centred.

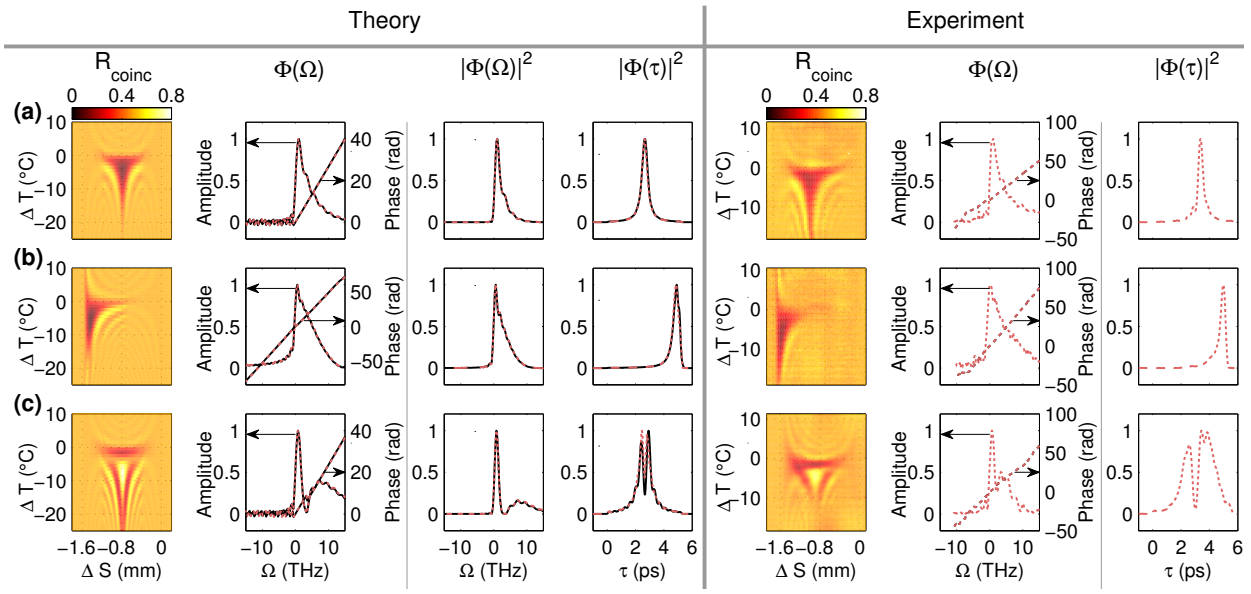

Figure 3.8: Demonstration of the reconstruction method on three test cases, obtained through the use of different projection modes. Theoretical results are in the left panel, while the corresponding experimental results, obtained by Alexander Büse, are shown on the right. For the simulations, a pump beam with a wavelength of 404.25 nm and a beam waist in the crystal $w_p = 4.3$ μm is used. The crystal is a 15 mm long ppKTP crystal with a poling period $\Lambda(T_0) = 9.89$ μm at the collinear degenerate crystal temperature $T_0 = 58°$C. The parameter c_t for an expansion about degenerate SPDC is $-4.8698 \times 10^{11}\,(°\mathrm{C}\cdot s)^{-1}$. The detection beam waist is $w_s = w_i = 9.6$ μm in all cases. The detection modes are (a) Gaussians with the crystal centred, (b) Gaussians with the crystal displaced by 3 mm along the propagation direction, and (c) a pair of Laguerre Gaussian modes (1 0), (-1 0) with the crystal centred. The plots show (from left to right) the coincidence counts, the complex spectral wavefunctions (amplitude in arb. units), the spectral distributions (arb. units), and the time delay distributions (arb. units). For experiments, the spectral distribution is omitted. The red dotted lines are the reconstruction results, while the black solid lines within the theory section are based on the simulated wavefunction.

The left panel contains the theory results, while the right panel shows experimental results. The experiment was performed by Alexander Büse and is discussed in more detail in [3], but a good agreement between theory and experiment can be noted. The theory results were obtained in the following way: From a model of the nonlinear process and detection, the spectral wavefunction was obtained directly (black solid line). Then, the quantum interference pattern was simulated, based on which the spectral wavefunction was reconstructed using Eqs. (3.18-3.25) (red dashed line). The spectral and time delay distributions were calculated both from the original and the reconstructed wavefunction, shown in black solid and red dashed lines, respectively. This allows drawing a comparison between the reconstructed functions and the original ones.

Fig. 3.8 shows a close match of the original and reconstructed theoretical distributions.

The only visible deviation is in the time delay distribution for the case of the Laguerre Gaussian detection mode (c). The origin of the deviation is an error in the reconstructed phase. For any particular implementation, the error is limited and depends on the optical properties and length of the crystal, as well as the spectral bandwidth. The spectral bandwidth is influenced by the detection mode, and the choice of a small detection beam waist corresponds to a broad spectrum, which allows to explore limitations of the method. The deviation in phase cannot be seen easily in Fig. 3.8 because it is comparatively small, but there is a quadratic error.

To gain some understanding of the error in the phase, it is useful to distinguish phases from two origins: First, phases stemming from the projection into spatial modes, and second, from the propagation through the nonlinear crystal (and possible further dispersive elements). While there are no issues with phases originating from the projection, the method is limited in the reconstruction of phases from the propagation through the crystal (and further dispersive elements).

Let us see why a difference exists between the two. The technique is based on shifting the relative frequencies of signal and idler photons, which is achieved by changing the crystal temperature (or pump frequency). The reason that such a change causes a relative shift in frequencies when Eq. (C.6) from Appendix C is used in Eq. (C.2), is the appearance of linear terms in both the temperature dependence (pump frequency) and biphoton frequency within the sinc function. In contrast, when using Eq. (C.4) in Eq. (C.2), the term in the biphoton wavefunction corresponding to the propagation through the crystal, the third line of Eq. (C.2), does not have the same relationship between the variables. Therefore, the phase from the propagation through the crystal is not appropriately shifted with the rest of the wavefunction. However, for the symmetrised form of the wavefunction, Eq. (C.7), the problem disappears when using a Taylor expansion up to leading order. As a result, only the linear term of the phase originating from the propagation through the crystal is reconstructed. The same thing happens when the photon pair propagates through additional dispersive elements after the down-conversion crystal.

To clarify this, a closer look into the numerical results for the Laguerre Gaussian case (Fig. 3.8 (c)) is instructive. In Fig. 3.9 (a), the error of the reconstructed phase is plotted. This is a quadratic error, which stems from the propagation of the photons to the end of the crystal, effectively a propagation through a thickness of $L/2$. In Fig. 3.9 (d), the already familiar original and reconstructed time delay distributions of the two photons are shown. To demonstrate that the quadratic phase not recovered by the method originates from the dispersion of the nonlinear crystal, Fig. 3.9 (b) and (e) show the results when a potassium titanyl phosphate (KTP) compensation crystal of length $L/2$, rotated by 90° compared to the

first crystal, is inserted after the down-conversion crystal. The addition of the compensation crystal has increased the quadratic phase that is not reconstructed by the method. Due to this increased error of the phase, the discrepancy between the corresponding reconstructed and original time delay distributions (Fig. 3.9 (e)) has increased. The time delay distribution has additionally been shifted, which is the usual purpose of such a compensation crystal. Fig. 3.9 (c) and (f) depict what happens if instead of inserting a compensation crystal, we artificially remove the quadratic phase shown in (a) from the biphoton wavefunction. In this case, the reconstructed phase and time delay distribution match the original ones well.

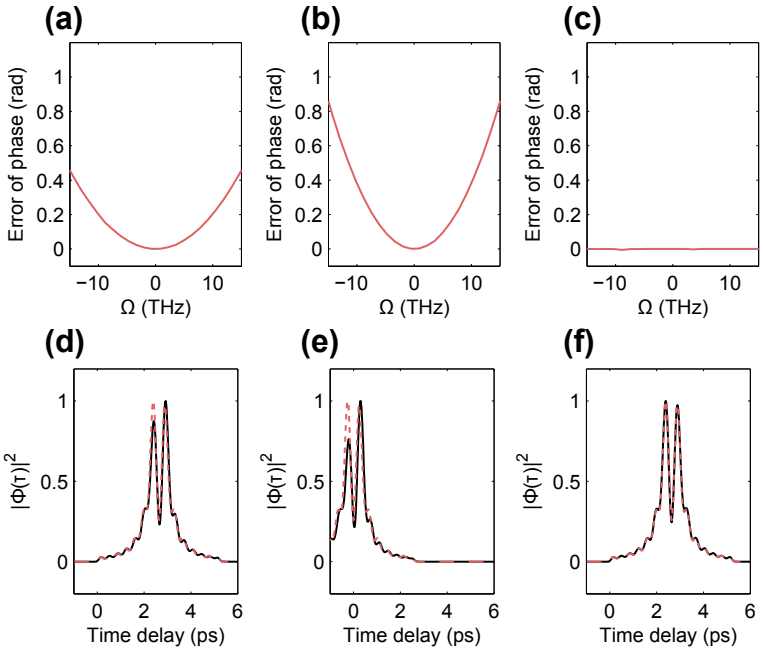

Figure 3.9: Numerical results of the error of the reconstructed phase (upper row) and of the original and reconstructed time delay distributions (black solid line and red dashed line, respectively, of the lower row), for some variations on the test case with Laguerre Gaussian detection modes (Fig. 3.8 (c)). (a) and (d) correspond to the original configuration as in Fig. 3.8 (c). (b) and (e) are with a KTP compensation crystal of length $L/2$, rotated by 90° compared to the down-conversion crystal, inserted in the collimated beam after the first crystal. For (c) and (f) the quadratic phase of (a) is artificially removed from the biphoton wavefunction.

Note that the discussed lack of sensitivity of the reconstruction method does not mean that it is only sensitive to odd functions of the phase, as the phase imparted through the spatial projection can be arbitrary and is recovered by the method.

Let us now return to the main results shown in Fig. 3.8 and take a look at the impact the detection mode has on the spectral wavefunction. A comparison of the three rows in Fig. 3.8 shows significant differences. The Gaussian detection with the crystal centred (a)

yields a quantum interference pattern that is symmetric with respect to ΔS, about a value that depends on the time delay acquired when signal and idler photons propagate through half the length of the nonlinear birefringent crystal. The phase of the wavefunction has a primarily linear trend due to this time delay, but it also undergoes jumps that stem from sign changes in the sinc terms contained in the wavefunction. The spectrum's departure from a sinc squared function is highlighted by its asymmetry. It arises from the use of a small detection beam waist, and also results in the asymmetry of the quantum interference pattern in the ΔT direction. The time delay distribution has a symmetric peak centred at the time delay acquired by propagation through half of the crystal. When the crystal is displaced (b), the quantum interference pattern becomes asymmetric, the phase changes, and the time delay distribution shifts, which is consistent with the results from Section 3.2 and Ref. [2]. Using the Laguerre Gaussian detection mode with the crystal centred (c) changes the structure of the quantum interference pattern markedly, even transforming the dip into a peak. The phase of the wavefunction is similar to the Gaussian case, but the spectrum has a side lobe. A change of the spectrum makes sense, since the doughnut shape of the LG detection mode leads to a preferential detection of photons with larger transverse momenta; due to spatio-temporal correlations, these photons with larger transverse momenta also tend to have larger Ω. Remarkably, the time delay distribution has a dip at the approximate axis of symmetry, which means that the probability of photons arriving with their mean time delay is suppressed.

In summary, in this subsection I proposed a method to reconstruct the complex spectral wavefunction of a biphoton, which addresses the original idea of Hong, Ou, and Mandel, although for type-II SPDC. The proposal is based on analytic results and the applicability of the approximations made was numerically verified for an experimentally realistic set-up. Corresponding results from an experimental implementation carried out by Alexander Büse were also shown for comparison. The essence of the proposed method lies in the fact that a change in temperature or pump frequency is approximately equivalent to a shift of the frequency for the symmetrised mode function that determines the quantum interference coincidence counts.

On the one hand, a limitation of the technique compared to some of the other methods is its restricted applicability. In particular, to manipulate the biphoton in the appropriate manner through the generation process, so that its wavefunction can be shifted as shown here, the argument of the phase matching function must be linear in the relative frequency Ω. This includes processes such as collinear and noncollinear type-II SPDC with or without periodic poling [8], but not type-I collinear degenerate down-conversion due to the group

[8] Details can be found in Appendix C.5

velocities of the two photons being equal. Moreover, post-emission spectral manipulation that does not comply with Eq. (3.20), such as the use of spectral filters or propagation through dispersive elements, will lead to a faulty reconstruction. This section has explicitly dealt with the case of the biphotons being in a pure state and produced by a monochromatic pump beam. As an extension, following the results in Ref. [104], $f(\Delta S, T, \omega_p)$ provides the Wigner function in the case of a mixed state. For the case of a pulsed pump where the biphoton wavefunction depends on both signal and idler frequencies, useful information could still be obtained: Provided that the bandwidth is not so wide as to produce problems with the phase in Eq. (3.20), $f(\Delta S, T, \omega_{0p})$ provides the Wigner function in which the sum-frequency variable has been traced out [9]. The reconstruction is unsuccessful at recovering the limited part of the quadratic and higher order phase that arises from the propagation of the biphoton to the end of the crystal. Whether the error causes a visible deviation depends on the relative contribution of the frequencies further from the degenerate frequency, which is influenced by the detection beam waist. Here I was deliberately working with small beam waists that provide relatively wide spectra, in order to probe limitations of the method.

On the other hand, a considerable advantage of the method lies in its simplicity, which extends from the experimental equipment and implementation right to the data analysis. The experimental resources consist of coincidence counting, temperature control of the nonlinear crystal, and a beam splitter. The experimental implementation of the technique is not faced with the challenging stabilisation requirements of interferometric measurements [93], or the inefficiencies causing a need for high pump powers [72], incurred by measurements that rely on nonlinear optical effects. The analysis is straightforward, since it is a closed form solution, and no iterative, complicated algorithm is required. This is in contrast to frequency-resolved optical gating (FROG) type measurements [94], which are a popular choice for bright coherent pulses, and have recently even be implemented on single photon pulses [109].

Lastly, the freedom to choose spatial pump and detection modes offers some interesting possibilities. The spectrotemporal properties of the biphoton are characterised after projection into a spatial mode. At first sight, the impression may arise that the spatial DOF would not play a role. However, as the results demonstrate, this is far from the truth, because the spatial modes can have a pronounced effect on the spectrotemporal properties, particularly due to spatio-temporal correlations in the biphoton wavefunction [85, 87, 110]. The method works for arbitrary paraxial pump and projection modes, so it is possible to influence the detected wavefunction by adjusting the modes.

[9] Details can be found in Appendix C.6

While this chapter has focused on the detection modes, the possibility of using the spatial pump mode to influence the spectrotemporal properties of the biphoton has also been established in the literature. The manipulation of biphoton spectrotemporal properties by tailoring the pump mode is demonstrated for type-I noncollinear SPDC in [111], and for the case of spontaneous four-wave mixing in [112]. It is also proposed and numerically shown in [113] for the case of SPDC in a semiconductor waveguide. Ref. [113] then goes on to present how spatial pump modes can be used for the measurement of the biphoton spectral Wigner function. In fact, similarly to the method introduced in this subsection, it is also based on the results from [104]. In a transverse pump configuration the spatial pump mode provides an alternative way of producing effective shifts in the relative frequencies and arrival times.

3.4 Conclusion

This chapter has investigated two topics, both related to the spectrotemporal DOF of biphotons produced in SPDC.

Section 3.2 demonstrated the possibility to influence the time delay of photon pairs through spatial manipulations. Changing the distance between crystal and collimating lens produces an effect that is to first approximation a shift in the time delay, although it is actually more subtle than that. Spatio-temporal correlations have been identified as underpinning the effect. While the effect occurs under a variety of different detection conditions, they have the property in common that not all photons are detected.

The significance of this work is both practical and scientific: The practical implications are that the crystal position is important in applications where the time delay between photons is crucial, such as in quantum interference, and where the compensation cannot be easily adjusted, for example when a given birefringent crystal is used to compensate the time delay in type-II SPDC, as opposed to having variable path lengths. It also points towards the prospect of more generally shaping the temporal properties of the biphoton via spatial manipulation. From a more fundamental point of view, the effect is interesting because the ability to manipulate one DOF through another is unintuitive.

In Section 3.3, a scheme was proposed that presents a new and convenient method for the usually rather challenging measurement of the complex spectral wavefunction. The scheme is based on the ability to tailor the wavefunction in a particular way during the generation process. The complex spectral wavefunction fully characterises the spectrotemporal DOF and therefore contains complete information about the state, given a fixed polarisation and spatial mode. One particularly valuable outcome is the ability to determine the distribution of time delays between the two photons in a pair. This distribution is often impossible to

measure directly, as the time delays can be much smaller than the timing resolution of a typical measurement apparatus.

Chapter 4

Multiwavelength optical activity measurements with entangled photons

The experiment presented in this chapter is a quantum metrology experiment where the interaction of light with chiral molecules is measured in the form of optical activity. The experiment brings together a number of previously encountered concepts: The nonclassical light used as the probe is created through SPDC, the control of which is the subject of Chapter 3. The sample used in the experiment is a solution of chiral molecules in water. One the one hand, the light-matter interaction can be thought of as a multitude of scattering events where a large number of "nanoscatterers" have random positions and orientations. On the other hand, the net result is well described by modelling the interaction using effective optical properties of the medium, as mentioned in Chapter 1. In addition, the theme of helicity from Chapter 2 is picked up again. However, notable differences also exist: In contrast to the former case of strong focusing, we now work with collimated beams so that helicity can be considered as being equivalent to circular polarisation. While Chapter 2 specifically deals with the helicity transformation upon scattering, here the helicity states are eigenstates of the transformation in question. The phenomenon of optical activity can in fact be understood as circular birefringence where the two circular polarisations pick up a different phase, and it is precisely this phase difference that we are interested in.

4.1 An introduction to optical activity

For over two centuries, people have observed the ability of certain media to rotate the plane of polarisation when linearly polarised light propagates through them. Such media are called optically active, and the polarisation rotation is depicted in Fig. 4.1. Optical

activity is related with another important effect called circular dichroism, which in turn manifests itself as linear polarisation becoming elliptical upon propagation [114]. The wide range of media that can naturally exhibit optical activity and circular dichroism have a crucial property in common: They are chiral, meaning that they are non-superimposable with their mirror image or, more formally, that no improper rotation can result in the same object [115, Sec. 1.9]. An improper rotation consists of a combination of a rotation about an axis and a reflection about a point lying on the axis or a plane orthogonal to the axis. As a consequence of the lack of improper rotation symmetry, a chiral object can exist in two distinct forms, that is with different handedness, and these two forms are related by a reflection, such as a mirror transformation. The optical activity caused by the two distinct forms is equal in magnitude but the rotation occurs in opposite directions. One can think of a helix as a simple example of a chiral object.

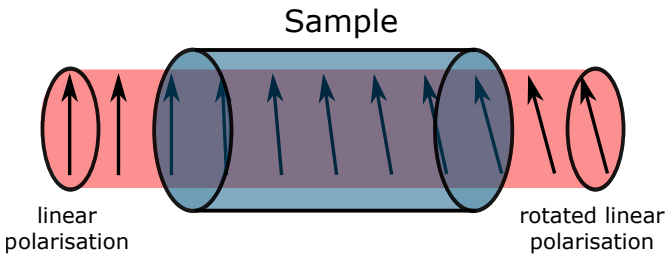

Figure 4.1: Manifestation of optical activity for a linearly polarised state of light, which is a rotation of that polarisation.

I will now provide a rough historical overview of the understanding of optical activity, based on Refs. [115–118]. The first study of optical activity dates back to 1811, when D. F. J. Arago conducted the following experiment illustrated in Fig. 4.2: He looked at sunlight through two polarisers, and inserted a quartz crystal, oriented to have its optical axis along the propagation direction, between the polarisers. He was able to observe coloured light passing through the second polariser, with the colour depending on the polariser angle. After continuing this line of experimentation J. B. Biot came up with a two-part explanation.

The first part is that the plane of linear polarisation rotates when the light propagates through the crystal. It is easy to appreciate that when the two polarisers have orthogonal orientations, rotation must occur for any light to pass through the second polariser. Later on, J. W. F. Herschel identified a correlation between quartz crystals of different handedness and the sign of the optical rotation. A link between the crystal structure and optical activity was established, which provided insight into the origin of optical activity for crystals. However, gases and liquids can also exhibit optical activity. L. Pasteur made the important realisation that the concept of chirality not only applies to crystal structures, but also to individual

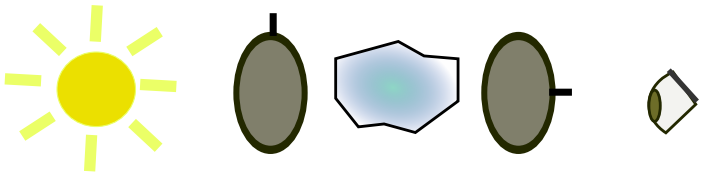

Figure 4.2: Sketch of the idea behind Arago's optical activity experiment. (The resemblance with current polarisers is only for illustration purposes, the implementation in 1811 naturally looked different.)

molecules. It is the chirality of the molecules that gives rise to the optical activity of solutions and gases.

Let us return to Arago's experiment. Aside from rotation of linear polarisation, a second idea is needed to explain the observation of coloured light coming through the second polariser: The rotation of light must be wavelength-dependent. This dependence is usually referred to as optical rotatory dispersion (ORD). Biot proposed a wavelength dependence of the form $\propto \frac{1}{\lambda^2}$, where λ is the wavelength. A. A. Cotton studied the wavelength dependence at absorption bands and established a connection between the characteristic shape of the ORD at absorption bands and circular dichroism, the differential absorption of RC and LC polarised light. Optical activity and circular dichroism are directly related to the real and imaginary parts, respectively, of a wavelength-dependent quantity called the chirality parameter [10]. Cotton's work made progress towards identifying the origin of both phenomena. This origin lies in the transition moments associated with optical transitions between molecular states with different energies. The role of optical transitions can also clearly be seen in the quantitative model for the ORD proposed by P. K. L. Drude in 1902, which is applicable not at the absorption bands themselves, but at longer wavelengths. The optical rotation takes the form

$$\alpha = \sum_j \frac{A_j}{\lambda^2 - \lambda_j^2}, \tag{4.1}$$

where the sum runs over different excitations labelled by j with resonant wavelengths λ_j and with weights A_j. In 1928 L. Rosenfeld developed a semi-classical model of optical activity that treats molecules quantum mechanically but the radiation classically [119]. There, the contributions from different resonances are related to parallel components of electric and magnetic dipole transition moments associated with transition between different states of the molecule.

Although the historical overview shows what a long time ago the study of optical activity began, the phenomenon attracts unwavering interest even to this day. Let us look at the reasons behind this. Optical activity is useful in the study of molecular structure: The

optical activity exhibited by molecules can reveal information about their stereochemistry, by which the three-dimensional arrangement of the constituent atoms is meant that has a bearing on their properties. Chirality also plays a crucial role in biology, since amino acids within proteins and sugars are all chiral with a particular handedness [115, 116]. The stereochemical features of biomolecules affect their biological function. Optical activity techniques are sensitive to these features and unlike the alternative of using x-ray methods, they are applicable to solutions and biomolecules in vivo [115]. This makes optical activity techniques valuable in biochemical studies. Chirality is also a pertinent concept in the pharmaceutical industry since many drugs are chiral [115, 120].

For the experiment presented in this chapter the key things to know about optical activity are as follows:

1. Optical activity can be understood as circular birefringence, i.e. a different phase is imparted on RC and LC polarised light.
2. The difference in phase is proportional to the path length in the optically active medium and under the conditions of interest it is also proportional to the concentration of the solution.
3. It further depends on the wavelength.

Although the effect of circular birefringence on linear input polarisation, which is to rotate that polarisation, appears to be the same as the action of a half waveplate (HWP), the properties of an optically active medium and the material used for a HWP are in fact different. HWPs are typically based on linear birefringence, not circular birefringence [121, Sec. 3.4]. The difference between linearly and circularly birefringent media becomes apparent when the path length is changed. For an optically active medium, the amount of rotation is proportional to the path length. This can intuitively be understood as a linear dependence on the effective number of interactions with molecules, which is why there is also a linear dependence on the concentration, provided the concentration is not too high. To facilitate the comparison of measurements under different conditions, the rotation is often provided in a normalised form, the so-called specific rotation, which is the rotation (in deg) divided by the path length (in dm) and concentration (in g cm^{-3}). In contrast to a circularly birefringent medium, for a linearly birefringent medium the amount of rotation of linear polarisation depends on the angle of the input polarisation, and is not proportional to the path length. In fact, linear polarisation does not in general remain linear when propagating through a linearly birefringent medium, a quarter waveplate (QWP) being a well-known counter example.

The wavelength dependence is of interest because as Eq. (4.1) shows, it reveals information about optical transitions between different molecular energy states. Sucrose solutions are used as the optically active medium in the experiment below. In the wavelength range

under study, sucrose exhibits notable optical activity but negligible circular dichroism, thus the light-matter interaction is a helicity preserving unitary transformation, simply imparting a different phase to the two helicities. Now, an attentive reader may have picked up on the fact that sucrose molecules are unlikely to be dual and this being a helicity preserving interaction despite a lack of duality seems to be surprising, given what is written in Section 1.2.3. Such concern is justified for a general scattering event. However, as discussed in our work [122] and in Refs. [123–125], the resolution lies in the fact that here we are only looking at a particular scattering direction, which is the forward direction, and that the sucrose solution exhibits cylindrical symmetry due to the statistical ensemble of molecules with random positions and orientations. Considering only one propagation direction for light in a system with cylindrical symmetry about that axis leads to helicity conservation because the total angular momentum of the light must be preserved and for a plane wave, the helicity determines the total angular momentum.

4.2 Context and motivation behind the experiment

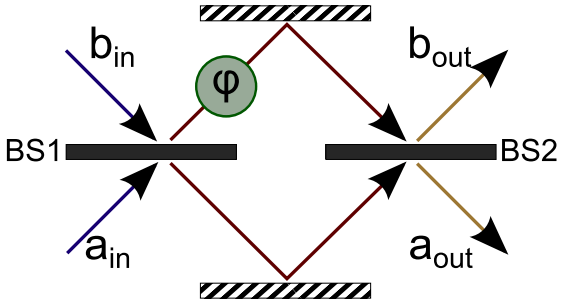

Figure 4.3: Mach-Zehnder interferometer: Two input modes are mixed by a first beam splitter (BS1), and the two output modes follow different paths that result in a phase difference φ, before incidence on a second beam splitter (BS2). The output modes of BS2 constitute the output of the interferometer.

After the introduction into the topic of optical activity, let us now see how it fits into quantum metrology. The archetypal example of phase measurement is a Mach-Zehnder interferometer (MZI) [126, Sec. 3.5]. In this interferometer, two paths emerge from a first beam splitter, and end at a second beam splitter, as illustrated in Fig. 4.3. The parameter of interest is a relative phase that is imparted on light between the two paths. This relative phase is caused by different effective path lengths, which can have a variety of origins, for instance a difference in the actual path lengths, or in the refractive indices within the two

paths. The classical measurement scheme consists in having a coherent state incident on one of the input ports of the first beam splitter (BS1), with vacuum in the other input mode, letting this coherent state be split into the two arms, be recombined at the second beam splitter (BS2), and finally measuring the intensity difference at the two output ports of BS2. This measurement results in a sinusoidal signal as a function of the phase difference. The period of the fringes is the same as for a single photon passing though the interferometer. The best achievable uncertainty for the coherent input scales as $\frac{1}{\sqrt{N}}$, where N is the mean photon number, and this is called the shot-noise limit or standard quantum limit [67],[20, Sec. 13.1]. The optimal uncertainty also scales the same way for a single photon experiment repeated N times such that the same mean photon number is used for the estimation [127].

The aim of quantum parameter estimation strategies is to employ quantum phenomena in order to increase the precision of the estimate for a given amount of resources. A generally applicable definition of resources in quantum metrology needs to take into account a variety of possible schemes, such as allowing multiple passes of photons through the phase element, or using an entangling rather than a linear interaction [128, 129]. However, for the experiment of this chapter, a more general definition of resources can be simplified to the rather intuitive meaning of the number of photons N.

Metrology schemes using quantum correlated states can outperform classical schemes. One approach is to use NOON states, where N photons are in a superposition of all being in one of two possible modes and all being in the other mode. The state picks up a phase difference between the terms of the superposition that is a factor of N larger than for a coherent state or single photon [23]. This results in an improvement over the shot noise by a factor of $\sqrt{N}$. The corresponding $\frac{1}{N}$ scaling of the uncertainty is the best scaling allowed by quantum mechanics and is called the Heisenberg limit. For the example of $N = 2$, the following implementation can be used: Let two indistinguishable single photons be incident on the first beam splitter, one at each input. Due to HOM interference, the photons will leave the beam splitter bunched, i.e. as a superposition of both photons together in either one of the interferometer arms. This is a NOON state with N=2. As a consequence they pick up twice the phase compared to a single photon. At the output of the second beam splitter, one can measure the expectation value of the photon number difference or the parity, which assigns a value of 1 to even and -1 to odd photon numbers [67]. Even though the path-based MZI is probably the most well-known example, other implementations of the same idea for phase estimation are also possible, with polarisation being one option. In that case the polarisation plays the role of paths, and the phase imparted needs to be polarisation-dependent.

Such polarisation-based implementations have been demonstrated a number times, for

example in Refs. [70, 130–138], and in [139] the two modes differ in both polarisation and path. Here I will focus on three works [136–138]. The closest to molecular optical activity is the experiment by Wolfgramm *et al.* of [137], which measures Faraday rotation. Faraday rotation is an effect that is very similar to natural molecular optical activity. There are two important differences: 1. It can be achieved with atoms that do not need to be chiral, but instead an externally applied magnetic field is necessary. 2. Natural molecular optical activity and Faraday rotation can be distinguished in an interesting manner: By placing a mirror behind the medium and letting the light travel back in a reverse pass through the medium. The final polarisation back at the starting position is the same as the initial polarisation if the rotation is due to natural optical activity, but is rotated twice compared to a single pass if the rotation is based on the Faraday effect [140, Sec. 6.4]. The reason behind this difference is that for the case of natural optical activity, the reverse pass is equivalent to a time reversal and must therefore lead back to the original state, whereas for the case of a Faraday rotation it is different from time reversal: Time reversal would require the direction of the magnetic field to be reversed, in addition to the propagation direction of the light [115, Sec. 1.9]. Incidentally, this property of the Faraday effect is utilised in optical isolators [140, Sec. 6.6]. In their experiment, Wolfgramm and co-workers use narrow-band photon pairs from type-II down-conversion, which can be rewritten as a NOON state in circular polarisation when the photons are indistinguishable (in analogy to the two-photon NOON state obtained from HOM interference, as discussed above for the MZI). This photon pair travels through a medium that induces Faraday rotation, namely a cell containing an ensemble of ^{85}Rb atoms in a magnetic field. The acquired phase is detected through coincidence measurements after a polarising beam splitter (acting as BS2 of the MZI).

NOON states with $N > 2$ can no longer be created deterministically through simple HOM interference as explained above. However, they can be obtained in a superposition of different N values using a method proposed by Hofmann and Ono in 2007 [141]. The state is created by combining a coherent beam and the output of SPDC on a beam splitter. The method was experimentally demonstrated by Afek and colleagues in 2010 [136], enabling them to measure a phase imparted by a liquid crystal phase retarder using post-selected NOON states of up to $N = 5$. More recently, the technique also allowed Israel and co-workers to utilise NOON states up to N=3 in a microscopy setting, where a polarisation-dependent phase difference is measured as a function of transverse position [138]. The phase difference in that experiment arises from the birefringence of the sample.

The essential difference between various classical and quantum precision limits lies in the scaling with the photon number, N. It carries significance from a theoretical point of view.

The question what limitations nature imposes on measurement precision through quantum mechanics is clearly a fundamental one. Also interesting from a quantum information perspective, entanglement criteria exist that establish a relationship between multipartite entanglement and the maximum achievable precision [142–144]. When it comes to more practical matters, obviously the photon number N strongly determines the actual precision that is achieved. In most cases, a given desired precision can be reached without any elaborate quantum metrological schemes, simply by increasing the number of photons within a classical scheme. This solution tends to be significantly more straightforward than the challenging creation of quantum correlated probe states with a high N [21, 145]. Hence, leaving aside their theoretical interest, quantum metrology approaches are only of practical value if an increase of the probe power is in some way hindered. This motivation is also pointed out in [137, 138, 145, 146].

Biological samples can fall into this category of delicate systems. A recent article by Taylor and Bowen [145] provides a thorough review on the current state of quantum metrology applied to the field of biology. My demonstration of optical activity measurements is carried out on sucrose solutions, which are not delicate. Nevertheless, it can be considered as a proof of concept for other optical activity studies of the kind. Since optical activity techniques are of interest in biochemistry, the motivation of optimising the precision for a fixed number of photons can be relevant in general. The damage to biological samples, as well as losses, are both wavelength-dependent. In these matters, near infrared light tends to strike a favourable balance between unwanted effects that dominate at shorter wavelengths (photochemical damage, dipole scattering, absorption of light by chromophores), and others that in turn take over at longer wavelengths (absorption of light by water and consequent heating of the sample) [145, 147]. Similarly to many of the works on polarisation-based quantum metrology mentioned above, quantum correlated photon pairs are also used in the below experiment to measure relative phases between polarisations, but with important differences: The design of the experiment accommodates distinguishable photons, which allows the use of nondegenerate photons. As we will see next, this, in turn, makes the set-up equivalent to having two MZIs and enables the measurement of multiwavelength properties.

4.3 Experimental design

The aim of this experiment is the study of optical activity as a function of wavelength through the use of entangled photons. In particular, we will focus on the optical rotations for two wavelengths at a time, as illustrated in Fig. 4.4, and consider the mean and difference of the rotations, denoted by $\overline{\alpha}$ and $\Delta\alpha$.

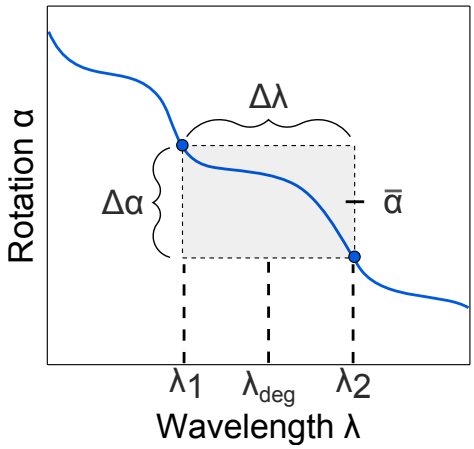

Figure 4.4: Illustration of the two quantities that can be accessed with the two types of input states: The state $|\Phi_{\text{in}}\rangle$ with correlated polarisations is sensitive to $\overline{\alpha}$, the mean of the optical rotations of the two wavelengths in question, while the state $|\Psi_{\text{in}}\rangle$ with anti-correlated polarisations is sensitive to $\Delta\alpha$, the difference of the two optical rotations.

Optical activity can be modelled as a unitary transformation of the form $U\left(\alpha\left(C,\lambda\right)\right) = \exp\left[-i\Lambda\alpha\left(C,\lambda\right)\right]$, where Λ is the helicity of light and $\alpha\left(C,\lambda\right)$ is the angle by which the linear polarisation of single photons gets rotated, which is a function of the wavelength of the light λ and of the concentration of the solution C. Although the rotation angle additionally depends on the path length and temperature, these parameters are not explicitly included here since they are held constant throughout the experiment. The transformation applied to a single monochromatic photon is $U\left(\alpha\left(C,\lambda\right)\right)|L,\lambda_m\rangle_n = \exp\left(-\mathrm{i}\alpha\left(\mathrm{C},\lambda_{\mathrm{m}}\right)\right)|L,\lambda_m\rangle_n$, and $U\left(\alpha\left(C,\lambda\right)\right)|R,\lambda_m\rangle_n = \exp\left(+\mathrm{i}\alpha\left(\mathrm{C},\lambda_{\mathrm{m}}\right)\right)|R,\lambda_m\rangle_n$, where $|P,\lambda_m\rangle_n$ symbolises a photon with polarisation P and wavelength λ_m in path n. The polarisation is L or R for left or right circular polarisation, which implies a helicity of 1 and -1, respectively. A typical classical way to measure optical activity consists in probing the interaction with linear polarisation and measuring the output polarisation as a projection in the horizontal-vertical (H-V) basis. The straightforward extension of this to the measurement of optical rotations at two wavelengths is to simply perform this measurement at each wavelength. Given the resource of two photons, it could be done either sequentially with two single photons, or with a separable photon pair where each photon has linear polarisation. Although single photons and photon pairs can be understood as non-classical objects in their own right, I will refer to this as the "classical" input state to indicate the lack of polarisation entanglement.

For the quantum scheme, two different types of biphoton input states are used. In both cases, the two photons are distinguishable: They are in separate paths, and they may additionally have unequal wavelengths. The input states are the following polarisation

entangled states:

$$|\Phi_{\text{in}}\rangle \equiv \frac{1}{\sqrt{2}}\left[|R,\lambda_1\rangle_1|R,\lambda_2\rangle_2 + \mathrm{e}^{i\alpha_0}|L,\lambda_1\rangle_1|L,\lambda_2\rangle_2\right] \tag{4.2}$$

$$|\Psi_{\text{in}}\rangle \equiv \frac{1}{\sqrt{2}}\left[|R,\lambda_1\rangle_1|L,\lambda_2\rangle_2 + \mathrm{e}^{i\alpha_0}|L,\lambda_1\rangle_1|R,\lambda_2\rangle_2\right]. \tag{4.3}$$

Here, $|P,\lambda_1\rangle_1|P',\lambda_2\rangle_2$ is shorthand for the two-photon composite system $|P,\lambda_1\rangle_1 \otimes |P',\lambda_2\rangle_2$. The phase α_0 will be referred to as the bias phase. The Bell states are recovered when $\alpha_0 = j\pi$, $j \in \mathbb{Z}$.

Through the interaction with the optically active medium, the states $|\Phi_{\text{in}}\rangle$, $|\Psi_{\text{in}}\rangle$ evolve to

$$\begin{aligned}|\Phi_{\text{out}}\rangle \equiv{}& \frac{1}{\sqrt{2}}\mathrm{e}^{i[\alpha(C,\lambda_1)+\alpha(C,\lambda_2)]} \\ &\times\left[|R,\lambda_1\rangle_1|R,\lambda_2\rangle_2 + \mathrm{e}^{i[\alpha_0-2(\alpha(C,\lambda_1)+\alpha(C,\lambda_2))]}|L,\lambda_1\rangle_1|L,\lambda_2\rangle_2\right] \qquad (4.4)\\ |\Psi_{\text{out}}\rangle \equiv{}& \frac{1}{\sqrt{2}}\mathrm{e}^{i[\alpha(C,\lambda_1)-\alpha(C,\lambda_2)]} \\ &\times\left[|R,\lambda_1\rangle_1|L,\lambda_2\rangle_2 + \mathrm{e}^{i[\alpha_0+2(\alpha(C,\lambda_2)-\alpha(C,\lambda_1))]}|L,\lambda_1\rangle_1|R,\lambda_2\rangle_2\right]. \qquad (4.5)\end{aligned}$$

The parameters of interest are $\overline{\alpha} \equiv \frac{1}{2}\left(\alpha\left(C,\lambda_1\right) + \alpha\left(C,\lambda_2\right)\right)$ and $\Delta\alpha \equiv \left(\alpha\left(C,\lambda_2\right) - \alpha\left(C,\lambda_1\right)\right)$. The aim within this experiment is not a joint measurement of the two parameters, but the individual measurement of either the mean or the difference rotation. These parameters can be estimated through coincidence measurement in the H-V basis. Rewriting the output states (4.4) and (4.5) in the H-V basis yields:

$$\begin{aligned}|\Phi_{\text{out}}\rangle \propto{}& \frac{1}{2\sqrt{2}}\left(1+\mathrm{e}^{i[\alpha_0-2(\alpha(C,\lambda_1)+\alpha(C,\lambda_2))]}\right)\left[|H,\lambda_1\rangle_1|H,\lambda_2\rangle_2 - |V,\lambda_1\rangle_1|V,\lambda_2\rangle_2\right] \\ &-\frac{i}{2\sqrt{2}}\left(1-\mathrm{e}^{i[\alpha_0-2(\alpha(C,\lambda_1)+\alpha(C,\lambda_2))]}\right)\left[|H,\lambda_1\rangle_1|V,\lambda_2\rangle_2 + |V,\lambda_1\rangle_1|H,\lambda_2\rangle_2\right] \qquad (4.6)\\ |\Psi_{\text{out}}\rangle \propto{}& \frac{1}{2\sqrt{2}}\left(1+\mathrm{e}^{i[\alpha_0-2(\alpha(C,\lambda_1)-\alpha(C,\lambda_2))]}\right)\left[|H,\lambda_1\rangle_1|H,\lambda_2\rangle_2 + |V,\lambda_1\rangle_1|V,\lambda_2\rangle_2\right] \\ &+\frac{i}{2\sqrt{2}}\left(1-\mathrm{e}^{i[\alpha_0-2(\alpha(C,\lambda_1)-\alpha(C,\lambda_2))]}\right)\left[|H,\lambda_1\rangle_1|V,\lambda_2\rangle_2 - |V,\lambda_1\rangle_1|H,\lambda_2\rangle_2\right]. \qquad (4.7)\end{aligned}$$

The expectation values of the HH and VV coincidences are therefore $\frac{1}{4}\left(1+\cos\left(\theta\right)\right)$, while the mixed coincidences HV and VH give $\frac{1}{4}\left(1-\cos\left(\theta\right)\right)$, where $\theta = \alpha_0 - 2\left(\alpha\left(C,\lambda_1\right) + \alpha\left(C,\lambda_2\right)\right) = \alpha_0 - 4\left(\overline{\alpha}\left(C,\lambda_1,\lambda_2\right)\right)$ when $|\Phi_{\text{in}}\rangle$ is used, and $\theta = \alpha_0 - 2\left(\alpha\left(C,\lambda_1\right) - \alpha\left(C,\lambda_2\right)\right) = \alpha_0 + 2\left(\Delta\alpha\left(C,\lambda_1,\lambda_2\right)\right)$ for $|\Psi_{\text{in}}\rangle$. From here we see that the mean rotation can be measured with $|\Phi_{\text{in}}\rangle$ as the input state, and the dispersion is directly accessible with $|\Psi_{\text{in}}\rangle$. Clearly, the

measurement schemes exhibit sensitivity to the parameters of interest, but before moving on to the experimental implementation, let us analyse how well they perform.

Adopting the matrix formalism to represent states by vectors and operators by matrices, and using the Pauli matrices σ_m with $m \in \{x, y, z\}$, the unitary transformation of optical activity for a single photon in the left-right (L-R) basis takes the form of $U_{LR}\left(\alpha\left(C,\lambda\right)\right) = \exp\left[-i\sigma_z\alpha\left(C,\lambda\right)\right]$, while in the H-V basis it is $U_{HV}\left(\alpha\left(C,\lambda\right)\right) = \exp\left[-i\sigma_y\alpha\left(C,\lambda\right)\right]$. Writing it in this way elucidates its role in terms of the Poincaré sphere: Optical activity is a rotation of the polarisation state about the y-axis of the sphere (the L-R axis).

For the case of a photon pair, the experiment contains four modes that are pairwise coupled, in the same way as a set-up consisting of two MZIs. The transformation in the H-V basis becomes $U\left(\alpha\left(C,\lambda_1\right),\alpha\left(C,\lambda_2\right)\right) = \exp\left[-\mathrm{i}\alpha\left(\mathrm{C},\lambda_1\right)\left(\sigma_{\mathrm{y1}}\otimes\mathbb{1}_2\right) - \mathrm{i}\alpha\left(\mathrm{C},\lambda_2\right)\left(\mathbb{1}_1\otimes\sigma_{\mathrm{y2}}\right)\right]$, with the subscripts indicating to which of the two photons the property belongs or operator applies, and $\mathbb{1}$ being the identity matrix. Using $\overline{\alpha}$ and $\Delta\alpha$ and assuming the concentration of the solution is the same for the two photons, the two-photon transformation can be rewritten as

$$\begin{aligned} U'\left(\overline{\alpha}\left(C,\lambda_1,\lambda_2\right),\Delta\alpha\left(C,\lambda_1,\lambda_2\right)\right) &= \exp\Bigg[-i\big(\overline{\alpha}(C,\lambda_1,\lambda_2)(\sigma_{y1}\otimes\mathbb{1}_2+\mathbb{1}_1\otimes\sigma_{y2}) \\ &\quad +\frac{1}{2}\Delta\alpha(C,\lambda_1,\lambda_2)(\mathbb{1}_1\otimes\sigma_{y2}-\sigma_{y1}\otimes\mathbb{1}_2)\big)\Bigg]. \end{aligned} \tag{4.8}$$

As all of the operators commute, the overall action can thus be considered as a sequence of two transformations, in either order: A rotation of the polarisation of the two photons in the same direction, and a rotation in opposite directions. The generators of the groups can immediately be identified as $\hat{H}_{\mathrm{col}} \equiv (\sigma_{y1}\otimes\mathbb{1}_2 + \mathbb{1}_1\otimes\sigma_{y2})$ belonging to the parameter $\overline{\alpha}(C,\lambda_1,\lambda_2)$ and $\hat{H}_{\mathrm{dif}} \equiv \frac{1}{2}\left(\mathbb{1}_1\otimes\sigma_{y2} - \sigma_{y1}\otimes\mathbb{1}_2\right)$ belonging to the parameter $\Delta\alpha(C,\lambda_1,\lambda_2)$. Knowing the generators of the transformation is useful because it allows to assess the choice of measurement for a given probe state. This can be understood by considering a quantity called Fisher information (FI). The FI is a measure of the information about a parameter that is provided by a measurement scheme, and is related to the achievable precision via the Cramér-Rao bound: $\Delta\theta \geq \frac{1}{\sqrt{I(\theta)}}$, with θ being the parameter to be estimated, $\Delta\theta$ its uncertainty, and $I\left(\theta\right)$ the FI. It is defined as $I\left(\theta\right) \equiv \sum_i p(x_i|\theta)\left(\frac{\partial \ln p(x_i|\theta)}{\partial\theta}\right)^2$, where $p(x_i|\theta)$ is the probability of obtaining the measurement outcome x_i given the parameter value of θ, and the sum is taken over all measurement outcomes of the positive operator valued measure (POVM) [20, Sec. 13.1.1]. The quantum Fisher information (QFI) is the FI optimised over all POVMs, and for a pure state it can be calculated as $I_{\mathrm{q}} = 4(\Delta\hat{H})^2 = 4(\langle\hat{H}^2\rangle - \langle\hat{H}\rangle^2)$, where $\hat{H}$ is the generator of the unitary transformation [144]. If the QFI is found to be equal to the

FI, then the choice of POVM is optimal. In the literature, such an investigation can be found for the case of a conventional (two-mode) MZI, where photon counting measurements in the output arms (equivalent to H-V projections in our framework of polarisation-based phase estimation) were shown to be optimal for any path-symmetric pure state [148]. Furthermore, for a four-mode, two-MZI set-up equivalent to our measurement of the rotation difference, photon counting measurements were shown to be optimal for singlet states [149]. However, this is a four-mode case and we are interested in the mean rotation in addition to the difference rotation. The FI and QFI for the states from above were therefore compared in a similar way, and they were found to be equal. The values for the different input states are given in Table 4.1, which allows a comparison of the different schemes for the same resources of two photons. The distribution between the two parameters is particularly noteworthy: The quantum probe states are sensitive to one parameter each while insensitive to the other. If both parameters are of interest, then the FI of two classical photon pairs is equal compared to choosing one of each quantum input photon pair. However, to estimate either one of the two parameters alone, the quantum schemes provide a factor of two increase in the FI, which can result in an enhancement of the precision by $\sqrt{2}$. In contrast, the factor of four difference between the FI of $\overline{\alpha}$ and $\Delta\alpha$ is merely due to the choice of definitions and carries no special significance.

	classical	$\|\Phi_{\text{in}}\rangle$	$\|\Psi_{\text{in}}\rangle$
$\overline{\alpha}$	8	16	0
$\Delta\alpha$	2	0	4

Table 4.1: Fisher information for three two-photon input states (columns) with respect to the two parameters of interest, namely the mean rotation $\overline{\alpha}$ and rotation difference $\Delta\alpha$. The classical input state can be two single linearly polarised photons or a pair of linearly polarised photons (with singles or coincidence detection). The quantum correlated input states $|\Phi_{\text{in}}\rangle$ and $|\Psi_{\text{in}}\rangle$ are given in Eqs. (4.2) and (4.3). In all cases, the FI and QFI are equal, indicating that the projective measurements in the H-V basis are optimal.

4.4 Experimental implementation

The experiment consists in the measurement of the wavelength-dependent optical activity of sucrose solutions at two concentrations. Using polarisation entangled photon pairs in the scheme described above, the mean rotation and rotation difference are measured for a number of wavelength pairs centred around the degenerate SPDC wavelength. The experimental

set-up with which the idea is implemented is sketched in Fig. 4.5. It can be understood as consisting of three main parts: State preparation, light-matter interaction, and measurement.

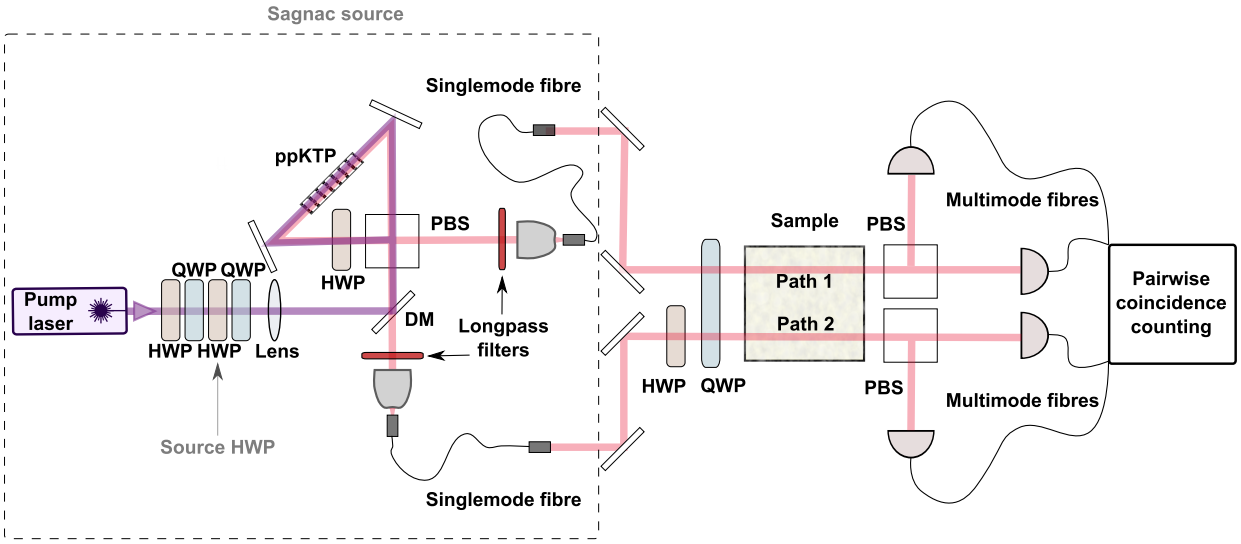

Figure 4.5: Schematic of the experimental set-up. Wavelength tunable polarisation-entangled photon pairs in separate paths are created by type-II SPDC in a polarisation-based Sagnac interferometer, as detailed in Appendix D. The preparation of the desired polarisation state is then completed by the half waveplate (HWP) and quarter waveplate (QWP) before the sample (the HWP setting determines whether $|\Phi_{\text{in}}\rangle$ of Eq. (4.2) or $|\Psi_{\text{in}}\rangle$ of Eq. (4.3) is selected). Next, the photons propagate through the sample, which consists of a cuvette with a path length of 20 mm filled with either water or a sucrose solution. Afterwards, each photon is incident on a polarising beam splitter (PBS), followed by multimode fibre coupling and detection with avalanche photodiodes (APDs). A coincidence logic enables the detection of the four types of coincidences in the H-V basis (HH, HV, VH, VV).

1. State preparation: Type-II SPDC in a Sagnac interferometer is used to create a polarisation entangled state [150, 151]. The details about this quantum source, which will from now on be referred to as a Sagnac source, are explained in Appendix D. Here it suffices to note that the purpose of the Sagnac source is the generation of the state

$$|S\rangle \equiv \frac{1}{\sqrt{2}}\left[|H,\lambda_1\rangle_1|V,\lambda_2\rangle_2 - \mathrm{e}^{i\alpha_0}|V,\lambda_1\rangle_1|H,\lambda_2\rangle_2\right], \tag{4.9}$$

and that the bias phase α_0 can be controlled with a HWP inside the source. The photons are coupled into SMFs, outcoupled, and brought into two modes with beam waists of 1.2 mm, vertically separated by approximately 1 cm. Bat ears applied to the SMFs compensate for unwanted polarisation transformations in the fibres and subsequent mirrors, ensuring that the polarisation state at the beginning of the paths still has the form of (4.9). Next, one of the photons passes through a HWP which can be set either to 90° or 45° relative to

the horizontal axis. This choice determines whether $|\Psi_{\text{in}}\rangle$ or $|\Phi_{\text{in}}\rangle$ is created. Finally, both photons pass through a QWP to convert the linear polarisations to circular polarisations.

2. Interaction: The interaction takes place as both photons travel through the same sample, which provides a path length of 20 mm. The content of the cuvette is either pure water (water HPLC grade from Hartenstein GmbH) or a sucrose solution (using the same water and D(+)-Sucrose pure Ph. Eur., NF from Hartenstein GmbH) with a concentration 0.2 ± 0.002 g/ml or 0.4 ± 0.008 g/ml, at a temperature of 19 ± 1 °C.

3. Measurement: After the cuvette, the photons are separately detected. Each photon is incident on a polarising beam splitter and subsequently coupled into one of two multimode fibres (four in total for the two photons), from where it is detected with APDs. Analysing the coincidences, this yields the four possible coincidence detection events HH, HV, VH, and VV.

To tune the wavelengths of the photons, it is possible to make use of the impact of the crystal temperature on the phase matching conditions, which is already familiar from Chapter 3. Tuning the crystal temperature linearly changes the difference between the two wavelengths, $\Delta\lambda$, by shifting the wavelengths relative to a fixed degenerate wavelength. In Fig. 4.6 (a) the dependence of the peak wavelengths of the two photons on the temperature is shown, as measured with a single photon spectrometer after each of the SMFs that emerge from the Sagnac source. An example spectrum is given in Fig. 4.6 (b). Note that the biphoton spectrum that is relevant for coincidence measurements is in general not exactly the same as the spectrum obtained through singles detection by the spectrometer. This is because not every event that contributes to the singles also contributes to the coincidences. For the purposes of the experiment, however, it is of interest that the measured bandwidth of 0.5 nm full width at half maximum (FWHM), which is largely determined by the beam waist of the detection mode, indicates a small bandwidth of the photons compared to the approximately 18 nm range over which $\Delta\lambda$ is tuned. For the optical activity measurements five equidistant settings of $\Delta\lambda$ between 0 and 17.7 nm are used, and the degenerate wavelength is 809.7 nm.

For a calibration of the measurements that accounts for experimental imperfections and details, the dependence of the coincidence counts on the phase is required. The calibration curve can then be used for the estimator, to map the coincidences from the optical activity measurements to a phase. The bias phase α_0 in expressions (4.2), (4.3) can be conveniently controlled using a HWP in the Sagnac source, namely the second HWP in the set of four waveplates used to prepare the pump beam polarisation. This HWP determines the relative phase between the equal H and V components of the pump beam polarisation, and consequently the relative phase between the two propagation directions in the Sagnac loop; the bias phase α_0 is four times the HWP angle. The output of the coincidence counts for a

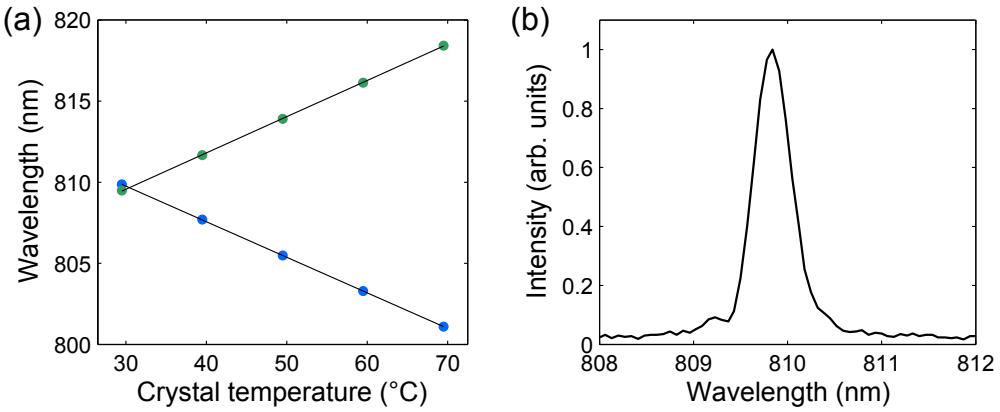

Figure 4.6: Spectral characterisation of the photon pairs. (a) The dependence of the central wavelengths of signal and idler photons as a function of crystal temperature. Data points correspond to measured values, while the lines show fitted linear functions. (b) An example spectrum of one of the photons, obtained with a spectrometer.

scan over different angles of this HWP, converted to an equivalent bias phase, is depicted for $|\Psi_{\text{in}}\rangle$ in Fig. 4.7. The information of the four different coincidence counts from (a) can also be combined into the curve of part (b) as detailed in the caption. The control of the bias phase works for both input states $|\Phi_{\text{in}}\rangle$ and $|\Psi_{\text{in}}\rangle$. The results for the $|\Phi_{\text{in}}\rangle$ state are very similar to Fig. 4.7. The experimental precision of the optical activity measurements depends on the bias phase, so it is set to a suitable value in advance. As shown in more detail later on, the aim is reaching a section of the curve midway between a maximum and minimum to optimise the experimental precision. The required setting was found to depend on the crystal temperature used, as shown in Fig. 4.8. This dependence is most likely due to dispersive birefringent elements, such as waveplates, in the set-up.

The experimental state preparation is not perfect. In order to check how close the experimental input states are to the desired states (4.2) and (4.3), the following additional measurement was performed: A HWP was inserted behind the sample (simply the cuvette filled with water), and the coincidences were measured as a function of this HWP angle using degenerate photons. We can expect a curve similar to when optical activity is probed at the degenerate wavelength, but with freely tunable rotation; a HWP rotation by an angle β produces $\alpha(\lambda_1) = \alpha(\lambda_2) = 2\beta$. Therefore, the mean rotation $\overline{\alpha}$ probed by $|\Phi\rangle$ depends on the HWP angle, and the measurement outcomes as a function of $\overline{\alpha}$ should be sinusoidal curves with a quarter of the period compared to the curve as a function of α_0 obtained by rotating the source HWP. In contrast, the rotation difference $\Delta\alpha$ probed by $|\Psi\rangle$ is zero, so the measurement outcomes should exhibit no dependence on the HWP angle. The measurement results in Fig. 4.9 (a) and (b) indeed show the expected sinusoidal and

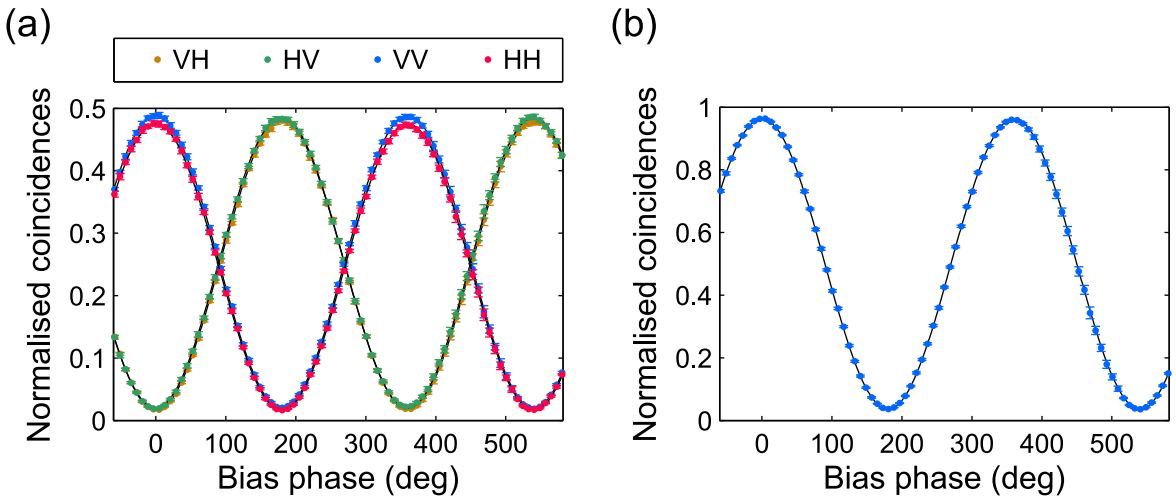

FIGURE 4.7: Calibration of the measurement outcome as a function of phase in the biphoton state, which is controlled with the Sagnac source HWP. The measurement results can be expressed by the four individual normalised measurement outcomes HH, HV, VH, VV as shown in (a), or by the combined quantity $\frac{\sqrt{HH \times VV}}{\sqrt{VH \times HV}+\sqrt{HH \times VV}}$ as shown in (b). The error bars cover intervals of $\pm$ one standard deviation obtained from 20 repetitions of each measurement, using the state $|\Psi\rangle$ with $\Delta\lambda = 0$ on a cuvette filled with water.

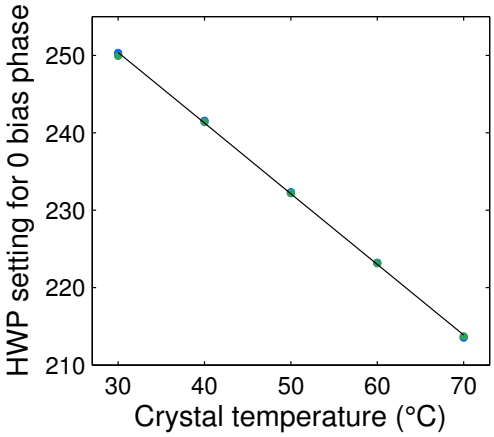

FIGURE 4.8: Calibration of the Sagnac source HWP across different crystal temperatures. The required settings of the HWP to maintain a constant phase of the biphoton quantum state vary with the crystal temperature. The data points are measured values with the two types of input states distinguished by colour (but these are almost on top of each other), while the line shows a fitted linear function.

zero dependence, respectively. Except for experimental imperfections, they reflect what is expected from Section 4.3 and Table 4.1. They can also be compared to HWP measurement results for a separable photon pair, presented in Fig. 4.10. Coincidence measurements on the classical state yield two of the four curves with the same period as the quantum state,

and such a reduced period oscillation is commonly referred to as super-resolution. However, due to the lower amplitudes of those curves, the super-resolution does not result in the same sensitivity. This is an example demonstrating the fact that super-resolution does not imply super-sensitivity, i.e. sensitivity beyond the standard quantum limit [132, 137, 152]. Unlike the super-resolution coincidence curves, the singles shown in Fig. 4.10 (b) have full amplitude, but the period is doubled.

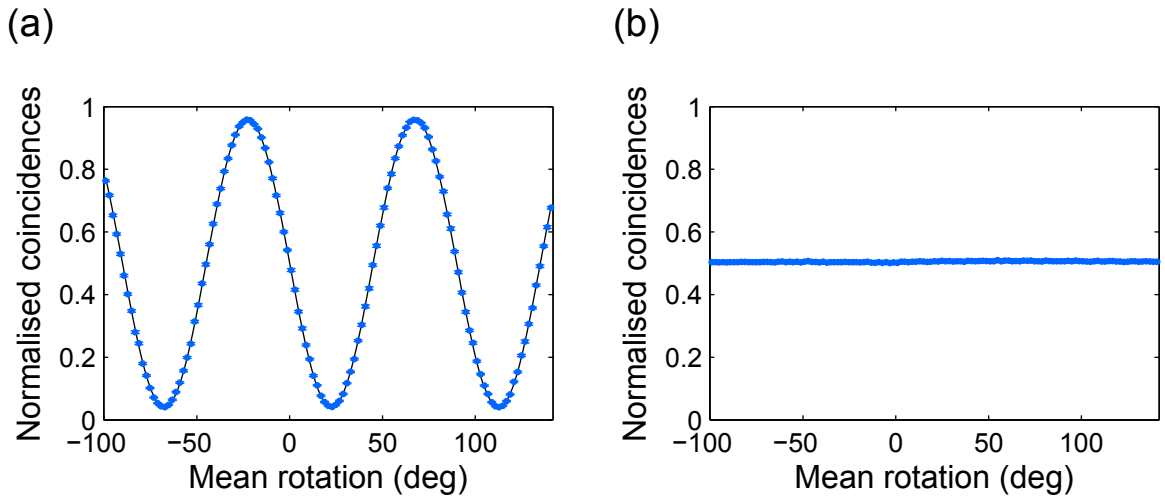

Figure 4.9: Test of the experimental quantum state by rotating a HWP behind the sample at the degenerate wavelength setting. (a) For the state $|\Phi\rangle$, a rotation of the HWP imparts a relative phase between the two terms. In an ideal case, the fringes would have unity visibility. (b) For the state $|\Psi\rangle$, a rotation of the HWP has almost no effect. Ideally, there would be no phase difference, which would result in a zero signal. The error bars show ± one standard deviation intervals obtained from 20 repetitions of each measurement.

The sinusoidal curves of Fig. 4.7 and 4.9 all have imperfect visibilities $\left(\text{vis} \equiv \frac{\text{max}-\text{min}}{\text{max}+\text{min}}\right)$ below one. The combined coincidences from the calibration with the source HWP, an example of which is given in Fig. 4.7 (b), had visibilities between 91.4% and 93.6% over all the different crystal temperature settings in use. Given the low level of accidentals in the experiment ($\sim 0.6\%$ of coincidences), the visibilities indicate a discrepancy between the experimentally prepared states and the target states (4.2) and (4.3), and hence, a potential for improvement. To locate the origin of the imperfections, different sections of the set-up were checked. The background-corrected visibility of the state at the output of the Sagnac source was still significantly better, 98.0% in the diagonal-antidiagonal basis. Since tests of the sample cuvette and detection apparatus showed that their contribution to unwanted polarisation effects was negligible, the remainder of the drop in the visibility was likely to

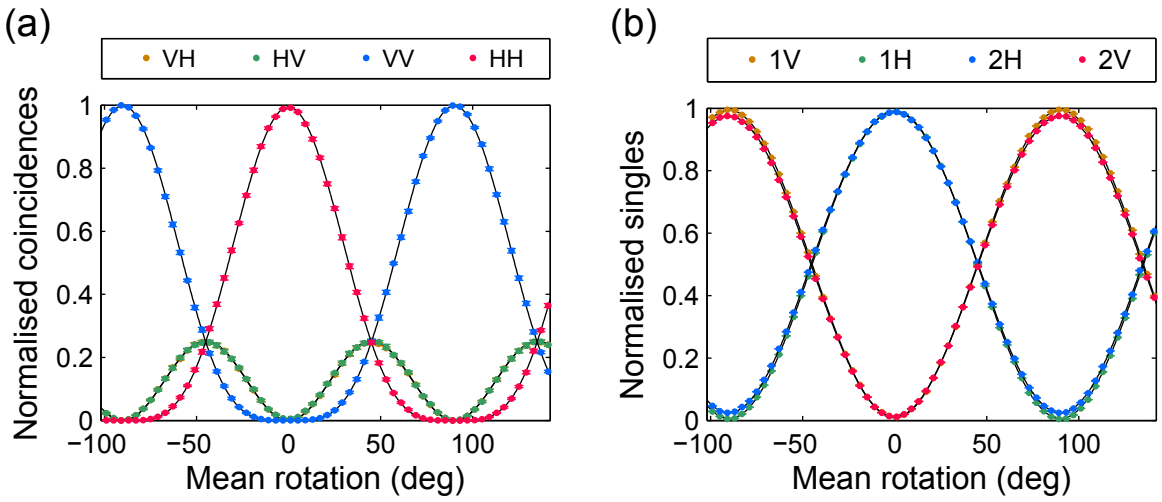

FIGURE 4.10: Classical measurement results for a rotation of a HWP behind the sample, i.e. the classical counter-part to the results of Fig 4.9. A separable photon pair with linear polarisations was used and the coincidences (a) and singles (b) were recorded in the H-V basis.

occur during the transfer of the photons from the Sagnac source to the sample. In this regard classical states tend to be better, as evidenced by the visibilities in Fig. 4.10.

The visibilities have an impact on the amount of available information. This can intuitively be understood from the fact that the signal obtained for a change in the phase drops with a decrease in visibility. Moreover, the experimental imperfections that are responsible for a decreased visibility introduce a phase dependence of the FI, which exhibits no such dependence under ideal conditions (see Table 4.1). A very similar point was made in [148], and Refs. [70, 152] also show that the FI depends on the visibility. As evident from Fig. 4.11, the impact of a decrease in visibility is most pronounced at the extreme points of the coincidence count curves. This figure provides a comparison of the FI as a function of the mean rotation for three cases. The case of an ideal implementation of the proposed scheme with entangled photons is shown by the green, upper horizontal line. The FI for the experimental implementation, inferred from the fitted curve of the test measurements for $|\Phi\rangle$ with the rotation produced by a HWP behind the sample, is shown by the blue curve. It accounts for all the experimental details that lead to a reduced visibility, but not for the losses, because it is based on data post-selected for coincidences. Since standard equipment was used, the losses in the experiment are significant; without accounting for the SMF coupling of the photons in the Sagnac source and for the detection efficiency of the APDs, the single photon transmission through the set-up was typically 46-56%. However, losses in the experiment could be much reduced by using high efficiency detectors and anti-reflection coated elements throughout. The case of an ideal implementation where either separable linearly polarised

photon pairs are used or two repetitions with a single linearly polarised photon is depicted by the red, lower horizontal line. Although due to the visibility below one, the experimental FI does not reach the ideal value for entangled photons, it surpasses the classical FI in regions away from the extrema of the coincidence curves. The optimal values correspond to the midway positions between the maxima and minima of the coincidence count curves. The desired section can be reached by tuning the bias phase α_0, which horizontally shifts the curves of Figs. 4.9 and 4.11. Based on the calibration curve of Fig. 4.7 for the input state $|\Psi\rangle$, a similar result for the inferred experimental FI can be expected for the rotation difference $\Delta\alpha$, but with all the FI values rescaled.

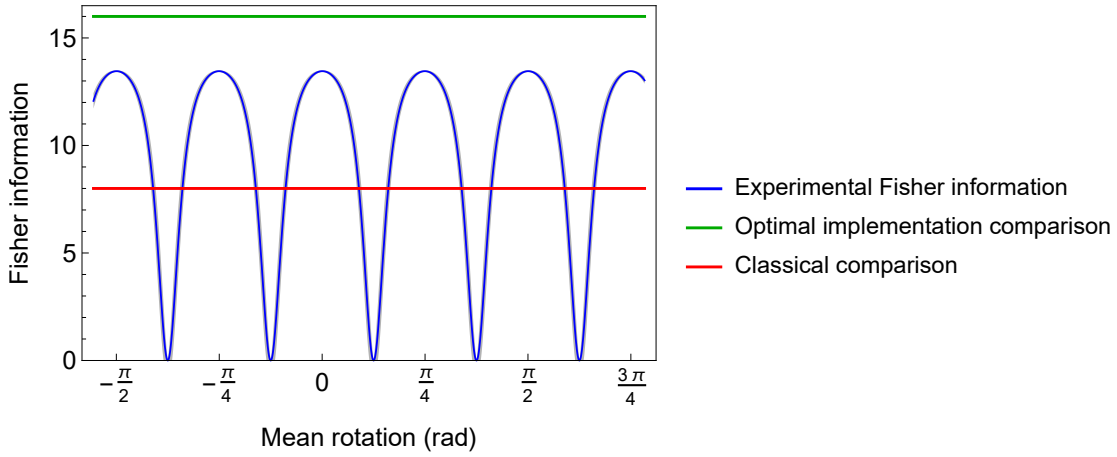

Figure 4.11: Comparison of the Fisher information as a function of the mean rotation for different lossless cases. The experimental FI inferred from the fitted curve of the test measurements for $|\Phi\rangle$ with the rotation produced by a HWP behind the sample is shown in blue. The very narrow lighter blue shaded region represents the uncertainty ($\pm$ one standard deviation), as obtained from the uncertainty of the fit parameters with standard error propagation. The inferred experimental FI is presented alongside the FI from an ideal implementation of the quantum measurement scheme in green (upper horizontal line), and the FI corresponding to a an ideal classical measurement with linearly polarised photons in red (lower horizontal line).

To enable the mapping to a phase, which is based on a comparison with the calibration curves, normalised coincidences are calculated from the raw number of detection events. The combined quantities $\frac{\sqrt{VH\times HV}}{\sqrt{VH\times HV}+\sqrt{HH\times VV}}$ and $\frac{\sqrt{HH\times VV}}{\sqrt{VH\times HV}+\sqrt{HH\times VV}}$ are invariant with respect to multiplicative factors applied to any of the detection channels, or a combination thereof (see Supp. Inf. of [153]). This means that they should be robust to variations in the number of photon pairs created or transferred from the Sagnac source to the remainder of the set-up, as well as in the detection efficiencies. Nevertheless, experimentally, the inferred phase was observed to slightly depend on some of these factors even when the sample was not changed. Moreover, certain other experimental conditions that will be mentioned below can

also affect the phase. Attempts to eliminate such effects were assessed by monitoring the photon statistics. When counting coincidences per time interval for a fixed setting of the experiment, a Poisson distribution is expected, and Fig. 4.12 shows an experimental example that is quite close. Fluctuations in excess of a Poisson distribution were not completely eliminated at all times, but could be significantly reduced by the measures listed below. For an example data set, the value of the variance divided by the mean, which is one for a Poisson distribution, was lowered from 154 to 1.14 by these actions.

- Vibrations within the Sagnac source were reduced by constructing a box around it and removing the temperature controller of the crystal, which contains moving parts, from the box.
- By insulating this box, the temperature on the inside was stabilised to within 0.1 °C, in contrast to the $\sim$ 1 °C fluctuations on the outside.
- Since the polarisation transformation in the SMF is temperature-dependent, the temperature of the fibres that connect the Sagnac source with the optical activity set-up was stabilised. This was achieved by laying the fibres flat on the optical table wherever possible, and applying insulating tape (Tesa Moll) from above.
- A stable operating condition was found for the pump laser through careful selection of its operating current.
- Detectors were selected that had minimal fluctuation of the detector efficiencies.
- Air bubbles in the liquid were avoided through careful filling of the cuvette.

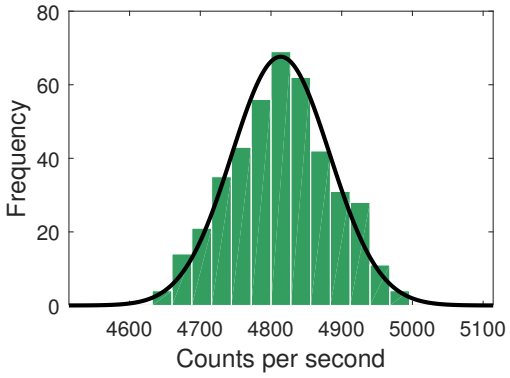

Figure 4.12: Photon statistics. An example of experimental photon statistics (number of VV coincidences per second, acquired over seven minutes) is presented by the histogram. For comparison, a Poisson distribution is shown by the black line.

4.5 Optical activity measurement results

The optical activity of sucrose as a function of wavelength can be modelled by Eq. (4.1), with a single transition characterised by the coefficients $j = 1$, $A_1 = 2.1648 \times 10^7$ deg nm^2 dm^{-1} g^{-1} mL and $\lambda_1 = 146$ nm from [154]. The result is shown in Fig. 4.13, with an additional close-up on the region that is probed in the experiment.

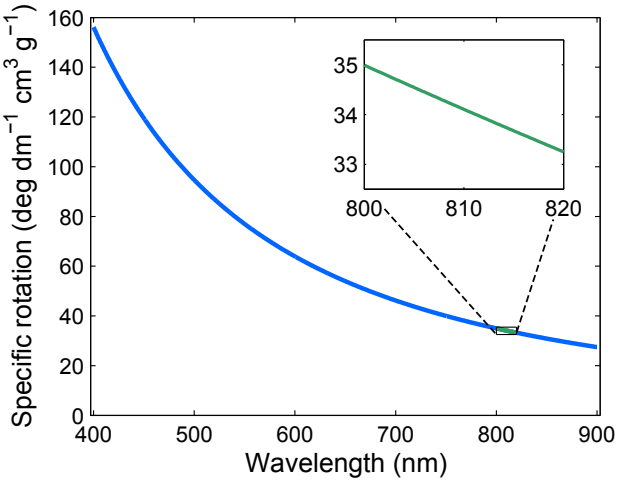

Figure 4.13: The optical activity of sucrose as a function of wavelength, as predicted by the model of Eq. (4.1). The inset shows a magnification of the optical activity in the spectral region probed within the experiment.

For the optical activity measurement a sequence of seven-minute sets was taken, which consist of one-second acquisitions recording the four types of coincidences. For each of the two input states, each of the two sucrose concentrations, and each of the five crystal temperatures, one data set was taken with water, and one with a sucrose solution. The measurement results are shown in Fig. 4.14. Part (a) contains the results for mean rotations and (b) for the rotation differences. Overlaid are the curves predicted by the model of Eq. (4.1) with the parameters specified above. Due to the optical activity being proportional to the concentration, for both means and differences the values for the higher concentration 0.4 g/ml are expected to be a factor of two larger than for the lower concentration of 0.2 g/ml. The reason behind the mean rotations being approximately constant and the rotation differences being linear functions is that as shown in Fig. 4.13, the ORD curve is nearly linear within the spectral region that is probed. This is not generally true for different media, centre wavelengths, and wavelength ranges.

Not all data points fall within one standard error from the model. In particular, for the optical rotation difference measurement at a concentration of 0.4 g/ml, there appears to be a systematic error based on the fact that all the measured values are below the predictions.

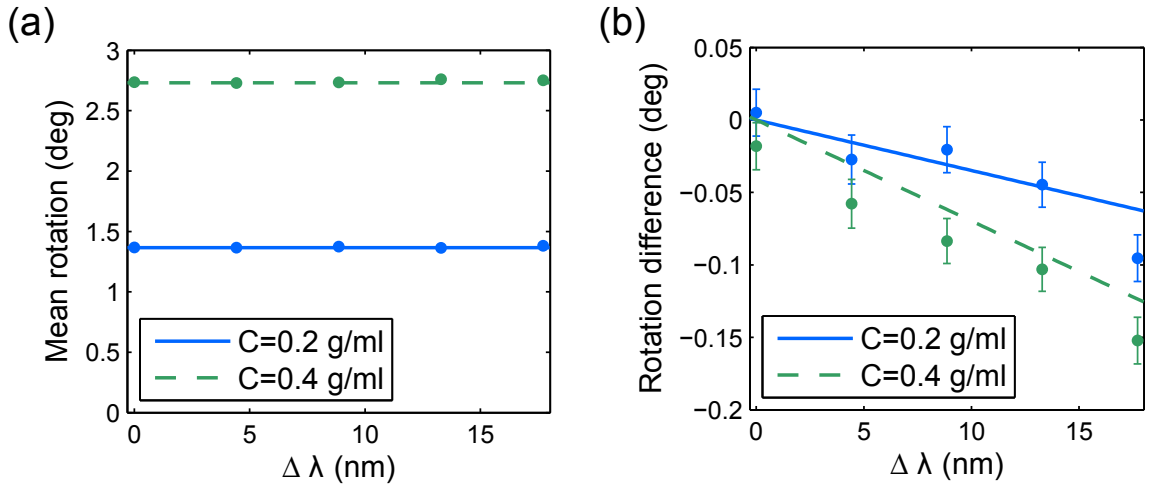

FIGURE 4.14: Comparison of experimental optical activity measurement results (data points) for sucrose with predictions by the model of Eq. (4.1) (lines). (a) depicts the mean rotations and (b) the rotation differences for wavelengths of $809.7 \pm \frac{\Delta\lambda}{2}$ nm. The results for a concentration of 0.4 g/ml are given by the dashed green line, and for 0.2 g/ml by the solid blue line. The error bars show $\pm$ one standard error of the mean, estimated from the standard deviation of the experimentally obtained angles. For the cases where the error bars are not clearly visible, the intervals are smaller than the markers. The measurements were taken at a temperature of 19°C.

The cause of this has not been established; one possibility might be an unintended difference between the conditions for the two paths in the cuvette. A difference in conditions could also explain the non-zero rotation difference at $\Delta\lambda = 0$, where a value of zero is expected, independently of the form optical activity takes as a function of wavelength. Nevertheless, the graphs show the expected overall behaviour, and the model notably has no free fitting parameters. The experiment constitutes a proof of principle for this type of measurement scheme. Fig. 4.14 (b) reveals that the difference between the optical activity at two wavelengths is very small, and the state $|\Psi\rangle$ is sensitive to this difference. Crucially, the signal of the comparatively large mean is separated from the small difference signal.

4.6 Discussion

To the best of my knowledge, this constitutes the first measurement of molecular optical activity that is based on quantum correlations. The speciality of this experiment is that the mean and difference of the optical rotation at two wavelengths are measured separately. As explained earlier, for the same resource of two photons, the quantum measurement schemes

ideally allow a factor of $\sqrt{2}$ enhancement in the precision of the mean or difference measurements, compared to using two separable linearly polarised photons. The difference measurement is especially interesting, because the ORD is often very small but reveals valuable information about the stereochemistry and molecular transition energies. A high precision measurement of the mean rotation can also be used for a number of applications, for instance to determine the concentration of a given optically active substance. In a sensing application where the goal is the detection of trace amounts of a substance, the measurement precision would determine the smallest concentration that can be distinguished from zero.

We will conclude this section by looking at how this experiment fits in the context of some relevant works from the literature. A distinctive feature of this experiment in comparison to previous polarisation-based quantum metrology experiments is the fact that it involves four modes in total, and the two photons are distinguishable so that they can probe two different polarisation-based MZIs.

Given that four modes are involved, one might ask how the above scheme is related to the joint estimation of multiple parameters, a problem that has been studied in some recent works [155–159]. Research on multi-parameter quantum metrology has revealed some intricacies in the extension of concepts from the comparatively well-understood single parameter estimation to the multi-parameter case. For instance, it has been shown that the simultaneous estimation of multiple parameters can lead to a better precision than if the same resources are distributed to estimate the parameters individually [156]. Furthermore, while a quantum Cramér-Rao bound can also be established for multi-parameter estimation, the possibility to saturate it depends on the commutativity of the measurement operators for the various parameters [144]. Another topic in multi-parameter estimation concerns the need for multimode entanglement. Generally, multi-parameter quantum metrology encompasses the study of unitary and nonunitary processes. Within unitary processes generated by commuting operators, one scenario relevant to imaging applications is the estimation of phases in a number of modes relative to one reference. A second scenario that is particularly relevant for comparison with the above optical activity study consists in the estimation of a set of pairwise relative phases. Ref. [159] provides an analysis of both scenarios. The authors propose quantum states without mode-entanglement that perform at least as well as other, multimode entangled states, suggesting that multimode entanglement is not a required resource for multi-parameter estimation tasks. This is consistent with the fact mentioned earlier that in our case, the states $|\Phi_{\text{in}}\rangle$ and $|\Psi_{\text{in}}\rangle$ yield no advantage for a joint estimation of both parameters $\overline{\alpha}$ and $\Delta\alpha$. Indeed, the goal in this chapter differs from that of multi-parameter quantum metrology. Although the use of two wavelengths introduces the rotation angles at the wavelengths, α_1 and α_2, as two potential parameters of interest, the experiment of this

chapter addresses single-parameter estimation tasks, albeit unusual ones. The more conventional single-parameter estimation task would be to determine the optical activity at only one of the two wavelengths. In that case, using a two-photon state as a resource, a polarisation NOON state or similar could simply be used at the wavelength in question, without probing the second wavelength at all. However, recasting the two parameters α_1 and α_2 in terms of multiwavelength sum and difference parameters $\overline{\alpha}$ and $\Delta\alpha$, the situation changes. As we have seen, quantum mechanics allows to directly access these multiwavelength parameters via the inter-mode entangled states $|\Phi_{\text{in}}\rangle$ and $|\Psi_{\text{in}}\rangle$, which are each sensitive to one of the two parameters. The proposed scheme provides an advantage when multiwavelength parameters are of interest individually rather than jointly, for example when only the derivative of the wavelength dependence is required.

The distinguishability of the photons in the experiment means that (superpositions of) Bell states are used as opposed to NOON states. In fact, the photons are distinguishable for two distinct reasons. The first is the separate paths containing one photon each. For the particular case of the input state $|\Phi_{\text{in}}\rangle$ and when $\Delta\lambda = 0$ so that the other source of distinguishability is eliminated, the scheme can be directly compared to the polarisation NOON type measurements with N=2, which can provide the same precision enhancement. Yet, a consequence of the individual paths for the photons is that the two photons are also detected separately. Hence, the typical problem of losing events due to both photons being incident on the same detector is completely avoided, even with four non-photon-number-resolving standard APDs. The second DOF by which the photons are distinguishable whenever $\Delta\lambda \neq 0$ is the wavelength. This DOF plays a very different role than the path, since the optical activity is wavelength-dependent and it is this dependence which is studied.

In [146], Bell *et al.* present another experiment where entangled photons with unequal wavelengths are used for phase measurement. Similarly to the optical activity measurement experiment above, the entangled multicolour biphoton state is created through a superposition of two events of a nonlinear optical process. In [146], it is realised by four-wave mixing in a photonic crystal fibre that the pump beam traverses in two directions. It allows the creation of path entanglement without the requirement of photon indistinguishability that is typical for schemes relying on HOM interference. The experiment bears some resemblance to the part of the above optical activity measurement in which $|\Phi\rangle$ is used to measure the mean rotation. By exploiting the distinguishability of the photons, both experiments avoid the issue of the two photons being incident on the same detector. However, some important differences also exist: Despite the photons being multicolour in both schemes, the role of the wavelength is different within the two experiments. In [146], the wavelength difference serves as a distinguishing feature that is useful for the implementation, rather than as an

important parameter for the phase itself. In contrast, in the optical activity experiment, the distinguishability is already achieved through the path DOF, and the actual wavelength-dependence of the phase is of interest. Moreover, the optical activity experiment adds the new element of measuring the difference between the phases at the two wavelengths.

The idea of using anti-correlated states for measuring a phase difference has been established in magnetometry, where macroscopic singlet states, which are insensitive to the homogeneous component of the magnetic field, can probe the spatial field gradient [144, 160]. Macroscopic singlet states in cold atomic ensembles have been proposed and implemented [161, 162]. The photonic counter-part has also been created successfully [163–165]. In Ref. [149], singlet states of photons produced in parametric down-conversion are proposed for the measurement of symmetry-breaking effects. The measurement scheme for the $|\Psi\rangle$ state from above (using a particular setting of the bias phase) is recovered from the proposed scheme in the limit of using only two photons. Singlet states possess the special property of being invariant to global rotations about any axis. As an alternative, the phase difference measurement from above could also be generalised to $N > 2$ photons using the state $\frac{1}{\sqrt{2}}\left(|\frac{N}{2},0,0,\frac{N}{2}\rangle + \mathrm{e}^{i\alpha_0}|0,\frac{N}{2},\frac{N}{2},0\rangle\right)$, where $|a,b,c,d\rangle$ denotes a state consisting of a photons with wavelength λ_1 and polarisation R, b photons with wavelength λ_1 and polarisation L, c photons with wavelength λ_2 and polarisation R, and d photons with wavelength λ_2 and polarisation L. The state $|\Psi\rangle$ is also a member of this family of states, which is constructed as a superposition of the eigenstates corresponding to the minimum and maximum eigenvalues of the generator of the unitary transformation [21, 128, 166]. Similar states have also been proposed in the context of quantum clock synchronisation [167, 168].

Chapter 5

Conclusions and Outlook

This thesis combines experimental, analytic, and numerical work in the fields of nanophotonics and quantum optics. The common motivation behind the individual projects is the goal of optical quantum metrology on nanoscatterers. An understanding of light-matter interaction for a given system of interest, and a suitable nonclassical light source form the prerequisites for the goal.

To this end, I have studied the interaction of classical light with a nanostructure that consists of a (sub-)wavelength hole in a metal film. Furthermore, I have shown ways of manipulating and measuring the wavefunction of photon pairs produced through SPDC. Finally, I have demonstrated how photon pairs can be used to measure the interaction of light with chiral molecules.

5.1 Summary of key contributions of this thesis to the fields of research

Chapter 2 presents two experiments on the interaction of classical light with nanoholes.

A description of the polarisation DOF of light in terms of helicity is very useful, since a symmetry can be associated with this observable. Section 2.3 demonstrates how helicity can be used and controlled in nanophotonics experiments, even though in the nonparaxial regime its relationship with polarisation is subtle. Circular nanoapertures in metal make up the scatterers for this experiment. The scaling of the power transmitted through nanoholes as a function of the hole size has been studied by the nanophotonics community. The experiment adds to that body of work by establishing that the scaling of the transmitted power is different for the two output helicities, when a Gaussian beam is incident on the nanohole in a helicity eigenstate. The experiment is published in Ref. [31].

In Section 2.4, a simple nanopositioning technique that enables the identification of a reference position is proposed and experimentally implemented using the same nanostructure. As it only relies on cylindrical symmetry of the probe field and the scatterer, it can also be adapted to other systems besides nanoapertures.

Chapter 3 contains analytic and numerical results on the control of the spectrotemporal properties of photon pairs produced in SPDC.

Section 3.2 shows a way of manipulating the time delay between photons produced in type-II SPDC through the crystal position, and the underlying mechanism is explained. The results have immediate implications for experiments in which photon pairs to be used for quantum interference are created via type-II SPDC, particularly in a collinear configuration. The work is published in Ref. [2].

In Section 3.3 a simple, new method is proposed that allows to measure the complex spectral wavefunction of biphotons produced in type-II SPDC. Since the wavefunction contains the complete information about the spectrotemporal DOF, it admits the calculation of any observable related to this DOF. The probability distribution of time delays between the photons is of particular practical interest, because it is difficult to measure experimentally. The content of this section is published in Ref. [3].

Chapter 4 presents a quantum metrology experiment in which entangled photon pairs are used for the first time to measure natural optical activity. The special feature of this experiment is that nondegenerate photons provide information about different quantities of interest: One type of entangled state, with correlated polarisations, is sensitive to the mean optical activity, while another type with anticorrelated polarisations gives direct access to the ORD.

5.2 Outlook

Striving for speed, compactness, and efficiency, technology is reducing the size of devices such as sensors and transistors to smaller and smaller scales. This miniaturisation calls for new tools to control and measure structures at the nanoscale. The intersection of nanophotonics and quantum optics is a promising space for the development of such tools, because it allows to combine nonclassical resources, such as single photons or entangled photon states, with the understanding of tightly confined modes offered by nanophotonics. One of the tasks that can benefit from quantum resources is measurement. This thesis pursues the goal of performing quantum-enhanced measurements of nanostructures by exploiting the interplay

between nanophotonics and quantum technologies. The work presented in the thesis makes several contributions towards this larger goal.

First of all, the nanohole experiments of Chapter 2 demonstrate a way to exploit symmetries in nanoscattering. This is particularly advantageous when no analytic model for the light-matter interaction is known, a common case in nanoscattering. Although classical light was employed in the experiments, the approach of basing the experimental design on symmetries is equally applicable when using nonclassical light.

Secondly, some tools for engineering biphoton states are developed in Chapter 3. The ability to tailor and control quantum states of light is a key requirement for their use within quantum metrology. Spectrotemporal properties, which are the focus of the chapter, play a role for applications that involve energy transitions or exhibit a dependence on the photon timings.

Lastly, the goal of quantum measurements with nanoscatterers is approached more directly in Chapter 4. The quantum metrology experiment presented there involves nanoscatterers on the smallest scale, namely molecules acting as the scatterers. The light-matter interaction is used to reveal molecular properties exhibited through the refractive index of the medium.

In the future it would be interesting to perform quantum metrology experiments on larger scatterers, for example complex biomolecules or nanostructures made of dielectrics or metals. This could better motivate restricting the probe power and would allow tapping into more of the typical features of nanophotonics explained in Section 1.1.1. The measurements could again be of optical activity, but other aspects of the light-matter interaction could also be probed. The transition to larger scatterers could be realised via two routes:
1. In special systems, for instance with metamaterials, it may be possible to have light interacting with larger structures in such a way that a simple effective interaction is maintained. A unitary transformation, through which the parameter of interest is encoded in the probe state as a phase, would then permit the use of conventional, well established tools of quantum metrology [21, 166].
2. Generally, however, the light-matter interaction can be more complex, so that no mapping onto well-studied problems in quantum metrology is obvious. This poses the question of how the parameter of interest in a given system can be measured. The task can further be complicated by losses that are often present in nanophotonics experiments (examples can be found in [48] and [5, Chapter 12]).

With regard to the choice of probe light, although the experiment of Chapter 4 strictly speaking does not make use of conventional NOON states, it has some challenges in common with NOON-type quantum metrology experiments: The enhancement of the measurement

precision is on the one hand limited by difficulties in creating the required sort of entangled state with a high photon number, and on the other hand degraded by losses. Already today, the losses could be significantly reduced with different equipment, such as anti-reflection coatings and high-efficiency detectors [169]. The preparation of useful nonclassical states is an important challenge [20, Sec. 13.5.2], [136, 141, 170–173]. The problem of loss is also being recognised and tackled in the research community (see for example [21] and references within, as well as [174–180]).

Despite such challenges, combining elements of quantum metrology and nanophotonics might open up exciting new possibilities. Real-world metrological applications could benefit from jointly leveraging phenomena of the two fields, for instance the field enhancement of nanophotonics on the one hand, and the fast state evolution of quantum metrology on the other. A further interesting path might emerge from optical properties that are not accessible in nature but attainable through the design of metamaterials. Could these novel properties be put to use in metrological applications? I am curious what new ideas the connection of nanophotonics with quantum metrology will generate.

The results of this thesis also admit some more immediate follow-up studies that are not explicitly related to the idea of quantum metrology for nanoscatterers.

In my opinion, an analysis in terms of helicity and total angular momentum is especially worthwhile in the set of optics experiments that would otherwise typically be considered in terms of spin and orbital angular momenta. The main reason for this is the predictive power due to the connection with symmetries. In the experiment of Section 2.3, helicity conversion is measured for a case where light interacts with matter that lacks duality symmetry. In the case of a dual scatterer, theory predicts that independently of its geometry, no conversion occurs. This, in fact, is a striking example for the difference in predictive power of the frameworks. Hence, an experimental observation of such helicity preservation would constitute a nice follow-up of the work from Section 2.3. It could in principle be done with a similar experimental set-up; the main challenge would be procuring a dual scatterer, as most naturally occurring materials are not dual.

There is also a possibility for extensions related to Chapter 3. The effect explained in Section 3.2 is rooted in spatio-temporal correlations within the biphoton wavefunction. The primary consequence of moving the crystal is a shift of the time delay distribution. However, the results of Chapter 3 point towards a possibility of shaping the temporal wavefunction in a more comprehensive manner. It could be achieved via more general spatial manipulations, for instance with an SLM, which can again affect the temporal properties due to spatio-temporal correlations.

In the optical activity study presented in Chapter 4, measuring the difference between two wavelengths was of particular interest. However, the same method can also be used for other differential measurements. As further examples involving optical activity, the experimental set-up can be adapted to compare the concentrations or enantiomeric purities of two solutions by choosing the photons to be at the same wavelength and simply performing the differential measurement across two different solutions. Of course, the differential measurement approach is by no means limited to optical activity measurements. Such measurements could also be used more generally to compare the relative phase difference between two pairs of modes, or to estimate derivatives of parameters that affect the relative phase with respect to the relevant DOF by which the two pairs of modes differ, for example to estimate some types of spatial gradients.

Appendix A

Nanofabrication

The samples used for the experiments of Chapter 2 were fabricated by Dr. Alexander Minovich at the ACT Node of the Australian National Fabrication Facilities. Later on, I made further nanoaperture samples at the Central Analytical Research Facility of Queensland University of Technology (QUT) with the help of Michael Larkins and Dr. Kristy Vernon. Here I provide details about the fabrication process at QUT to give the reader an idea about what is involved in the creation of such nanoaperture samples.

The final nanohole sample is obtained in three main steps: A suitable glass substrate is required, then a gold film is deposited on the substrate, and finally the nanoapertures are milled in the gold.

A.1 Glass substrate

Given that the gold layer containing the nanoapertures should have a thickness of only 100-200 nm, a transparent substrate is used to support the gold film. This substrate is the object the nanofabrication starts with. We chose to make samples on two different glass substrates, a microscope coverslip (made from colourless borosilicate glass (D 263) with a thickness of 0.15 ± 0.02 mm) and a microscope slide (alkaline earth boro-aluminosilicate glass with a thickness of 1.10 ± 0.03 mm). The main difference between the two, the thickness, is the basis of their respective advantages and disadvantages. On the one hand, the thicker microscope slide is less fragile and therefore easier to handle. On the other hand, the thinner coverslip can allow imaging of the gold film using microscope objectives with higher NA, as high NA objectives tend to have shorter working distances so that they need to be closer to the gold. As required, the substrates were cleaned following a four-step procedure:

1. Using tweezers, the substrate is immersed in a solution of detergent in water for a duration of 10 s.
2. Next, it is held in a bath of acetone for 2 minutes.
3. Then the sample is quickly rinsed with ethanol.
4. Finally, it is dried using compressed nitrogen from a nitrogen gun.

A.2 Gold film

Once the substrate is ready, the gold film is created on top of it from bulk gold such as commercially available gold string. A very thin ($\sim$ 2 nm) layer of chromium may be used for better adhesion between the gold and glass, but it was not done in our case. The gold film deposition can be achieved via sputter coating or thermal evaporation under high vacuum. The choice of method has an impact on the purity, surface quality, and structure of the gold film. Ideally, one would like a smooth film. The specifics, in turn, influence the geometrical precision of the holes that are later milled into the gold: Irregularities and crystalline boundaries behave differently in the milling process, which may lead to a deviation from the design structures. Examples of such defects are shown in Fig. A.1. The details of the gold film also affect the interaction of light with the sample. Simple calculations and simulations that model multilayer structures with piecewise constant permittivities as obtained from tables for bulk materials generally do not account for such details.

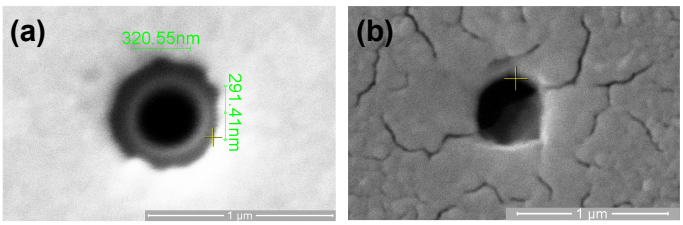

FIGURE A.1: SEM images of nanoholes with erratic shapes. In both cases, the outline of the hole, which is meant to be circular, contains irregularities. In addition, the hole walls in (a) are not vertical as intended. In (b) imperfections in the surface of the gold film are visible.

For our gold films, we used vacuum deposition with a thermal evaporator (Emitech K975X), which typically results in a better film purity than sputter coating [181, Sec. 18.3.2.1]. However, we encountered some difficulties related to the film thickness. The film thickness monitor contained in the device, which is designed to assist with achieving the desired value, was not operational at the time of use. Without the monitor, it could

still be possible to control the film thickness after a thorough calibration that relates the specific settings (amount of gold used, device settings, coating times) with film thicknesses. Yet, uncertainties in the calibration led to uncertainties in the film thickness. The film on the coverslip has a thickness of $\sim$ 120 nm, and the one on the microscope slide is $\sim$ 130 nm thick.

Ellipsometry is a very useful tool for characterising multilayer structures. An ellipsometer is a device that measures the polarisation-dependent scattering of light from planar surfaces and multilayer samples, potentially as a function of the scattering angle and wavelength [182]. The physical layout of the apparatus is illustrated in Fig. A.2. The thickness of a layer can be estimated with an ellipsometer based on the interference between light that is scattered from the lower and upper surfaces of the layer. However, this works only for thin films (approximately $<$ 100 nm thickness) in the case of metal samples. The reason for this is that absorption takes place, which results in a decrease of the amplitude of light scattered from the lower surface.

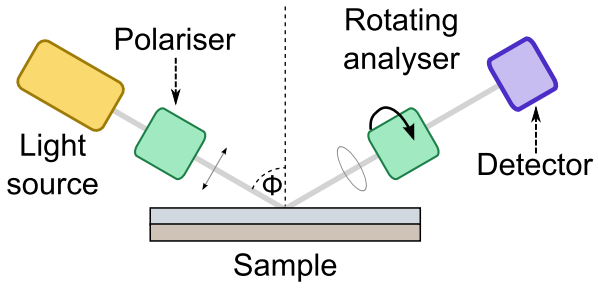

Figure A.2: Schematic of an ellipsometer. Polarised light is reflected off a planar sample and the polarisation of the reflected light is analysed. The angle of incidence, Φ, and wavelength of the light may be varied.

We performed ellipsometric measurements on thinner gold films (thickness of 10-20 nm), and the results revealed a further complication to the calibration of our thermally evaporative film deposition, namely that the film thickness strongly depended on the position of the sample within the chamber. The maximum relative variation of film thickness we measured for different positions was as much as $\sim$ 80%. Ellipsometric measurements can also be used to determine the complex permittivities of the sample materials. Knowledge of these permittivities is useful for any subsequent modelling of light interacting with the fabricated sample. Fig. A.3 shows the complex permittivities as a function of wavelength that we obtained for our glass (a) and gold (b) materials through ellipsometric measurements. This is plotted alongside reference values from the literature which could otherwise have been

used for modelling purposes. For the case of glass, the results obtained for the coverslip and microscope slide are very similar and also match the reference values closely. On the other hand, discrepancies between experimental permittivities and the reference values are evident for gold. The reference values for the real part of the permittivity are mostly within one standard deviation of the experimental values, but there is a significant deviation of the experimentally obtained imaginary part compared to the reference values at wavelengths above 500 nm. This might be due to the polycrystalline structure of the gold.

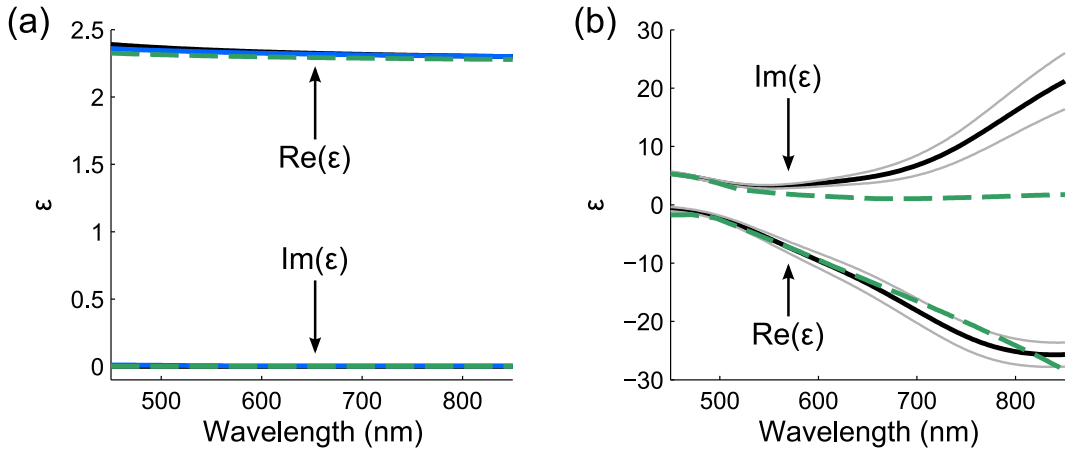

FIGURE A.3: Comparison between experimentally obtained wavelength-dependent complex permittivities and reference values for glass (a) and gold (b). In (a) the solid curves are the experimental permittivities for the coverslip (black) and the microscope slide (blue), while the dashed green line is the permittivity for Schott borosilicate crown (N-BK7) [183]. (b) shows the mean experimental permittivities of gold in black solid lines and an interval of $\pm\sigma$ is indicated by the grey lines, as obtained from four independent measurements. Again, the green dashed lines show a reference permittivity, this time values for gold from [184].

A.3 Nanoaperture milling

The final step is milling the nanoholes into the gold film with an FIB machine. We used an FEI Quanta 200 3D, a dual beam system that allows to mill structures using an ion beam, and to image the sample using either ion or electron beams [185, Chapter 12]. All these applications make use of beams of charged particles, which can be manipulated with electric and magnetic fields. The electrons are released through field emission from a tungsten tip, and the gallium ions are obtained from a liquid metal ion source with a tungsten needle, where the large electric field results in ionisation and finally also field emission. These primary electrons or ions are accelerated and focused on the sample. Electrons excite the atoms near the sample surface, which then emit secondary electrons that are detected. When

an ion beam is used, material is sputtered during the interaction of the ions with the sample. For imaging applications, a low ion beam current is used to reduce the amount of sputtering, but the imaged section is nevertheless gradually milled away with increasing imaging time. The dark rectangular regions around some of the holes in the electron beam images of both (a) and (b) in Fig. A.5 are due to milling during ion beam imaging. The properties visible through ion beam imaging are different from those that show up in an electron beam image [185, Fig. 7.8]. An example of an ion beam image can be seen in Fig. A.4. The pattern in the gold might appear like surface roughness at first, but it is actually due the differing orientations of crystalline domains.

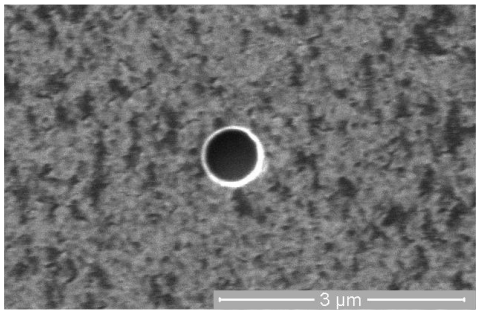

Figure A.4: Ion beam image of a circular nanoaperture. The pattern of the gold film does not show surface roughness but different orientations of the crystalline domains.

A higher beam current is chosen for lithographic applications, i.e. to deliberately pattern the sample. This is how the nanoholes are created. The preparatory steps to get the machine ready for milling include setting up the focus of the beams, and this influences the quality of the final nanostructures. For example, if astigmatism is not properly corrected, a hole that is designed to be round may turn out elliptical. It is also important to find the right combination of beam current and dwell time that leads to the correct milling depth. Insufficient depth means that the holes do not fully penetrate the gold film, while overmilling can result in an undesired shape, for example due to material redepositing at the edge of the hole [185, Sec. 2.4]. The milling settings also influence the shape of the hole walls. The aim for our nanosamples was cylindrical rather than the conical holes (compare Fig. A.6 (a) and (b) with Fig. A.1 (a)).

As the holes are very small, it can actually be quite difficult to locate them on the sample at the beginning of optical experiments. The challenge in the search for the holes is the following: When illuminating a large portion of the sample, very little light is transmitted through the nanoapertures, but the more tightly the light is focused, the smaller the spot. One way to simplify the search would be to have them close to the edge of the sample.

However, this is usually not very practical since it would restrict the options for how the sample can be mounted later on. To help with navigation on the sample, it is therefore convenient to create the nanoholes in the vicinity of some easy to find marker. One option is to use a scratch in the gold, but this has the disadvantage of the scratch potentially affecting the gold film in an extended region. An alternative option is to mill a large hole as a marker (see Fig. A.5 (a) for an example), which requires time but does not disturb the gold film around the marker.

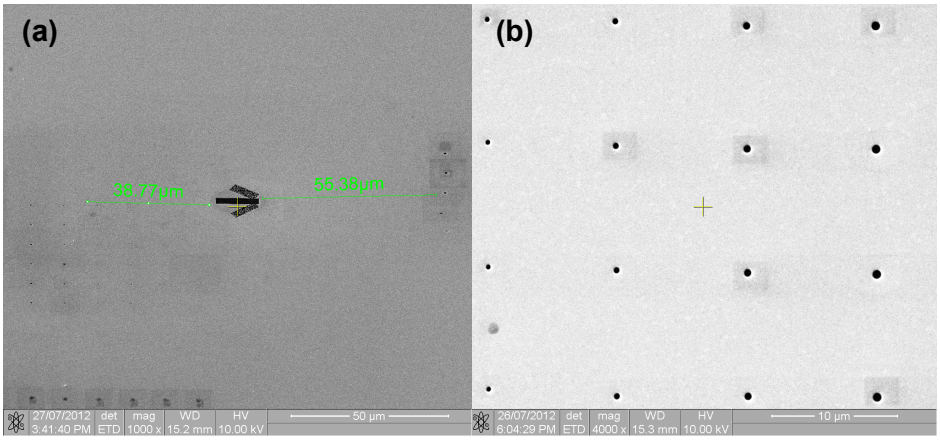

FIGURE A.5: SEM images of large sections of two different samples. In (a) an arrow milled into the sample, which serves as a marker, is visible, along with parts of three nanohole arrays. (b) shows a part of one nanohole array with holes of increasing size towards the right.

We milled a variety of different nanoholes, namely circular, elliptical, and rectangular nanoapertures with cross-sections ranging between 200 nm and 750 nm. For the ellipses and rectangular holes, aspect ratios between 0.3 and 1 were used. A selection of examples is shown in Fig. A.6.

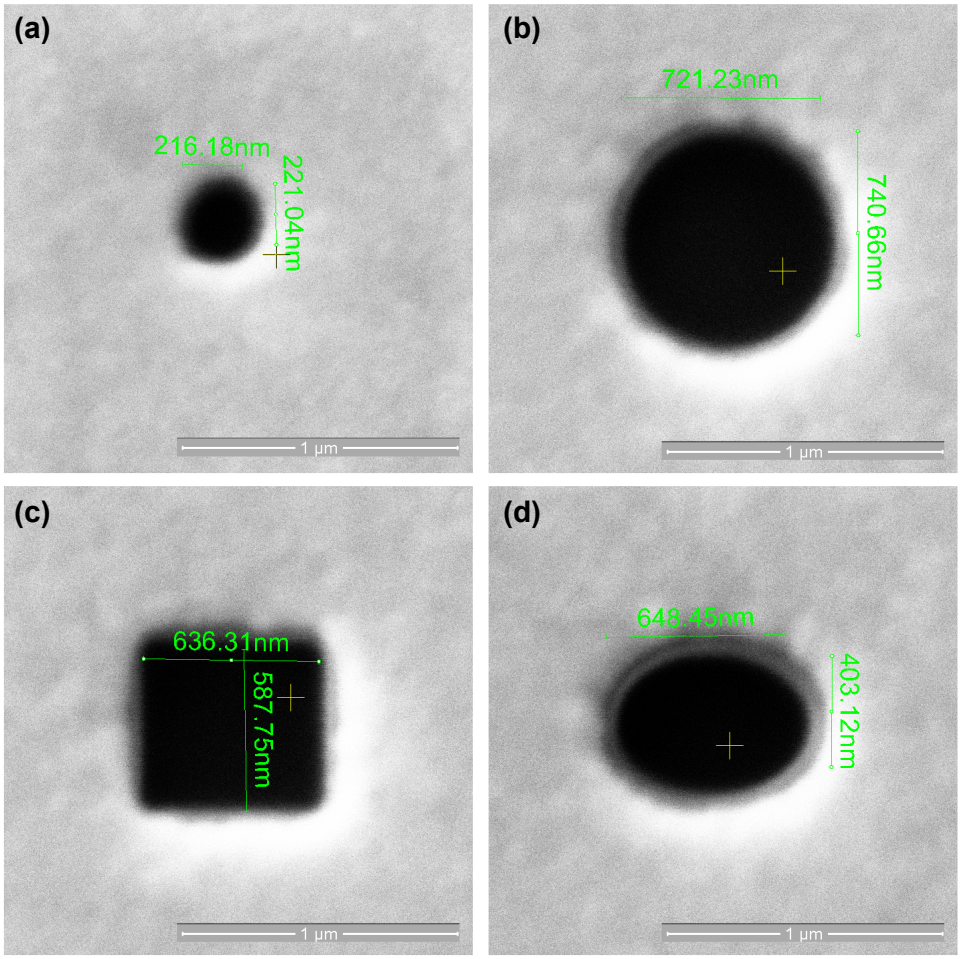

Figure A.6: SEM images of four example holes, illustrating the range of sizes and shapes created. (a) and (b) are circular holes of different sizes, while (c) shows a rectangular and (d) an elliptical hole. The scale is the same in all subfigures, with the length of 1 μm indicated by the insets. The overlaid measurements were performed with the FIB machine and provide information about the hole sizes.

Appendix B

Details for Chapter 2

Rotational symmetry of scattered light when a field in a superposition of $J_z = 1, \Lambda = 1$ and $J_z = -1, \Lambda = -1$ impinges on a cylindrically symmetric object

This Appendix considers an electromagnetic field consisting of a superposition of $J_z = 1, \Lambda = 1$ and $J_z = -1, \Lambda = -1$, that impinges on a cylindrically symmetric scatterer, such that the symmetry axis of the scatterer and incident electromagnetic modes coincide. In particular, we will see what kind of rotational symmetry is obtained when helicity modes of the scattered field are imaged, even in the case of imperfect helicity projection. Relating this to the nanoaperture experiment of Section 2.4, the analysis corresponds to a case of perfect alignment, but allows for imperfections in the polarisation preparation and analysis. In the nanoaperture experiment, the incident light field consists of predominantly $J_z = 1, \Lambda = 1$ with only a very small component of $J_z = -1, \Lambda = -1$, but the following analysis is valid for a general superposition of the two modes.

Let us first treat the two input modes separately, since each one forms a cylindrically symmetric system with the scatterer. A superposition of the resulting modes will be constructed at the end. We will begin with the incident mode $J_z = 1, \Lambda = 1$. The z-component of the angular momentum is conserved due to cylindrical symmetry, so it is clear that both incident field and transmitted field should be invariant to rotation about the z-axis, except for a phase factor. In contrast to J_z, Λ is not conserved, so that the scattered field originating from the $J_z = 1, \Lambda = 1$ mode contains two modes: $J_z = 1, \Lambda = 1$ and $J_z = 1, \Lambda = -1$. Considering these two modes of well-defined helicity, after collimation, the transmitted field with unchanged helicity can be written in terms of the functions $\mathbf{D}_{1p_z}$ from Eq. (1.4) and has

no azimuthal dependence, while the transmitted mode with opposite helicity can be written in terms of $\mathbf{C}_{1\mathrm{p}_z}$ of Eq. (1.3) and has an azimuthal dependence of $\exp(i2\theta)$ (The azimuthal dependence here refers to the scalar component of the field). The central node of the beam with opposite helicity (see Fig. 2.4 (b) for the case of the nanoaperture) is then an optical vortex of charge two. Both of these factors of azimuthal dependence, 1 and $\exp(i2\theta)$, are invariant to rotations by π about the z-axis. Because of the unit vectors for LC and RC polarisation, such a transformation on the full vectorial field results in an overall phase factor of -1 in the case of both helicities. This common property of the two modes is of course consistent with the fact that both fulfil $J_z = 1$.

Now, the modes originating from the incident mode with $J_z = -1, \Lambda = -1$ can be treated in an analogous way, where the same argument concerning rotations by π can be made for the two scattered modes $J_z = -1, \Lambda = -1$, $J_z = -1, \Lambda = +1$. This means that in fact, all four modes contained in the scattered field share the factor of -1 after an angular momentum preserving transformation. Imperfections of the projective measurement will result in mixing of the four modes. However, the essential result is that due to the common two-fold rotational symmetry of all the modes, the intensity distribution of the measured helicity mode is also invariant to a rotation by π.

Appendix C

Details for Chapter 3

C.1 Numerical modelling

In the numerical calculation of the mode function the refractive indices are modelled by Sellmeier equations for KTP that depend on the frequency, polarisation, and propagation direction of the light, as well as the crystal temperature [186]. A temperature dependence of the poling period, which is caused by thermal expansion of the crystal, is also incorporated based on coefficients from [187], although this has a comparatively small effect.
In the calculation of the longitudinal wavevectors, I make the approximation of using $k_{zm} = \sqrt{(k(\omega_m, T))^2 - |\mathbf{q}_m|^2}$ with $k(\omega_m, T) = n(\omega_m, T)\frac{\omega_m}{c}$, where $n(\omega_m, T)$ is calculated for the propagation direction z.

C.2 SPDC state

For the biphoton wavefunction at the crystal exit facet

$$|\Psi\rangle = \int \mathrm{d}\mathbf{q}_s \mathrm{d}\mathbf{q}_i \mathrm{d}\omega_s \; \Phi_{\text{full}}(\mathbf{q}_s, \mathbf{q}_i, \omega_s, \omega_i; T, \omega_p) \hat{a}_s^\dagger(\mathbf{q}_s, \omega_s) \hat{a}_i^\dagger(\mathbf{q}_i, \omega_i)|0\rangle \tag{C.1}$$

is used, where the function $\Phi_{\text{full}}(\mathbf{q}_s, \mathbf{q}_i, \omega_s, \omega_i; T, \omega_p)$ is the biphoton mode function

$$\begin{aligned} \Phi_{\text{full}}(\mathbf{q}_s, \mathbf{q}_i, \omega_s, \omega_i; T, \omega_p) \;\propto\; & \operatorname{sinc}\left(\frac{\Delta k_z(\mathbf{q}_s, \mathbf{q}_i, \omega_s, \omega_i; T, \omega_p) L}{2}\right) \exp\left(-\frac{w_p^2 |\mathbf{q}_s + \mathbf{q}_i|^2}{4}\right) \\ & \times \exp\left(i \; k_{zp}(\mathbf{q}_s + \mathbf{q}_i, \omega_s + \omega_i, T)(z_c - z_{foc}(z_c))\right) \\ & \times \exp\left(i \; (k_{zs}(\mathbf{q}_s, \omega_s, T) + k_{zi}(\mathbf{q}_i, \omega_i, T))(L/2)\right). \end{aligned} \tag{C.2}$$

This is equivalent to Eqs. (3.1) and (3.2) of Section 3.2 and the definitions of the variables are provided there; the only difference is that here the dependence on ω_p is explicitly incorporated. In Section 3.2 it is held constant and therefore omitted.

After projection into spatial modes G_s and G_i, the mode function becomes

$$\Phi\left(\omega_s, \omega_i; T, \omega_p\right) \equiv \int\int \mathrm{d}\mathbf{q}_s \mathrm{d}\mathbf{q}_i \; \Phi_{\mathrm{full}}(\mathbf{q}_s, \mathbf{q}_i, \omega_s, \omega_i; T, \omega_p) \; G_s^*(\mathbf{q}_s) G_i^*(\mathbf{q}_i). \tag{C.3}$$

Detection modes

Laguerre Gaussian (LG) modes are used as detection modes. This encompasses the typical Gaussian, appropriate for the simple use of a SMF as in Section 3.2, but also higher order modes, the projection into which can be achieved by the use of holograms, SLMs, or q-plates before the fibre coupling. The Laguerre Gaussian modes are determined by the parameters l, q, w, which are the vortex charge, the radial index related to the number of radial nodes, and the beam waist, respectively. They are defined as

$$\begin{aligned}
G(\mathbf{q}) &= LG_{l,q}\left(k_r, \phi_k; w_m\right) = f_l\left(\phi_k\right) \; f_{l,q}\left(k_r\right), \\
f_l\left(\phi_k\right) &= \exp\left(il\phi_k\right) \\
f_{l,q}\left(k_r\right) &= \sqrt{\frac{w_m^2 q!}{2\pi\left(|l|+q\right)!}} \left(\frac{w_m k_r}{\sqrt{2}}\right)^{|l|} L_q^{|l|}\left(\frac{w_m^2 k_r^2}{2}\right) \exp\left(-\frac{w_m^2 k_r^2}{4}\right) \exp\left(i\left(q - \frac{|l|}{2}\right)\pi\right).
\end{aligned}$$

Here, $L_q^{|l|}\left(x\right)$ is the associated Laguerre polynomial. The polarisation is omitted, but is determined by the projection modes applying to either the signal or idler photon. The momenta in cylindrical coordinates are related to the Cartesian ones in the usual way:

$$\begin{aligned}
\phi_k &= \mathrm{Arg}\left(q_x + iq_y\right) \\
k_r &= \sqrt{q_x^2 + q_y^2}.
\end{aligned}$$

Section 3.2 explains how the effect of a longitudinal displacement of the crystal on the detection modes is modelled.

C.3 Taylor approximations

C.3.1 Taylor expansion of longitudinal wavevectors

A multivariate Taylor expansion of the longitudinal wavevector, k_{zm}, about $\omega_m = \omega_{0m}$, $T = T_0$, and $\mathbf{q}_m = \mathbf{0}$ up to the first non-zero order in each variable is

$$\begin{aligned} k_{zm}(\mathbf{q}_m, \omega_m, T) &\approx k_m(\omega_{0m}, T_0) + (\omega_m - \omega_{0m}) \frac{\partial k_m}{\partial \omega} \\ &\quad + (T - T_0) \left(\frac{\partial k_m}{\partial T} \right) - \frac{|\mathbf{q}_m|^2}{2k_m(\omega_{0m}, T_0)}. \end{aligned} \tag{C.4}$$

All derivatives are evaluated at the reference settings. The wavenumber is $k_m(\omega_m, T) = k_{zm}(\mathbf{0}, \omega_m, T)$, $\frac{\partial k_m}{\partial \omega}$ is the inverse group velocity, and $\frac{\partial k_m}{\partial T} = \frac{\omega_{0m}}{c} \frac{\partial n_m}{\partial T}$.

C.3.2 Taylor expansion of the longitudinal wavevector mismatch

Since $\Delta k_z L/2$ is the argument of the sinc function in Eq. (3.2), down-conversion is most efficient for $\Delta k_z = 0$. T_0 is defined as the temperature at which collinear down-conversion takes place efficiently at the reference frequencies ω_{0s} and ω_{0i}, so that

$$k_p(\omega_{0s} + \omega_{0i}, T_0) - k_s(\omega_{0s}, T_0) - k_i(\omega_{0i}, T_0) - \frac{2\pi}{\Lambda(T_0)} = 0. \tag{C.5}$$

The poling period, Λ, depends on the crystal temperature due to the thermal expansion of the nonlinear crystal. Using Eqs. ($C.4$) and ($C.5$), a multivariate Taylor expansion of the longitudinal wave vector mismatch, Δk_z, about $\omega_s = \omega_{0s}$, $\omega_i = \omega_{0i}$, $T = T_0$, and $\mathbf{q}_s = \mathbf{q}_i = \mathbf{0}$ up to the first non-zero order in each variable is

$$\begin{aligned} \Delta k_z &\approx (\omega_s - \omega_{0s} + \omega_i - \omega_{0i}) \frac{\partial k_p}{\partial \omega} - (\omega_s - \omega_{0s}) \frac{\partial k_s}{\partial \omega} - (\omega_i - \omega_{0i}) \frac{\partial k_i}{\partial \omega} \\ &\quad + (T - T_0) \left(\frac{\partial k_p}{\partial T} - \frac{\partial k_s}{\partial T} - \frac{\partial k_i}{\partial T} + \frac{2\pi}{(\Lambda(T_0))^2} \frac{\partial \Lambda}{\partial T} \right) \\ &\quad - \frac{|\mathbf{q}_s + \mathbf{q}_i|^2}{2k_p(\omega_{0s} + \omega_{0i}, T_0)} + \frac{|\mathbf{q}_s|^2}{2k_s(\omega_{0s}, T_0)} + \frac{|\mathbf{q}_i|^2}{2k_i(\omega_{0i}, T_0)}. \end{aligned} \tag{C.6}$$

Since the pump frequency is fixed in Section 3.2, the first term does not contribute there.

C.4 Symmetrised mode function after Taylor approximation

First, some definitions are introduced that will be useful later on:

$$
\begin{aligned}
X_T &\equiv \left(\frac{\partial k_p}{\partial T} - \frac{\partial k_s}{\partial T} - \frac{\partial k_i}{\partial T} + \frac{2\pi}{\left(\Lambda\left(T_0\right)\right)^2}\frac{\partial \Lambda}{\partial T}\right) \\
X_{T2} &\equiv \left(\frac{\partial k_s}{\partial T} + \frac{\partial k_i}{\partial T}\right) \\
c_t &\equiv -\frac{X_T}{\left(\frac{\partial k_s}{\partial \omega} - \frac{\partial k_i}{\partial \omega}\right)} \\
X_{q2}\left(\mathbf{q}_s, \mathbf{q}_i\right) &\equiv -\frac{|\mathbf{q}_s|^2}{2k_s(\omega_{0s}, T_0)} - \frac{|\mathbf{q}_i|^2}{2k_i(\omega_{0i}, T_0)} \\
X_{q3}\left(\mathbf{q}_s, \mathbf{q}_i\right) &\equiv -\frac{|\mathbf{q}_s + \mathbf{q}_i|^2}{2k_p(\omega_{0s} + \omega_{0i}, T_0)} + \frac{|\mathbf{q}_s|^2}{2k_s(\omega_{0s}, T_0)} + \frac{|\mathbf{q}_i|^2}{2k_i(\omega_{0i}, T_0)} \\
X_\omega &\equiv \left(\frac{\partial k_p}{\partial \omega} - \frac{\partial k_s}{2\partial \omega} - \frac{\partial k_i}{2\partial \omega}\right) \\
c_{\omega p} &\equiv -\frac{X_\omega}{\left(\frac{\partial k_s}{\partial \omega} - \frac{\partial k_i}{\partial \omega}\right)}.
\end{aligned}
$$

Now, in order to establish the relationship between a change in crystal temperature or pump wavelength and the frequencies, the wavefunction is written explicitly in the symmetrised form that is intrinsic to the quantum interference process. Let $\Delta\omega_p \equiv \omega_1 + \omega_2 - \omega_{0s} - \omega_{0i}$ and $\Omega \equiv \omega_1 - \frac{\omega_{0s}+\omega_{0i}}{2} - \frac{\Delta\omega_p}{2}$. With these definitions and change of variables, after some work one can obtain

$$
\begin{aligned}
\Phi \quad & (\omega_1, \omega_2; T = T_0 + \Delta T, \omega_p = \omega_{p0} + \Delta\omega_p)\, \Phi^* (\omega_2, \omega_1; T = T_0 + \Delta T, \omega_p = \omega_{p0} + \Delta\omega_p) \\
\approx \quad & \Phi (\omega_1 + \Delta T c_t + \Delta\omega_p c_{\omega p}, \omega_2 - \Delta T c_t - \Delta\omega_p c_{\omega p}; T_0, \omega_{0p}) \\
& \times \Phi^* (\omega_2 + \Delta T c_t + \Delta\omega_p c_{\omega p}, \omega_1 - \Delta T c_t - \Delta\omega_p c_{\omega p}; T_0, \omega_{0p}) \\
\propto \quad & \exp\left(i \left(2\Omega \left(\frac{\partial k_s}{\partial \omega} - \frac{\partial k_i}{\partial \omega} \right) \right) \left(\frac{L}{2} \right) \right) \\
& \times \int\int \mathrm{d}\mathbf{q}_{s'} \mathrm{d}\mathbf{q}_{i'} G_s^*(\mathbf{q}_{s'}) G_i^*(\mathbf{q}_{i'}) S_P(\mathbf{q}_{s'} + \mathbf{q}_{i'}) \\
& \times \exp\left(i \left(X_{q2} (\mathbf{q}_{s'}, \mathbf{q}_{i'}) \right) \left(z_c - z_{foc} (z_c) + \frac{L}{2} \right) \right) \\
& \times \mathrm{sinc}\left(\frac{L}{2} \left(\left(\frac{\partial k_s}{\partial \omega} - \frac{\partial k_i}{\partial \omega} \right) \left(-\Omega + \frac{\omega_{0s} - \omega_{0i}}{2} - \Delta T c_t - \Delta\omega_p c_{\omega p} \right) + X_{q3} (\mathbf{q}_{s'}, \mathbf{q}_{i'}) \right) \right) \\
& \times \int\int \mathrm{d}\mathbf{q}_{s''} \mathrm{d}\mathbf{q}_{i''} G_s(\mathbf{q}_{s''}) G_i(\mathbf{q}_{i''}) S_P^*(\mathbf{q}_{s''} + \mathbf{q}_{i''}) \\
& \exp\left(-i \left(X_{q2} (\mathbf{q}_{s''}, \mathbf{q}_{i''}) \right) \left(z_c - z_{foc} (z_c) + \frac{L}{2} \right) \right) \\
& \times \mathrm{sinc}\left(\frac{L}{2} \left(\left(\frac{\partial k_s}{\partial \omega} - \frac{\partial k_i}{\partial \omega} \right) \left(\Omega + \frac{\omega_{0s} - \omega_{0i}}{2} - \Delta T c_t - \Delta\omega_p c_{\omega p} \right) + X_{q3} (\mathbf{q}_{s''}, \mathbf{q}_{i''}) \right) \right).
\end{aligned}
\tag{C.7}
$$

C.5 Applicability to other type-II SPDC configurations

The calculations have been shown for the case of collinear SPDC with a periodically poled crystal. However, the method is also applicable to noncollinear down-conversion and when a crystal without periodic poling is used. In the theory above, this modifies the Taylor expansion of the longitudinal wavevectors (Eq. (C.4)), and consequently the wavevector mismatch Δk_z of Eq. (C.6). Specifically, the first derivative of the wavenumbers with respect to the transverse momentum can be non-zero and the expansion can be performed about non-zero transverse momenta $\mathbf{q_{0m}}$. Despite these changes, the method for the wavefunction reconstruction can be used since Eq. (3.20) still holds. However, the constants defined in Eqs. (3.21)-(3.24) of the main text are modified in the following way:

$$X_T \equiv \left(X_{0p}\frac{\partial k_p}{\partial T} - X_{0s}\frac{\partial k_s}{\partial T} - X_{0i}\frac{\partial k_i}{\partial T} + \frac{2\pi}{\left(\Lambda\left(T_0\right)\right)^2}\frac{\partial \Lambda}{\partial T} \right) \tag{C.8}$$

$$X_\omega \equiv \left(X_{0p}\frac{\partial k_p}{\partial \omega} - X_{0s}\frac{\partial k_s}{2\partial \omega} - X_{0i}\frac{\partial k_i}{2\partial \omega} \right) \tag{C.9}$$

$$c_t \equiv -\frac{X_T}{\left(X_{0s}\frac{\partial k_s}{\partial \omega} - X_{0i}\frac{\partial k_i}{\partial \omega} \right)} \tag{C.10}$$

$$c_{\omega p} \equiv -\frac{X_\omega}{\left(X_{0s}\frac{\partial k_s}{\partial \omega} - X_{0i}\frac{\partial k_i}{\partial \omega} \right)}, \tag{C.11}$$

with the new constant $X_{0m} \equiv \frac{k_m(\mathbf{q_{0m}},\omega_{0m},T_0)}{k_{zm}(\mathbf{q_{0m}},\omega_{0m},T_0)} = \frac{k_m(\mathbf{q_{0m}},\omega_{0m},T_0)}{\sqrt{(k_m(\mathbf{q_{0m}},\omega_{0m},T_0)^2 - |\mathbf{q_{0m}}|^2)}}$. Additionally, a crystal without periodic poling can be considered as having an infinite poling period and then the dependence on the poling period in Eq. (C.8) drops out.

The applicability of the method relies on the fact that to first order, the argument of the phase matching function has a linear dependence on Ω and on the crystal temperature and pump frequency.

In practice, the easiest way of obtaining the constants c_t or $c_{\omega p}$ may be by experimentally measuring the shift in the biphoton spectral amplitude induced by a change in crystal temperature or pump frequency.

C.6 Quantum state reconstruction for the case of a pulsed pump

This section shows that in the case of a pulsed pump, it is possible to gain information about the Wigner function where the sum-frequency variable has been traced out. The way we will proceed is by working out the expression for the reduced Wigner function and comparing it with the measurable quantities from the wavefunction reconstruction scheme.
Lifting the constraint of a monochromatic pump and allowing a superposition of different pump frequencies, the biphoton density matrix is defined as

$$\begin{aligned}\rho &= |\psi\rangle\langle\psi| \\ &= \int \mathrm{d}\omega_s \mathrm{d}\omega_i \mathrm{d}\omega_s' \mathrm{d}\omega_i' \, \Phi\left(\omega_s,\omega_i\right) \Phi^*\left(\omega_s',\omega_i'\right) a_s^\dagger\left(\omega_s\right) a_i^\dagger\left(\omega_i\right) |0\rangle\langle 0| \, a_s\left(\omega_s'\right) a_i\left(\omega_i'\right).\end{aligned} \tag{C.12}$$

and with that, the biphoton Wigner function is

$$W(\mu_1,\mu_2,\tau_1,\tau_2) = \frac{1}{\pi^2}\int \mathrm{d}\Omega_1\mathrm{d}\Omega_2 \left\langle \mu_1+\Omega_1,\mu_2+\Omega_2\right| \rho \left|\mu_1-\Omega_1,\mu_2-\Omega_2\right\rangle \times \exp\left[2i\left(\Omega_1\tau_1+\Omega_2\tau_2\right)\right], \tag{C.13}$$

where

$$|x,y\rangle = a_s^\dagger(x)\, a_i^\dagger(y)\,|0\rangle\,. \tag{C.14}$$

This leads to

$$W(\mu_1,\mu_2,\tau_1,\tau_2) = \frac{1}{\pi^2}\int \mathrm{d}\Omega_1\mathrm{d}\Omega_2\, \Phi(\mu_1+\Omega_1,\mu_2+\Omega_2)\,\Phi^*(\mu_1-\Omega_1,\mu_2-\Omega_2) \times \exp\left[2i\left(\Omega_1\tau_1+\Omega_2\tau_2\right)\right]. \tag{C.15}$$

It can be rewritten in the diagonal coordinates in the following way:

$$W'(\omega_+,\omega_-,\tau_+,\tau_-) = \frac{1}{\pi^2}\int \mathrm{d}\Omega_1\mathrm{d}\Omega_2\,\Phi\left(\frac{\omega_+ + 2\omega_-}{2}+\Omega_1,\frac{\omega_+-2\omega_-}{2}+\Omega_2\right) \times \Phi^*\left(\frac{\omega_+ + 2\omega_-}{2}-\Omega_1,\frac{\omega_+-2\omega_-}{2}-\Omega_2\right) \tag{C.16}$$

$$\times \exp\left[2i\left(\Omega_1\frac{2\tau_+ + \tau_-}{2}+\Omega_2\frac{2\tau_+-\tau_-}{2}\right)\right], \tag{C.17}$$

where $\omega_+ = \mu_1+\mu_2$, $\omega_- = (\mu_1-\mu_2)/2$, $\tau_+ = \frac{1}{2}(\tau_1+\tau_2)$, $\tau_- = \tau_1-\tau_2$.

Additionally defining $\Omega_+ = \Omega_1+\Omega_2$, $\Omega_- = (\Omega_1-\Omega_2)/2$ so that $\Omega_1 = \frac{\Omega_+}{2}+\Omega_-$, $\Omega_2 = \frac{\Omega_+}{2}-\Omega_-$, one obtains

$$W'(\omega_+,\omega_-,\tau_+,\tau_-) = \frac{1}{\pi^2}\int \mathrm{d}\Omega_+\mathrm{d}\Omega_- \times \Phi\left(\frac{1}{2}(\omega_++\Omega_+)+(\omega_-+\Omega_-),\frac{1}{2}(\omega_++\Omega_+)-(\omega_-+\Omega_-)\right) \times \Phi^*\left(\frac{1}{2}(\omega_+-\Omega_+)+(\omega_--\Omega_-),\frac{1}{2}(\omega_+-\Omega_+)-(\omega_--\Omega_-)\right) \times \exp\left[2i\left(\tau_+\Omega_+ + \tau_-\Omega_-\right)\right]. \tag{C.18}$$

Now the goal is to trace out the sum coordinates ω_+ and τ_+ to obtain the reduced Wigner function:

$$W''(\omega_-,\tau_-) = \frac{1}{\pi^2}\int \mathrm{d}\omega_+\mathrm{d}\tau_+\mathrm{d}\Omega_+\mathrm{d}\Omega_- \Phi\left(\frac{1}{2}(\omega_+ + \Omega_+) + (\omega_- + \Omega_-), \frac{1}{2}(\omega_+ + \Omega_+) - (\omega_- + \Omega_-)\right) \times\Phi^*\left(\frac{1}{2}(\omega_+ - \Omega_+) + (\omega_- - \Omega_-), \frac{1}{2}(\omega_+ - \Omega_+) - (\omega_- - \Omega_-)\right) \times \exp\left[2i\left(\tau_+\Omega_+ + \tau_-\Omega_-\right)\right]. \tag{C.19}$$

To simplify the expression, the following property can be used: $\frac{1}{2\pi}\int \mathrm{d}x\mathrm{d}t \exp\left(i(x-a)t\right) g(x) = g(a)$. Letting $x = 2\Omega_+$, $t = \tau_+$, $a = 0$ so that $\int \mathrm{d}\Omega_+\mathrm{d}\tau_+ \exp\left(i2\Omega_+\tau_+\right) g(\Omega_+) = \pi g(0)$, this results in

$$W''(\omega_-,\tau_-) = \frac{1}{\pi}\int \mathrm{d}\omega_+\mathrm{d}\Omega_- \Phi\left(\frac{1}{2}\omega_+ + (\omega_- + \Omega_-), \frac{1}{2}\omega_+ - (\omega_- + \Omega_-)\right) \times\Phi^*\left(\frac{1}{2}\omega_+ + (\omega_- - \Omega_-), \frac{1}{2}\omega_+ - (\omega_- - \Omega_-)\right) \exp\left[2i\tau_-\Omega_-\right]. \tag{C.20}$$

The above can be written as

$$W''(\omega_-,\tau_-) = \frac{1}{\pi}\int \mathrm{d}\omega_+\mathrm{d}\Omega_- \Phi'(\omega_+, \omega_- + \Omega_-) \times\Phi'^*(\omega_+, \omega_- - \Omega_-) \times \exp\left[2i\tau_-\Omega_-\right], \tag{C.21}$$

and this expression of the reduced Wigner function is proportional to $f(\Delta S, T, \omega_{0p})$.

Appendix D

Sagnac source

The purpose of this source is the creation of polarisation-entangled photon pairs of the form

$$\cos(\phi)|H\rangle_1|V\rangle_2 + \sin(\phi)\exp(i\alpha_0)|V\rangle_1|H\rangle_2, \tag{D.1}$$

where H and V denote horizontal and vertical polarisations, respectively, $|\cdot\rangle_i$ with $i \in \{1, 2\}$ symbolises one of two outputs (Gaussian modes in SMFs), and ϕ and α_0 are real parameters.

The basic idea behind the set-up is that type-II SPDC is used within a polarisation-based Sagnac interferometer [150, 151], each direction of the pump light giving rise to one term of the superposition in expression (D.1).

The Sagnac source has the usual advantage of Sagnac interferometers, which is the intrinsic stability that is based on the fact that the two 'arms' of the interferometer actually consist of the same path, just with propagation in opposite directions [126, Sec. 3.6]. So if for instance the path length changes, then this happens for both arms such that a relative length change is avoided. A further benefit is the possibility to tailor the quantum state. As we will see below, the amount of entanglement and the phase between the terms in the superposition can be adjusted in a straightforward manner.

The detailed set-up as implemented in the experiment of Chapter 4 is depicted in Fig. D.1. The section up until the Sagnac PBS serves to prepare the desired pump state. First, the pump power is regulated using a HWP followed by a polarising beam splitter. As the pump power is low, the SPDC counts are proportional to it. Next, the pump polarisation is controlled with a set of waveplates (HWP, QWP, HWP, QWP). The key role of the pump polarisation will become clear shortly. Although any polarisation can be achieved with one HWP and QWP, this combination of four waveplates is especially practical when the polarisation state needs to be adjusted, as it allows direct access to the relative amplitudes of H and V through the first HWP, and to the relative phase between H and V through

the second HWP. After the waveplates, the pump passes through a lens that focuses it into the SPDC crystal. The pump beam waist inside the crystal influences the efficiency of coupling the SPDC photon pairs into SMFs at the end, jointly with the crystal length and the detection beam waist [82, 188]. The reason for this is that the pump beam waist and crystal length determine the amount of spatial correlations and therefore the distribution of Gaussian and higher order LG modes created, while the detection mode determines what Gaussian mode the SPDC state is projected into. The pump beam is then reflected by a dichroic mirror that is reflective at the pump wavelength and transmissive at SPDC wavelengths, and enters the Sagnac loop via the Sagnac PBS. To understand how the overall SPDC state is created, let us follow the pump path in each direction.

Counter-clockwise direction: First of all, what happens for the H polarisation component of the pump? This component is transmitted through the Sagnac PBS so that the loop is traversed in the counter-clockwise direction. The pump enters the SPDC crystal, which is oriented to allow for type-II SPDC with an H polarised pump, thereby creating one V (signal) and one H (idler) polarised SPDC photon. Since the photon pair goes through the HWP before incidence on the polarising beam splitter, we have that the idler photon is V polarised and gets reflected downwards, then transmitted through the dichroic mirror and is incident on the lower coupler. In contrast, the signal photon is transmitted towards the right and is incident on the right coupler. Both couplers incorporate longpass filters to reject pump photons and filter for the SPDC photons.

Clockwise direction: For the V polarised component of the pump, the pump is reflected by the polarising beam splitter so that the Sagnac loop is traversed in the clockwise direction. In this direction, the pump polarisation is rotated from V to H by the HWP before the nonlinear crystal, so that once again the appropriate pump polarisation is available for the down-conversion process, and again a V (signal) and H (idler) photon is created. This time the SPDC photons have no HWP before the polarising beam splitter, and the idler photon is transmitted downwards to the lower coupler, while the signal photon is reflected towards to right coupler.

Putting these two processes together, what we get overall is a photon pair where we definitely have one H and one V polarised photon due to the type-II SPDC process, and we have the idler photon always ending up at the lower coupler (output 2) and the signal photon always ending up at the right coupler (output 1). The labels signal and idler have a meaning besides the polarisation at the exit from the nonlinear crystal. Importantly for the experiment of Chapter 4, the wavelength of the photons can be tuned with the crystal temperature, and the signal and idler wavelengths may be distinct. While the final paths of the signal and idler photons are fixed irrespectively of the pump polarisation, it determines

their polarisations: The pump polarisation component H (V) results in the signal being H (V), with the idler the corresponding opposite. This highlights the role of the pump polarisation in tailoring the state of the photon pair: The relative amplitude between H and V controlled by the first HWP within the set of four waveplates determines ϕ of expression (D.1) and therefore the relative amplitudes of the two terms; the phase between the pump H and V components that is controlled by the second HWP sets the relative phase between the two terms given by α_0 in (D.1). In the experiment of Chapter 4, ϕ is set to $-\pi/4$, while α_0 is adjustable.

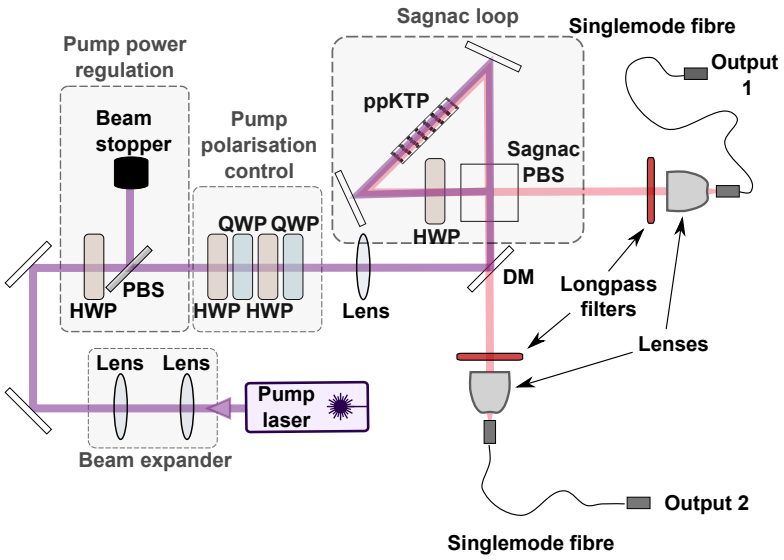

FIGURE D.1: Experimental set-up for the 'Sagnac source', a quantum source based on type-II SPDC within a polarisation-based Sagnac interferometer. A narrowband cw laser (Ondax SureLock diode laser) emits the linearly polarised pump beam at a wavelength of 404.85 nm. The beam is expanded with a telescope using lenses with focal lengths 15 mm and 40 mm. The pump power is set to 2.5 mW with a HWP followed by a polarising beam splitter (PBS). The pump polarisation is prepared with a set of four waveplates (HWP, QWP, HWP, QWP) that are set up to allow control of the relative amplitudes of H and V via the first HWP, and of the relative phase via the second HWP. Next, the pump beam passes through a lens with a focal length of 300 mm, which is placed at a distance of one focal length from the centre of the nonlinear crystal (15 mm ppKTP crystal) inside the Sagnac loop. A dichroic mirror (DM) that is reflective at ∼405 nm and transmissive at ∼810 nm reflects the pump beam that then enters the Sagnac loop via a PBS. This PBS is referred to as the Sagnac PBS and works for both wavelength ranges. Due to a dual wavelength HWP inside the Sagnac loop, the pump beam is H-polarised when it is incident on the nonlinear crystal from either direction. Orthogonally polarised photon pairs are created through type-II SPDC at near-degenerate wavelengths determined by the crystal temperature that is controlled with an oven. The SPDC photons are split at the Sagnac PBS. The pump photons get blocked by the DM in their Sagnac PBS output arm, and in addition, any residual pump light is discarded by longpass filters in both output arms. Finally, the SPDC photons are coupled into SMFs.

List of Symbols

CHAPTER 1

$\hat{\mathbf{A}}$ ..... vector potential operator.

$\mathbf{r}$ ..... spatial coordinate.

t ..... time.

$\mathbf{A}_i$ ..... the i-th member of an orthonormal basis for the classical vector potential.

$\hat{a}_i$ ..... annihilation operator for mode i.

$\hat{a}_i^\dagger$ ..... creation operator for mode i.

$\hat{U}$ ..... unitary symmetry transformation operator.

$\mathbb{1}$ ..... identity operator.

$|\Psi\rangle$ ..... state, with subscripts i (initial) or f (final) indicating the time and 1 or 2 the action of the symmetry operator.

$\hat{T}$ ..... time evolution operator between the initial and final time.

$\hat{U}(\phi)$ ..... unitary symmetry group parameterised by ϕ.

$\hat{O}$ ..... generator of $\hat{U}(\phi)$.

$|\Psi_o\rangle$ ..... eigenstate of $\hat{O}$ with eigenvalue o.

$\hbar$ ..... reduced Planck's constant.

k_0 ..... wavenumber in vacuum.

n ..... refractive index.

θ ..... angle of incidence.

$\mathbf{C}_{mp_z}$ ..... Bessel beam which has the eigenvalue m for the z-component of the total angular momentum, p_z for the z-component of the linear momentum, and -1 for helicity.

$\mathbf{D}_{mp_z}$ ..... Bessel beam which has the eigenvalue m for the z-component of the total angular momentum, p_z for the z-component of the linear momentum, and $+1$ for helicity.

k ..... wavenumber.

P_z ..... z-component of the linear momentum (operator).

J_z ..... z-component of the total angular momentum (operator).

Λ ..... helicity (operator).

$[\rho, \theta, z]$ ..... cylindrical coordinates.

$[\hat{\mathbf{r}}, \hat{\mathbf{l}}, \hat{\mathbf{z}}]$ ..... helical vector basis.

ω ..... angular frequency.

p_ρ ..... magnitude of the transverse momentum.

p_j ..... j-component of the linear momentum, where $j \in \{x, y, z\}$.

$J_m(\,\cdot\,)$ ..... Bessel functions of the first kind.

$\mathbf{J}$ ..... total angular momentum (operator).

$\mathbf{P}$ ..... linear momentum (operator).

ε_0 ..... vacuum permittivity.

μ_0 ..... vacuum permeability.

$\mathbf{E}$ ..... electric field.

$\mathbf{H}$ ..... magnetic field.

CHAPTER 2

Section 2.2

k ..... wavenumber of the incident light.

r ..... nanoaperture radius.

λ ..... wavelength.

Section 2.3

J_z ..... z-component of the total angular momentum.

Λ ..... helicity.

γ ..... ratio between the transmitted powers with changed and unchanged helicities. Optional subscripts indicate the hole diameter for the case with, or the material for the case without a nanoaperture.

d ..... nanoaperture diameter.

Λ_+ ..... mode with unchanged helicity.

Λ_- ..... mode with changed helicity.

ε_i ..... relative permittivity of subdomain i.

μ_i ..... relative permeability of subdomain i.

$\mathbf{k}$ ..... wavevector.

$\mathbf{s}$ ..... transverse electric component.

$\mathbf{p}$ ..... transverse magnetic component.

Section 2.4

α ..... angle obtained through image analysis.

(x, y) ..... transverse scatterer position.

(x_0, y_0) ..... reference scatterer position.

α_0 ..... reference angle.

r ..... distance of scatterer from its reference position.

$\mathbf{q}_{\text{min1,2}}$ ..... intensity minima in the image.

$\mathbf{p}_1$ ..... first point identified in the image analysis: the midpoint between the two intensity minima.

$\mathbf{p}_2$ ..... second point identified in the image analysis: the intensity-weighted centroid.

A ..... region of interest within an image.

$\mathbf{r}$ ..... two-dimensional position vector (specifying coordinates within an image).

$I(\mathbf{r})$ ..... intensity at position $\mathbf{r}$.

d ..... distance between $\mathbf{p}_1$ and $\mathbf{p}_2$.

(x_Δ, y_Δ) ..... inferred position of the sample in the x-y plane.

c ..... calibration constant.

CHAPTER 3

Section 3.1

$|m, n\rangle$ ..... two-mode, $(m+n)$-photon state with m photons in mode 1 and n photons in mode 2.

Section 3.2

$|\Psi\rangle$ ..... biphoton wavefunction.

$\mathbf{q}_m$ ..... transverse momentum of photon m.

ω_m ..... angular frequency of photon m.

p, s, i ..... pump, signal, idler.

T ..... crystal temperature.

Φ_{full} ..... biphoton mode function.

$\hat{a}_m^\dagger(\mathbf{q}, \omega)$ .... creation operator for the mode specified by the argument and with the polarisation of photon m.

$\hat{a}_m(\mathbf{q}, \omega)$ .... annihilation operator for the mode specified by the argument and with the polarisation of photon m.

$|0\rangle$ ..... vacuum state.

$\text{sinc}(\cdot)$ ..... cardinal sine function, $\text{sinc}(x) \equiv \frac{\sin(x)}{x}$.

Δk_z ..... longitudinal wavevector mismatch.

L ..... crystal length.

w_p ..... pump beam waist.

k_{zm} ..... longitudinal momentum of photon m.

z_c ..... longitudinal position of the crystal centre.

z_{foc} ..... longitudinal pump focal position.

Λ ..... poling period of the crystal.

n_p ..... refractive index experienced by the pump in the crystal.

$G(\mathbf{q})_z$ ..... spatial projection mode in the transverse plane at the longitudinal position z.

$\mathbf{q}$ ..... transverse momentum.

w_f ..... detection mode beam waist.

d ..... distance of the crystal end from where the detection focal point would be in the absence of the crystal.

k_{air} ..... wavenumber in air.

ω ..... angular frequency.

f_1 ..... focal length of the collection lens.

z_{CL} ..... longitudinal position of the collection lens.

n ..... refractive index.

$|\Psi_{SMF}\rangle$ ..... biphoton wavefunction after projection into single-mode fibres.

Φ ..... biphoton mode function after projection into single-mode fibres.

$R_{coinc,SMF}$ ... coincidence count rate using single-mode fibres.

τ ..... time delay between signal and idler photons at the detectors.

t ..... mean arrival time of signal and idler photons at the detectors.

$\hat{E}_m^{(+)}$ ..... electric field operator of photon m (by polarisation). Without spatial argument it applies to the mode corresponding to the detection SMF, and with spatial argument to the mode corresponding to the given coordinate in the detector plane.

$R_{coinc,FS}$ .... coincidence count rate using free-space APDs.

A_{det} ..... surface area of the free-space APDs.

$R_{coinc,PP}$ .... coincidence count rate at two specified points in the detector plane.

f_2 ..... focal length of the focusing lens in front of the detectors.

$k_{air,z}$ ..... z-component of the wavevector in air.

R_{coinc} ..... coincidence count rate, for a general detection scheme.

Ω ..... difference between the idler frequency and the degenerate frequency, $\omega_i - \omega_p/2$.

g ..... collective function for simplification purposes, which depends on the detection scheme.

T_0 ..... crystal temperature about which the Taylor expansion is performed.

D ..... $\equiv \frac{\partial k_s}{\partial \Omega} - \frac{\partial k_i}{\partial \Omega}$.

E ..... $\equiv \frac{\partial k_p}{\partial T} - \frac{\partial k_s}{\partial T} - \frac{\partial k_i}{\partial T} + \frac{2\pi}{(\Lambda(T_0))^2}\frac{\partial \Lambda}{\partial T}$.

$\mathrm{rect}(\,\cdot\,)$ ..... rectangular function.

τ_0 ..... $\equiv DL/2 + nD(f_1 - z_{CL} + z_c + L/2)$.

q_m ..... m-component of the transverse momentum, $m \in \{x, y\}$.

l ..... side length of the quadratic free-space detection area.

Section 3.3

Ω ..... difference between the signal frequency and the degenerate frequency, $\omega_s - \omega_p/2$.

ΔS ..... path length difference between signal and idler arms.

t ..... modulus of the transmission amplitude of the HOM beam splitter.

r ..... modulus of the reflection amplitude of the HOM beam splitter.

c ..... speed of light in vacuum.

Φ ..... biphoton mode function after spatial projection.

Φ_{full} ..... biphoton mode function before spatial projection.

$G_m(\mathbf{q}_m)$ .... spatial projection mode of photon m.

ω_{0m} ..... frequency of photon m about which the Taylor expansion is performed.

ΔT ..... crystal temperature difference compared to reference temperature used for Taylor expansion.

$\Delta\omega_p$ ..... pump frequency difference compared to reference frequency used for Taylor expansion.

c_t ..... proportionality constant between a shift in crystal temperature and Ω.

$c_{\omega p}$ ..... proportionality constant between a shift in pump frequency and Ω.

CHAPTER 4

λ ..... wavelength.

α ..... optical rotation.

A_j ..... weight of the contribution of transition j to the wavelength-dependent optical activity.

λ_j ..... resonance wavelength corresponding to transition j.

φ ..... phase difference between the two paths within the MZI.

N ..... (mean) number of photons.

$\bar{\alpha}$ ..... mean optical rotation at the wavelengths λ_1 and λ_2.

$\Delta\alpha$ ..... optical rotation difference between the wavelengths λ_1 and λ_2.

C ..... concentration of the optically active solution.

$\alpha\,(C, \lambda)$ ..... angle by which the linear polarisation of single photons gets rotated.

Λ ..... helicity.

$|P, \lambda_m\rangle_n$ ..... a photon with polarisation P and wavelength λ_m in path n.

L ..... left circular polarisation.

R ..... right circular polarisation.

$|\Phi_{\text{in}}\rangle$ ..... first input state.

$|\Psi_{\text{in}}\rangle$ ..... second input state.

α_0 ..... bias phase, the phase originating from the state preparation rather than the interaction with the sample.

$|\Phi_{\text{out}}\rangle$ ..... first output state.

$|\Psi_{\text{out}}\rangle$ ..... second output state.

H ..... horizontal polarisation.

V ..... vertical polarisation.

AB ..... measurement outcome of detecting the first photon with polarisation A and the second with polarisation B, where $A, B \in \{H, V\}$.

σ_m ..... Pauli matrix, with $m \in \{x, y, z\}$.

U_{LR} ..... optical activity transformation matrix for single photons in the L-R basis.

U_{HV} ..... optical activity transformation matrix for single photons in the H-V basis.

$\mathbb{1}$ ..... 2x2 identity matrix.

$\hat{H}_{\mathrm{col}}$ ..... generator of mean rotations.

$\hat{H}_{\mathrm{dif}}$ ..... generator of rotation differences.

$\Delta\theta$ ..... uncertainty of θ.

$I(\theta)$ ..... Fisher information as a function of θ.

$p(x_i|\theta)$ ..... probability of obtaining the measurement outcome x_i given the parameter value of θ.

I_{q} ..... quantum Fisher information.

$|S\rangle$ ..... biphoton state from the Sagnac source.

$\Delta\lambda$ ..... wavelength difference between the two photons in a pair.

β ..... angle of the HWP inserted behind the sample when testing the experimental quantum state.

max ..... the maximum value of a function.

min ..... the minimum value of a function.

APPENDICES

ε ..... relative permittivity.

μ ..... relative permeability.

ϕ_k ..... azimuthal momentum.

k_r ..... magnitude of transverse momentum.

ρ ..... biphoton density matrix.

W ..... biphoton Wigner function.

W' ..... biphoton Wigner function in diagonal coordinates.

W'' ..... reduced biphoton Wigner function in diagonal coordinates, with the sum DOF traced out.

$|P\rangle_i$ ..... a photon with polarisation P in output i of the Sagnac source, with $P \in \{H, V\}$ and $i \in \{1, 2\}$.

ϕ ..... parameter in the description of the output from the Sagnac source that determines the amount of entanglement.

Bibliography

[1] I. Fernandez-Corbaton, X. Zambrana-Puyalto, N. Tischler, X. Vidal, M. L. Juan, and G. Molina-Terriza. *Electromagnetic duality symmetry and helicity conservation for the macroscopic Maxwell's equations.* Phys. Rev. Lett. **111**, 060401 (2013).

[2] A. Büse, N. Tischler, M. L. Juan, and G. Molina-Terriza. *Where are photons created in parametric down-conversion? On the control of the spatio-temporal properties of biphoton states.* J. Opt. **17**, 065201 (2015).

[3] N. Tischler, A. Büse, L. G. Helt, M. L. Juan, N. Piro, J. Ghosh, M. J. Steel, and G. Molina-Terriza. *Measurement and shaping of biphoton spectral wave functions.* Phys. Rev. Lett. **115**, 193602 (2015).

[4] J. Gleick. *Genius: The life and science of Richard Feynman* (Open Road Media, 2011).

[5] L. Novotny and B. Hecht. *Principles of nano-optics* (Cambridge University Press, 2006).

[6] W. Cai and V. Shalaev. *Optical metamaterials: Fundamentals and applications* (Springer Science & Business Media, 2009).

[7] C. F. Bohren and D. R. Huffman. *Absorption and scattering of light by small particles* (WILEY-VCH Verlag GmbH & Co. KGaA, 2004).

[8] P. M. Morse and H. Feshbach. *Methods of theoretical physics* (McGraw-Hill, 1953).

[9] S. A. Maier. *Plasmonics: Fundamentals and applications* (Springer Science & Business Media, 2007).

[10] S. S. Oh and O. Hess. *Chiral metamaterials : Enhancement and control of optical activity and circular dichroism.* Nano Convergence **2**, 24 (2015).

[11] D. R. Smith, J. B. Pendry, and M. C. K. Wiltshire. *Metamaterials and negative refractive index.* Science **305**, 788 (2004).

[12] U. K. Chettiar, S. Xiao, A. V. Kildishev, W. Cai, H.-K. Yuan, V. P. Drachev, and V. M. Shalaev. *Optical metamagnetism and negative-index metamaterials.* MRS Bulletin **33**, 921 (2008).

[13] A. Einstein. *Über einen die Erzeugung and Verwandlung des Lichtes betreffenden heuristischen Gesichtspunkt.* Annalen der Physik **17**, 132 (1905).

[14] M. Planck. *Ueber das Gesetz der Energieverteilung im Normalspectrum.* Annalen der Physik **309**, 553 (1901).

[15] C. K. Hong, Z. Y. Ou, and L. Mandel. *Measurement of subpicosecond time intervals between two photons by interference.* Phys. Rev. Lett. **59**, 2044 (1987).

[16] J. Audretsch. *Entangled systems - New directions in quantum physics* (WILEY-VCH Verlag GmbH & Co. KGaA, 2007).

[17] U. Leonhardt. *Essential quantum optics - From quantum measurements to black holes* (Cambridge University Press, 2010).

[18] S. L. Braunstein, C. M. Caves, and G. J. Milburn. *Generalized uncertainty relations: Theory, examples, and Lorentz invariance.* Annals of Physics **247**, 135 (1996).

[19] D. F. Walls and G. J. Milburn. *Quantum optics* (Springer Science & Business Media, 2008).

[20] P. Kok and B. W. Lovett. *Optical quantum information processing* (Cambridge University Press, 2010).

[21] V. Giovannetti, S. Lloyd, and L. Maccone. *Advances in quantum metrology.* Nature Photon. **5**, 222 (2011).

[22] C. M. Caves. *Quantum-mechanical noise in an interferometer.* Phys. Rev. D **23**, 1693 (1981).

[23] J. P. Dowling. *Quantum optical metrology - the lowdown on high-N00N states.* Contemporary Physics **49**, 125 (2008).

[24] U. Leonhardt. *Quantum physics of simple optical instruments.* Rep. Prog. Phys. **66**, 1207 (2003).

[25] J. D. Jackson. *Classical electrodynamics* (John Wiley & Sons, Inc., 1999).

[26] S. P. Walborn, A. N. de Oliveira, S. Pádua, and C. H. Monken. *Multimode Hong-Ou-Mandel interference.* Phys. Rev. Lett. **90**, 143601 (2003).

[27] I. Marvian and R. W. Spekkens. *Extending Noether's theorem by quantifying the asymmetry of quantum states.* Nat. Commun. **5**, 3821 (2014).

[28] R. P. Feynman, R. B. Leighton, and M. Sands. *The Feynman lectures on physics, vol. 3* (Basic Books, 2013).

[29] E. Noether. *Invariante Variationsprobleme.* Nachr. d. König. Gesellsch. d. Wiss. zu Göttingen, Math-phys. Klasse pp. 235–257 (1918).

[30] I. Fernandez-Corbaton, X. Zambrana-Puyalto, and G. Molina-Terriza. *Helicity and angular momentum: A symmetry-based framework for the study of light-matter interactions.* Phys. Rev. A **86**, 042103 (2012).

[31] N. Tischler, I. Fernandez-Corbaton, X. Zambrana-Puyalto, A. Minovich, X. Vidal, M. L. Juan, and G. Molina-Terriza. *Experimental control of optical helicity in nanophotonics.* Light Sci Appl **3**, e183 (2014).

[32] W.-K. Tung. *Group theory in physics* (World Scientific, 1985).

[33] M. G. Calkin. *An invariance property of the free electromagnetic field.* Am. J. Phys. **33**, 958 (1965).

[34] D. Zwanziger. *Quantum field theory of particles with both electric and magnetic charges.* Phys. Rev. **176**, 1489 (1968).

[35] I. Fernandez-Corbaton. *Helicity and duality symmetry in light matter interactions: Theory and applications.* Ph.D. thesis, Macquarie University (2014).

[36] I. Fernandez-Corbaton and G. Molina-Terriza. *Role of duality symmetry in transformation optics.* Phys. Rev. B **88**, 085111 (2013).

[37] X. Zambrana-Puyalto, X. Vidal, M. L. Juan, and G. Molina-Terriza. *Dual and anti-dual modes in dielectric spheres.* Opt. Express **21**, 17520 (2013).

[38] M. Decker, I. Staude, M. Falkner, J. Dominguez, D. N. Neshev, I. Brener, T. Pertsch, and Y. S. Kivshar. *High-efficiency dielectric Huygens' surfaces.* Adv. Opt. Mater. **3**, 813 (2015).

[39] J. Sautter, I. Staude, M. Decker, E. Rusak, D. N. Neshev, I. Brener, and Y. S. Kivshar. *Active tuning of all-dielectric metasurfaces.* ACS Nano **9**, 4308 (2015).

[40] K. Y. Bliokh, E. A. Ostrovskaya, M. A. Alonso, O. G. Rodríguez-Herrera, D. Lara, and C. Dainty. *Spin-to-orbital angular momentum conversion in focusing, scattering, and imaging systems.* Opt. Express **19**, 26132 (2011).

[41] L. Allen, M. W. Beijersbergen, R. J. C. Spreeuw, and J. P. Woerdman. *Orbital angular momentum of light and the transformation of Laguerre-Gaussian laser modes.* Phys. Rev. A **45**, 8185 (1992).

[42] L. Allen, S. M. Barnett, and M. J. Padgett. *Optical angular momentum* (CRC Press, 2003).

[43] F. Manni, K. G. Lagoudakis, T. K. Paraïso, R. Cerna, Y. Léger, T. C. H. Liew, I. A. Shelykh, A. V. Kavokin, F. Morier-Genoud, and B. Deveaud-Plédran. *Spin-to-orbital angular momentum conversion in semiconductor microcavities.* Phys. Rev. B **83**, 241307 (2011).

[44] I. Fernandez-Corbaton, N. Tischler, and G. Molina-Terriza. *Scattering in multilayered structures: Diffraction from a nanohole.* Phys. Rev. A **84**, 053821 (2011).

[45] A.-L. Baudrion, F. de León-Pérez, O. Mahboub, A. Hohenau, H. Ditlbacher, F. J. García-Vidal, J. Dintinger, T. W. Ebbesen, L. Martín-Moreno, and J. R. Krenn. *Coupling efficiency of light to surface plasmon polariton for single subwavelength holes in a gold film.* Opt. Express **16**, 3420 (2008).

[46] M. L. Juan, M. Righini, and R. Quidant. *Plasmon nano-optical tweezers.* Nature Photon. **5**, 349 (2011).

[47] F. M. Huang, T. S. Kao, V. A. Fedotov, Y. Chen, and N. I. Zheludev. *Nanohole array as a lens.* Nano Lett. **8**, 2469 (2008).

[48] F. J. Garcia-Vidal, L. Martin-Moreno, T. W. Ebbesen, and L. Kuipers. *Light passing through subwavelength apertures.* Rev. Mod. Phys. **82**, 729 (2010).

[49] H. A. Bethe. *Theory of diffraction by small holes.* Phys. Rev. **66**, 163 (1944).

[50] C. J. Bouwkamp. *On the diffraction of electromagnetic waves by small circular disks and holes.* Philips Res. Rep. **5**, 401 (1950).

[51] A. Roberts. *Electromagnetic theory of diffraction by a circular aperture in a thick, perfectly conducting screen.* J. Opt. Soc. Am. A **4**, 1970 (1987).

[52] R. Wannemacher. *Plasmon-supported transmission of light through nanometric holes in metallic thin films.* Opt. Commun. **195**, 107 (2001).

[53] P. B. Catrysse, H. Shin, and S. Fan. *Propagating modes in subwavelength cylindrical holes.* J. Vac. Sci. Technol. B **23**, 2675 (2005).

[54] K. J. Webb and J. Li. *Analysis of transmission through small apertures in conducting films.* Phys. Rev. B **73**, 033401 (2006).

[55] A. Degiron, H. J. Lezec, N. Yamamoto, and T. W. Ebbesen. *Optical transmission properties of a single subwavelength aperture in a real metal.* Opt. Commun. **239**, 61 (2004).

[56] J. Prikulis, P. Hanarp, L. Olofsson, D. Sutherland, and M. Käll. *Optical spectroscopy of nanometric holes in thin gold films.* Nano Lett. **4**, 1003 (2004).

[57] J. Kindler, P. Banzer, S. Quabis, U. Peschel, and G. Leuchs. *Waveguide properties of single subwavelength holes demonstrated with radially and azimuthally polarized light.* Appl. Phys. B **89**, 517 (2007).

[58] J.-M. Yi, A. Cuche, F. de León-Pérez, A. Degiron, E. Laux, E. Devaux, C. Genet, J. Alegret, L. Martín-Moreno, and T. W. Ebbesen. *Diffraction regimes of single holes.* Phys. Rev. Lett. **109**, 023901 (2012).

[59] X. Zambrana-Puyalto, X. Vidal, and G. Molina-Terriza. *Excitation of single multipolar modes with engineered cylindrically symmetric fields.* Opt. Express **20**, 24536 (2012).

[60] B. D. Gates, Q. Xu, M. Stewart, D. Ryan, C. G. Willson, and G. M. Whitesides. *New approaches to nanofabrication: Molding, printing, and other techniques.* Chem. Rev. **105**, 1171 (2005).

[61] S. W. Hell. *Nobel Lecture: Nanoscopy with freely propagating light.* Rev. Mod. Phys. **87**, 1169 (2015).

[62] P. Bon, N. Bourg, S. Lécart, S. Monneret, E. Fort, J. Wenger, and S. Lévêque-Fort. *Three-dimensional nanometre localization of nanoparticles to enhance super-resolution microscopy.* Nat. Commun. **6**, 7764 (2015).

[63] C. Ru, X. Liu, and Y. Sun, eds. *Nanopositioning technologies: Fundamentals and applications* (Springer, 2016).

[64] S. Roy, K. Ushakova, Q. van den Berg, S. F. Pereira, and H. P. Urbach. *Radially polarized light for detection and nanolocalization of dielectric particles on a planar substrate.* Phys. Rev. Lett. **114**, 103903 (2015).

[65] M. Neugebauer, P. Woźniak, A. Bag, G. Leuchs, and P. Banzer. *Polarization controlled directional scattering for nanoscopic position sensing.* arXiv:1511.02066 (2015).

[66] C. Genet and T. W. Ebbesen. *Light in tiny holes.* Nature **445**, 39 (2007).

[67] J. P. Dowling and K. P. Seshadreesan. *Quantum optical technologies for metrology, sensing, and imaging.* J. Lightwave Technol. **33**, 2359 (2015).

[68] S. Wabnitz and B. J. Eggleton, eds. *All-optical signal processing: Data communication and storage applications* (Springer, 2015).

[69] M. J. Holland and K. Burnett. *Interferometric detection of optical phase shifts at the Heisenberg limit.* Phys. Rev. Lett. **71**, 1355 (1993).

[70] G. Y. Xiang, H. F. Hofmann, and G. J. Pryde. *Optimal multi-photon phase sensing with a single interference fringe.* Sci. Rep. **3**, 2684 (2013).

[71] B. Dayan, A. Pe'er, A. A. Friesem, and Y. Silberberg. *Two photon absorption and coherent control with broadband down-converted light.* Phys. Rev. Lett. **93**, 023005 (2004).

[72] K. A. O'Donnell and A. B. U'Ren. *Time-resolved up-conversion of entangled photon pairs.* Phys. Rev. Lett. **103**, 123602 (2009).

[73] O. Jedrkiewicz, J.-L. Blanchet, E. Brambilla, P. Di Trapani, and A. Gatti. *Detection of the ultranarrow temporal correlation of twin beams via sum-frequency generation.* Phys. Rev. Lett. **108**, 253904 (2012).

[74] E. Brambilla, O. Jedrkiewicz, L. A. Lugiato, and A. Gatti. *Disclosing the spatiotemporal structure of parametric down-conversion entanglement through frequency up-conversion.* Phys. Rev. A **85**, 063834 (2012).

[75] J.-W. Pan, Z.-B. Chen, C.-Y. Lu, H. Weinfurter, A. Zeilinger, and M. Zukowski. *Multiphoton entanglement and interferometry.* Rev. Mod. Phys. **84**, 777 (2012).

[76] R. W. Gerchberg and W. O. Saxton. *A practical algorithm for the determination of phase from image and diffraction plane pictures.* Optik **35**, 237 (1972).

[77] G. Cristobal, P. Schelkens, and H. Thienpont, eds. *Optical and digital image processing: Fundamentals and applications* (John Wiley & Sons, 2013).

[78] I. Prochazka, K. Hamal, and B. Sopko. *Recent achievements in single photon detectors and their applications.* J. Mod. Opt. **51**, 1289 (2004).

[79] E. A. Dauler, B. S. Robinson, A. J. Kerman, J. K. W. Yang, K. M. Rosfjord, V. Anant, B. Voronov, G. Gol'tsman, and K. K. Berggren. *Multi-element superconducting nanowire single-photon detector.* IEEE Trans. Appl. Supercond. **17**, 279 (2007).

[80] S. Carrasco, J. P. Torres, L. Torner, A. Sergienko, B. E. A. Saleh, and M. C. Teich. *Spatial-to-spectral mapping in spontaneous parametric down-conversion.* Phys. Rev. A **70**, 043817 (2004).

[81] H. Di Lorenzo Pires, F. M. G. J. Coppens, and M. P. van Exter. *Type-I spontaneous parametric down-conversion with a strongly focused pump.* Phys. Rev. A **83**, 033837 (2011).

[82] R. S. Bennink. *Optimal collinear Gaussian beams for spontaneous parametric down-conversion.* Phys. Rev. A **81**, 053805 (2010).

[83] J.-L. Smirr, M. Deconinck, R. Frey, I. Agha, E. Diamanti, and I. Zaquine. *Optimal photon-pair single-mode coupling in narrow-band spontaneous parametric downconversion with arbitrary pump profile.* J. Opt. Soc. Am. B **30**, 288 (2013).

[84] T. Guerreiro, A. Martin, B. Sanguinetti, N. Bruno, H. Zbinden, and R. T. Thew. *High efficiency coupling of photon pairs in practice.* Opt. Express **21**, 27641 (2013).

[85] E. Brambilla, L. Caspani, L. A. Lugiato, and A. Gatti. *Spatiotemporal structure of biphoton entanglement in type-II parametric down-conversion.* Phys. Rev. A **82**, 013835 (2010).

[86] G. Brida, M. Chekhova, M. Genovese, and L. Krivitsky. *Generation of different Bell states within the spontaneous parametric down-conversion phase-matching bandwidth.* Phys. Rev. A **76**, 053807 (2007).

[87] A. Gatti, E. Brambilla, L. Caspani, O. Jedrkiewicz, and L. Lugiato. *X entanglement: The nonfactorable spatiotemporal structure of biphoton correlation.* Phys. Rev. Lett. **102**, 223601 (2009).

[88] A. Gatti, T. Corti, E. Brambilla, and D. B. Horoshko. *Dimensionality of the spatiotemporal entanglement of parametric down-conversion photon pairs.* Phys. Rev. A **86**, 053803 (2012).

[89] A. Gatti, L. Caspani, T. Corti, E. Brambilla, and O. Jedrkiewicz. *Spatio-temporal entanglement of twin photons: An intuitive picture.* Int. J. Quantum Inf. **12**, 1461016 (2014).

[90] A. M. Weiner. *Femtosecond pulse shaping using spatial light modulators.* Rev. Sci. Instrum. **71**, 1929 (2000).

[91] C. Ren and H. F. Hofmann. *Time-resolved measurement of the quantum states of photons using two-photon interference with short-time reference pulses.* Phys. Rev. A **84**, 032108 (2011).

[92] C. Ren and H. F. Hofmann. *Analysis of the time-energy entanglement of down-converted photon pairs by correlated single-photon interference.* Phys. Rev. A **86**, 043823 (2012).

[93] F. A. Beduini, J. A. Zielińska, V. G. Lucivero, Y. A. de Icaza Astiz, and M. W. Mitchell. *Interferometric measurement of the biphoton wave function.* Phys. Rev. Lett. **113**, 183602 (2014).

[94] R. Trebino. *Frequency-resolved optical gating : The measurement of ultrashort laser pulses* (Springer Science+Business Media, 2000).

[95] A. Pe'er, B. Dayan, A. A. Friesem, and Y. Silberberg. *Temporal shaping of entangled photons.* Phys. Rev. Lett. **94**, 073601 (2005).

[96] D. Bouwmeester, J.-W. Pan, K. Mattle, M. Eibl, H. Weinfurter, and A. Zeilinger. *Experimental quantum teleportation.* Nature **390**, 575 (1997).

[97] H. F. Hofmann and S. Takeuchi. *Quantum phase gate for photonic qubits using only beam splitters and postselection.* Phys. Rev. A **66**, 024308 (2002).

[98] T. C. Ralph, N. K. Langford, T. B. Bell, and A. G. White. *Linear optical controlled-NOT gate in the coincidence basis.* Phys. Rev. A **65**, 062324 (2002).

[99] E. Knill, R. Laflamme, and G. J. Milburn. *A scheme for efficient quantum computation with linear optics.* Nature **409**, 46 (2001).

[100] M. Michler, K. Mattle, H. Weinfurter, and A. Zeilinger. *Interferometric Bell-state analysis.* Phys. Rev. A **53**, R1209 (1996).

[101] A. M. Steinberg, P. G. Kwiat, and R. Y. Chiao. *Dispersion cancellation in a measurement of the single-photon propagation velocity in glass.* Phys. Rev. Lett. **68**, 2421 (1992).

[102] R. Okamoto, S. Takeuchi, and K. Sasaki. *Tailoring two-photon interference with phase dispersion.* Phys. Rev. A **74**, 011801 (2006).

[103] P. Chen, C. Shu, X. Guo, M. M. T. Loy, and S. Du. *Measuring the biphoton temporal wave function with polarization-dependent and time-resolved two-photon interference.* Phys. Rev. Lett. **114**, 010401 (2015).

[104] T. Douce, A. Eckstein, S. P. Walborn, A. Z. Khoury, S. Ducci, A. Keller, T. Coudreau, and P. Milman. *Direct measurement of the biphoton Wigner function through two-photon interference.* Sci. Rep. **3**, 3530 (2013).

[105] S. Preble, L. Cao, A. Elshaari, A. Aboketaf, and D. Adams. *Single photon adiabatic wavelength conversion.* Appl. Phys. Lett. **101**, 171110 (2012).

[106] A. Fedrizzi, T. Herbst, M. Aspelmeyer, M. Barbieri, T. Jennewein, and A. Zeilinger. *Anti-symmetrization reveals hidden entanglement.* New J. Phys. **11**, 103052 (2009).

[107] D. Kielpinski, J. F. Corney, and H. M. Wiseman. *Quantum optical waveform conversion.* Phys. Rev. Lett. **106**, 130501 (2011).

[108] T. Sh. Iskhakov, S. Lemieux, A. Perez, R. W. Boyd, G. Leuchs, and M. Chekhova. *Nonlinear interferometer for tailoring the frequency spectrum of bright squeezed vacuum.* J. Mod. Opt. **63**, 64 (2016).

[109] C. Polycarpou, K. N. Cassemiro, G. Venturi, A. Zavatta, and M. Bellini. *Adaptive detection of arbitrarily shaped ultrashort quantum light states.* Phys. Rev. Lett. **109**, 053602 (2012).

[110] C. I. Osorio, A. Valencia, and J. P. Torres. *Spatiotemporal correlations in entangled photons generated by spontaneous parametric down conversion.* New J. Phys. **10**, 113012 (2008).

[111] A. Valencia, A. Ceré, X. Shi, G. Molina-Terriza, and J. P. Torres. *Shaping the waveform of entangled photons.* Phys. Rev. Lett. **99**, 243601 (2007).

[112] L. Zhao, X. Guo, Y. Sun, Y. Su, M. M. T. Loy, and S. Du. *Shaping the biphoton temporal waveform with spatial light modulation.* Phys. Rev. Lett. **115**, 193601 (2015).

[113] G. Boucher, T. Douce, D. Bresteau, S. P. Walborn, A. Keller, T. Coudreau, S. Ducci, and P. Milman. *Toolbox for continuous-variable entanglement production and measurement using spontaneous parametric down-conversion.* Phys. Rev. A **92**, 023804 (2015).

[114] A. Moscowitz. *Advances in chemical physics, vol. 4* (John Wiley & Sons, 2009).

[115] L. D. Barron. *Molecular light scattering and optical activity* (Cambridge University Press, 2004).

[116] D. J. Caldwell and H. Eyring. *The theory of optical activity* (Wiley-Interscience, 1971).

[117] E. Charney. *The molecular basis of optical activity: Optical rotatory dispersion and circular dichroism* (Wiley, 1979).

[118] S. F. Mason. *Molecular optical activity and the chiral discriminations* (Cambridge University Press, 1982).

[119] L. Rosenfeld. *Quantenmechanische Theorie der natürlichen optischen Aktivität von Flüssigkeiten und Gasen.* Z. Phys. **52**, 161 (1928).

[120] I. Agranat, H. Caner, and J. Caldwell. *Putting chirality to work: The strategy of chiral switches.* Nat. Rev. Drug Discov. **1**, 753 (2002).

[121] A. Rogers. *Essentials of photonics* (CRC Press, 2008), 2, revised ed.

[122] I. Fernandez-Corbaton, X. Vidal, N. Tischler, and G. Molina-Terriza. *Necessary symmetry conditions for the rotation of light.* J. Chem. Phys. **138**, 214311 (2013).

[123] X. Zambrana-Puyalto, I. Fernandez-Corbaton, M. L. Juan, X. Vidal, and G. Molina-Terriza. *Duality symmetry and Kerker conditions.* Opt. Lett. **38**, 1857 (2013).

[124] I. Fernandez-Corbaton. *Forward and backward helicity scattering coefficients for systems with discrete rotational symmetry.* Opt. Express **21**, 29885 (2013).

[125] X. Vidal, I. Fernandez-Corbaton, A. F. Barbara, and G. Molina-Terriza. *Polarization properties of light scattered off solutions of chiral molecules in non-forward direction.* Appl. Phys. Lett. **107**, 211107 (2015).

[126] P. Hariharan. *Basics of interferometry* (Academic Press, 2012).

[127] V. Giovannetti, S. Lloyd, and L. Maccone. *Quantum-enhanced measurements: Beating the standard quantum limit.* Science **306**, 1330 (2004).

[128] M. Zwierz, C. A. Pérez-Delgado, and P. Kok. *Ultimate limits to quantum metrology and the meaning of the Heisenberg limit.* Phys. Rev. A **85**, 042112 (2012).

[129] M. Zwierz, C. A. Pérez-Delgado, and P. Kok. *General optimality of the Heisenberg limit for quantum metrology.* Phys. Rev. Lett. **105**, 180402 (2010).

[130] A. Kuzmich and L. Mandel. *Sub-shot-noise interferometric measurements with two-photon states.* Quantum Semiclass. Opt. **10**, 493 (1998).

[131] M. W. Mitchell, J. S. Lundeen, and A. M. Steinberg. *Super-resolving phase measurements with a multiphoton entangled state.* Nature **429**, 161 (2004).

[132] K. J. Resch, K. L. Pregnell, R. Prevedel, A. Gilchrist, G. J. Pryde, J. L. O'Brien, and A. G. White. *Time-reversal and super-resolving phase measurements.* Phys. Rev. Lett. **98**, 223601 (2007).

[133] F. W. Sun, B. H. Liu, Y. X. Gong, Y. F. Huang, Z. Y. Ou, and G. C. Guo. *Experimental demonstration of phase measurement precision beating standard quantum limit by projection measurement.* EPL **82**, 24001 (2008).

[134] B. L. Higgins, D. W. Berry, S. D. Bartlett, M. W. Mitchell, H. M. Wiseman, and G. J. Pryde. *Demonstrating Heisenberg-limited unambiguous phase estimation without adaptive measurements.* New J. Phys. **11**, 073023 (2009).

[135] G. Y. Xiang, B. L. Higgins, D. W. Berry, H. M. Wiseman, and G. J. Pryde. *Entanglement-enhanced measurement of a completely unknown optical phase.* Nature Photon. **5**, 43 (2011).

[136] I. Afek, O. Ambar, and Y. Silberberg. *High-NOON states by mixing quantum and classical light.* Science **328**, 879 (2010).

[137] F. Wolfgramm, C. Vitelli, F. A. Beduini, N. Godbout, and M. W. Mitchell. *Entanglement-enhanced probing of a delicate material system.* Nature Photon. **7**, 28 (2013).

[138] Y. Israel, S. Rosen, and Y. Silberberg. *Supersensitive polarization microscopy using NOON states of light.* Phys. Rev. Lett. **112**, 103604 (2014).

[139] T. Ono, R. Okamoto, and S. Takeuchi. *An entanglement-enhanced microscope.* Nat. Commun. **4**, 2426 (2013).

[140] B. E. A. Saleh and M. C. Teich. *Fundamentals of photonics* (Wiley, 1991).

[141] H. F. Hofmann and T. Ono. *High-photon-number path entanglement in the interference of spontaneously down-converted photon pairs with coherent laser light.* Phys. Rev. A **76**, 031806 (2007).

[142] G. Tóth. *Multipartite entanglement and high-precision metrology.* Phys. Rev. A **85**, 022322 (2012).

[143] P. Hyllus, W. Laskowski, R. Krischek, C. Schwemmer, W. Wieczorek, H. Weinfurter, L. Pezzé, and A. Smerzi. *Fisher information and multiparticle entanglement.* Phys. Rev. A **85**, 022321 (2012).

[144] G. Tóth and I. Apellaniz. *Quantum metrology from a quantum information science perspective.* J. Phys. A **47**, 424006 (2014).

[145] M. A. Taylor and W. P. Bowen. *Quantum metrology and its application in biology.* Phys. Rep. **615**, 1 (2016).

[146] B. Bell, S. Kannan, A. McMillan, A. S. Clark, W. J. Wadsworth, and J. G. Rarity. *Multicolor quantum metrology with entangled photons.* Phys. Rev. Lett. **111**, 093603 (2013).

[147] K. Svoboda and S. M. Block. *Biological applications of optical forces.* Annu. Rev. Biophys. Biomol. Struct. **23**, 247 (1994).

[148] H. F. Hofmann. *All path-symmetric pure states achieve their maximal phase sensitivity in conventional two-path interferometry.* Phys. Rev. A **79**, 033822 (2009).

[149] H. Cable and G. A. Durkin. *Parameter estimation with entangled photons produced by parametric down-conversion.* Phys. Rev. Lett. **105**, 013603 (2010).

[150] T. Kim, M. Fiorentino, and F. N. C. Wong. *Phase-stable source of polarization-entangled photons using a polarization Sagnac interferometer.* Phys. Rev. A **73**, 012316 (2006).

[151] A. Fedrizzi, T. Herbst, A. Poppe, T. Jennewein, and A. Zeilinger. *A wavelength-tunable fiber-coupled source of narrowband entangled photons.* Opt. Express **15**, 15377 (2007).

[152] R. Okamoto, H. F. Hofmann, T. Nagata, J. L. O'Brien, K. Sasaki, and S. Takeuchi. *Beating the standard quantum limit: Phase super-sensitivity of N-photon interferometers.* New J. Phys. **10**, 073033 (2008).

[153] A. Crespi, M. Lobino, J. C. F. Matthews, A. Politi, C. R. Neal, R. Ramponi, R. Osellame, and J. L. O'Brien. *Measuring protein concentration with entangled photons.* Appl. Phys. Lett. **100**, 233704 (2012).

[154] T. M. Lowry and E. M. Richards. *CCCXLVI.-The rotatory dispersive power of organic compounds. Part XIII. The significance of simple rotatory dispersion. Rotatory dispersion of camphorquinone and of sucrose.* J. Chem. Soc., Trans. **125**, 2511 (1924).

[155] N. Spagnolo, L. Aparo, C. Vitelli, A. Crespi, R. Ramponi, R. Osellame, P. Mataloni, and F. Sciarrino. *Quantum interferometry with three-dimensional geometry.* Sci. Rep. **2**, 862 (2012).

[156] P. C. Humphreys, M. Barbieri, A. Datta, and I. A. Walmsley. *Quantum enhanced multiple phase estimation.* Phys. Rev. Lett. **111**, 070403 (2013).

[157] J.-D. Yue, Y.-R. Zhang, and H. Fan. *Quantum-enhanced metrology for multiple phase estimation with noise.* Sci. Rep. **4**, 5933 (2014).

[158] P. Kok, J. Dunningham, and J. F. Ralph. *Quantum estimation of coupled parameters and the role of entanglement.* arXiv:1505.06321 (2015).

[159] P. A. Knott, T. J. Proctor, A. J. Hayes, J. F. Ralph, P. Kok, and J. A. Dunningham. *Local versus global strategies in multi-parameter estimation.* arXiv:1601.05912 (2016).

[160] I. Urizar-Lanz, P. Hyllus, I. L. Egusquiza, M. W. Mitchell, and G. Tóth. *Macroscopic singlet states for gradient magnetometry.* Phys. Rev. A **88**, 013626 (2013).

[161] G. Tóth and M. W. Mitchell. *Generation of macroscopic singlet states in atomic ensembles.* New J. Phys. **12**, 053007 (2010).

[162] N. Behbood, F. Martin Ciurana, G. Colangelo, M. Napolitano, G. Tóth, R. J. Sewell, and M. W. Mitchell. *Generation of macroscopic singlet states in a cold atomic ensemble.* Phys. Rev. Lett. **113**, 093601 (2014).

[163] M. Rådmark, M. Zukowski, and M. Bourennane. *Experimental test of fidelity limits in six-photon interferometry and of rotational invariance properties of the photonic six-qubit entanglement singlet state.* Phys. Rev. Lett. **103**, 150501 (2009).

[164] T. Sh. Iskhakov, M. V. Chekhova, G. O. Rytikov, and G. Leuchs. *Macroscopic pure state of light free of polarization noise.* Phys. Rev. Lett. **106**, 113602 (2011).

[165] T. Sh. Iskhakov, I. N. Agafonov, M. V. Chekhova, G. O. Rytikov, and G. Leuchs. *Polarization properties of macroscopic Bell states.* Phys. Rev. A **84**, 045804 (2011).

[166] V. Giovannetti, S. Lloyd, and L. Maccone. *Quantum metrology.* Phys. Rev. Lett. **96**, 010401 (2006).

[167] R. Jozsa, D. S. Abrams, J. P. Dowling, and C. P. Williams. *Quantum clock synchronization based on shared prior entanglement.* Phys. Rev. Lett. **85**, 2010 (2000).

[168] Y.-L. Zhang, Y.-R. Zhang, L.-Z. Mu, and H. Fan. *Criterion for remote clock synchronization with Heisenberg-scaling accuracy.* Phys. Rev. A **88**, 052314 (2013).

[169] A. E. Lita, A. J. Miller, and S. W. Nam. *Counting near-infrared single-photons with 95% efficiency.* Opt. Express **16**, 3032 (2008).

[170] H. Lee, P. Kok, N. J. Cerf, and J. P. Dowling. *Linear optics and projective measurements alone suffice to create large-photon-number path entanglement.* Phys. Rev. A **65**, 030101 (2002).

[171] P. Kok, H. Lee, and J. P. Dowling. *Creation of large-photon-number path entanglement conditioned on photodetection.* Phys. Rev. A **65**, 052104 (2002).

[172] G. J. Pryde and A. G. White. *Creation of maximally entangled photon-number states using optical fiber multiports.* Phys. Rev. A **68**, 052315 (2003).

[173] J. C. F. Matthews, A. Politi, D. Bonneau, and J. L. O'Brien. *Heralding two-photon and four-photon path entanglement on a chip.* Phys. Rev. Lett. **107**, 163602 (2011).

[174] A. Datta, L. Zhang, N. Thomas-Peter, U. Dorner, B. J. Smith, and I. A. Walmsley. *Quantum metrology with imperfect states and detectors.* Phys. Rev. A **83**, 063836 (2011).

[175] B. M. Escher, R. L. de Matos Filho, and L. Davidovich. *General framework for estimating the ultimate precision limit in noisy quantum-enhanced metrology.* Nat. Phys. **7**, 406 (2011).

[176] N. Gkortsilas, J. J. Cooper, and J. A. Dunningham. *Measuring a completely unknown phase with sub-shot-noise precision in the presence of loss.* Phys. Rev. A **85**, 063827 (2012).

[177] R. Demkowicz-Dobrzański, J. Kołodyński, and M. Guţă. *The elusive Heisenberg limit in quantum-enhanced metrology.* Nat. Commun. **3**, 1063 (2012).

[178] A. M. Marino, N. V. Corzo Trejo, and P. D. Lett. *Effect of losses on the performance of an SU(1,1) interferometer.* Phys. Rev. A **86**, 023844 (2012).

[179] Z. Zhang, S. Mouradian, F. N. C. Wong, and J. H. Shapiro. *Entanglement-enhanced sensing in a lossy and noisy environment.* Phys. Rev. Lett. **114**, 110506 (2015).

[180] P. A. Knott. *An evolutionary algorithm to engineer quantum states with an application in optical quantum metrology.* arXiv:1511.05327 (2015).

[181] S. Cabrini and S. Kawata, eds. *Nanofabrication handbook* (CRC Press, 2012).

[182] T. E. Jenkins. *Multiple-angle-of-incidence ellipsometry.* J. Phys. D: Appl. Phys. **32**, R45 (1999).

[183] Schott. *SCHOTT optical glass data sheets* (2012). `http://refractiveindex.info/download/data/2012/schott_optical_glass_collection_datasheets_dec_2012_us.pdf`.

[184] P. B. Johnson and R. W. Christy. *Optical constants of the noble metals.* Phys. Rev. B **6**, 4370 (1972).

[185] L. A. Giannuzzi and F. A. Stevie, eds. *Introduction to focused ion beams: Instrumentation, theory, techniques and practice* (Springer Science & Business Media, 2005).

[186] K. Kato and E. Takaoka. *Sellmeier and thermo-optic dispersion formulas for KTP.* Appl. Opt. **41**, 5040 (2002).

[187] F. Pignatiello, M. De Rosa, P. Ferraro, S. Grilli, P. De Natale, A. Arie, and S. De Nicola. *Measurement of the thermal expansion coefficients of ferroelectric crystals by a moiré interferometer.* Opt. Commun. **277**, 14 (2007).

[188] D. Ljunggren and M. Tengner. *Optimal focusing for maximal collection of entangled narrow-band photon pairs into single-mode fibers.* Phys. Rev. A **72**, 062301 (2005).